

## ABSTRACT

Title of Document: ELECTRON ACCELERATION BY  
FEMTOSECOND LASER INTERACTION  
WITH MICRO-STRUCTURED PLASMAS

Andrew James Goers, Doctor of Philosophy,  
2015

Directed By: Professor Howard Milchberg  
Department of Physics

Laser-driven accelerators are a promising and compact alternative to RF accelerator technology for generating relativistic electron bunches for medical, scientific, and security applications. This dissertation presents three experiments using structured plasmas designed to advance the state of the art in laser-based electron accelerators, with the goal of reducing the energy of the drive laser pulse and enabling higher repetition rate operation with current laser technology. First, electron acceleration by intense femtosecond laser pulses in He-like nitrogen plasma waveguides is demonstrated. Second, significant progress toward a proof of concept realization of quasi-phasematched direct acceleration (QPM-DLA) is presented. Finally, a laser wakefield accelerator at very high plasma density is studied, enabling relativistic electron beam generation with  $\sim 10$  mJ pulse energies. Major results from these experiments include:

- Acceleration of electrons up to 120 MeV from an ionization injected wakefield accelerator driven in a 1.5 mm long He-like nitrogen plasma waveguide
- Guiding of an intense, quasi-radially polarized femtosecond laser pulse in a 1 cm plasma waveguide. This pulse provides a strong drive field for the QPM-DLA concept.
- Wakefield acceleration of electrons up to ~10 MeV with sub-terawatt, ~10 mJ pulses interacting with a thin (~200  $\mu\text{m}$ ), high density ( $>10^{20} \text{ cm}^{-3}$ ) plasma.
- Observation of an intense, coherent, broadband wave breaking radiation flash from a high plasma density laser wakefield accelerator. The flash radiates > 1% of the drive laser pulse energy in a bandwidth consistent with half-cycle (~ 1 fs) emission from violent unidirectional acceleration of electron bunches from rest.

These results open the way to high repetition rate (>~kHz) laser-driven generation of relativistic electron beams with existing laser technology.

ELECTRON ACCELERATION BY FEMTOSECOND LASER INTERACTION  
WITH MICRO-STRUCTURED PLASMAS

By

Andrew James Goers

Dissertation submitted to the Faculty of the Graduate School of the  
University of Maryland, College Park, in partial fulfillment  
of the requirements for the degree of  
Doctor of Philosophy  
2015

Advisory Committee:  
Professor Howard Milchberg, Chair  
Professor Phillip Sprangle  
Professor Konstantinos D. Papadopoulos  
Professor Ki-Yong Kim  
Dr. Jared Wahlstrand

© Copyright by  
Andrew James Goers  
2015

## Dedication

For my darling wife, Chelsea.

## Acknowledgements

I would like to thank Professor Howard Milchberg for the privilege of working and learning in his group over the past five plus years. Howard's drive and passion for physics is truly inspiring, and it is clear from working with him how much he wants his students to succeed. I truly appreciate the confidence and trust he has placed in my abilities as a scientist.

I would like to thank Yu-Hsin Chen and Brian Layer for working with me and getting me up to speed during my first year in the lab. I had the honor of sharing many late nights (sometimes into early mornings), frustrating days, and the joy of discovery and success with Sung Yoon, Jennifer Elle, and George Hine. Collaboration with you three has made graduate school rewarding beyond simple academic terms. Our next generation of graduate students Linus Feder, Bo Miao, Fatholah Salehi, and Daniel Woodburry have already proven to be creative and capable scientists. Howard's lab is definitely on a track to continued success with your talents, and I am happy to call you all friends. I would also like to thank the crew from Small Lab, Dr. Jared Wahlstrand, Sina Zahedpour, Eric Rosenthal, Nihal Jhaji, and Ilia Larkin for a fresh perspective over lunch or Town Hall breaks. I'm also grateful to the IREAP facilities and administrative staff for their assistance and support; in particular Nolan Ballew, Jay Pyle, and Bryan Quinn have always been happy to help when I've needed advice or assistance with mechanical projects.

Finally, I would not have been able to complete this endeavor without all the encouragement and support provided by my wife, Chelsea Goers, and my parents, Steven and Willona Goers. We did it. Woot!

# Table of Contents

Dedication .....	ii
Acknowledgements .....	iii
Table of Contents .....	iv
List of Figures .....	vi
Chapter 1: Introduction .....	1
1.1 Motivation and outline of the dissertation .....	1
1.2 Laser wakefield acceleration .....	5
1.2.1 The ponderomotive force .....	6
1.2.2 Laser wakefields .....	8
1.2.3 Pulse propagation and self-modulation .....	13
1.2.4 Electron injection .....	16
1.2.5. Acceleration limits and dephasing .....	19
1.3 Quasi-phase-matched direct laser acceleration .....	21
Chapter 2: The UMD 25 TW Laser System .....	27
2.1 Overview of high peak power, femtosecond laser systems – Chirped Pulse Amplification and Ti:Sapphire lasers .....	27
2.2 UMD 25 TW Ti:Sapphire Laser Architecture .....	28
2.3 Spectral phase compensation using an acousto-optic modulator .....	34
2.3.1 Dispersion and higher order spectral phase in femtosecond laser pulses ..	34
2.3.2 Second harmonic FROG .....	37
2.3.3 Spectral phase compensation with an acousto-optic programmable dispersive filter .....	41
2.4 Laser pre-pulse characterization by third order autocorrelation .....	45
2.5 Laser wave front correction using an adaptive optics loop .....	49
2.5.1 Diffraction limited focusing, $M^2$ , and Strehl ratio .....	49
2.5.2 Correction of laser phase front aberrations using closed loop adaptive optics .....	50
2.6 Measurement of spatiotemporal effects .....	55
2.7 Modelocked Nd:YAG Laser System .....	57
Chapter 3: Optical guiding at relativistic intensities in cluster-based plasma channels .....	59
3.1 Introduction to plasma channel guiding .....	59
3.1.1 Self guiding and relativistic self-focusing .....	60
3.1.2 Optical guiding in pre-formed plasma waveguides .....	62
3.2 Plasma waveguides generated in clustered gas targets .....	66
3.2.1 Advantages of using cluster based targets .....	66
3.2.2 Demonstration of efficient coupling into a cluster based plasma channel.	68
3.2.3 Measurement of nearly pure $N^{5+}$ plasma waveguides .....	72
3.3 Guiding at relativistic intensities in pure $N^{5+}$ plasma waveguides .....	74
3.4 Ionization injected wakefield acceleration in an $N^{5+}$ waveguide .....	76
Chapter 4: Guiding of quasi-radially polarized modes in a plasma channel .....	84
4.1 Direct acceleration in a plasma slow wave structure .....	84
4.2 Generation of modulated waveguides for DLA .....	87

4.3 Generation and focusing of quasi-radially polarized beams.....	91
4.4 Guiding of a TEM <sub>01</sub> mode in a plasma channel.....	97
Chapter 5: Characterization of a micrometer-scale cryogenically cooled gas jet for near critical density laser-plasma experiments .....	99
5.1 Introduction.....	99
5.2 High density valve design.....	100
5.3 Isentropic flow model .....	102
5.4 Experimental setup.....	106
5.5 Hydrogen jet density measurements .....	108
5.6 Cluster size and density characterization.....	112
5.6.1 Cluster formation in high pressure gas jets.....	112
5.6.2 Rayleigh scattering-based cluster measurement .....	113
5.7 Conclusion .....	117
Chapter 6: Multi-MeV electron acceleration by sub-terawatt laser pulses in high density plasma.....	119
6.1 Introduction.....	119
6.2 Experimental setup.....	120
6.3 Electron acceleration.....	123
6.4 Wave breaking radiation .....	126
6.5 Acceleration mechanism.....	131
6.6 Summary .....	132
Chapter 7: Summary and Future Work.....	134
7.1 Summary .....	134
7.2 Future Work .....	135
7.2.1 Plasma channel guiding experiments.....	135
7.2.2 Quasi-phase-matched direct laser acceleration.....	136
7.2.3 High density laser-plasma interaction experiments .....	137
Bibliography .....	139



## List of Figures

**Figure 1.1.** Basic schematic of a laser wakefield accelerator. The high intensity laser pulse drives a charge density wave in a plasma traveling with a phase velocity near the speed of light. The high amplitude electrostatic field associated with the charge density wave can accelerate a co-propagating electron bunch to high energy. Image from ref [250]..... 2

**Figure 1.2.** The density variation averaged over the laser frequency time scale,  $\delta n/n_0$ , (dashed curve) and axial electric field,  $E_z/E_0$ , (solid curve) of a plasma wave driven by a Gaussian laser pulse with RMS length  $L=k_p^{-1}$  and peak vector potential  $a_0 = 0.5$  (a) and  $a_0 = 2.0$  (b). The pulse is moving to the right centered at  $k_p \zeta = 0$  and the fluid quantities are found by numerically solving equation (1.16)-(1.18). Figure from ref [5]. ..... 12

**Figure 1.3.** Self-modulation of the pulse by the driven plasma wave can result in high amplitude waves. The laser pulse (red) initially drives a low amplitude plasma wave (blue). The plasma wave represents a longitudinally varying refractive index which, after sufficient propagation distance, can modulate the pulse amplitude on a scale of the plasma wavelength. The individual pulselets resonantly drive the plasma wave, resulting in a higher wave amplitude. The dashed line on the right shows the original pulse intensity envelope. .... 14

**Figure 2.1.** Block diagram of the 25 TW laser system used to perform the experiments in this dissertation..... 29

**Figure 2.2.** Spectrum of the laser pulse at various points in the amplification chain. Gain narrowing reduces the spectral bandwidth in the regenerative and multi-pass amplifiers to a final bandwidth of 26 nm, with the majority of the narrowing occurring in the regenerative amplifier. Gain shifting, again primarily in the regenerative amplifier, shifts the center wavelength from 790 nm in the oscillator to 808 nm after amplification..... 31

**Figure 2.3.** Amplified and expanded beam profile before (a) and after (b) implementing a vertical beam inversion after the second pass of the MPA. Lineouts along the x (c) and y (d) axes show a moderate improvement in the beam uniformity after the beam flip. .... 32

**Figure 2.4.** (a) Theoretical energy output per pass in the MPA pumped by two 9 mm diameter, 1.5 J frequency doubled Nd:YAG lasers. The seed pulse reaches gain saturation on the fourth pass. (b) Measured seed beam profile after the fourth and final pass through the MPA crystal. The pulse energy is 1.4 J..... 33

**Figure 2.5.** (a) A schematic of the single shot SHG FROG used for characterization of the pulse spectral amplitude and phase. The pulse is split using a thin pellicle beamsplitter and focused using a cylindrical lens into a BBO crystal. Focusing using a cylindrical lens allows the time delay,  $\tau$ , to be mapped onto the geometrical dimension,  $x$ , perpendicular to the direction of focusing as illustrated in (b). The sum

frequency signal pulse is imaged to the entrance slit of an imaging spectrometer to form the complete SHG FROG spectrogram in a single shot.....	38
<b>Figure 2.6.</b> SHG FROG measurement of a pulse exhibiting strong cubic spectral phase. The measured trace (a) and retrieved trace (b) closely match, with a FROG error of 0.006. Extracted spectral domain (c) and time domain (d) representations of the pulse electric field amplitude and phase show the effect of non-negligible third order spectral phase.....	40
<b>Figure 2.7.</b> Measured (a) and retrieved (b) SHG FROG traces after spectral phase compensation by the Dazzler AOPDF. The retrieved spectral phase (c) is much flatter and the retrieved temporal intensity envelope (d) is nearly bandwidth limited with FWHM pulsewidth 39 fs.....	43
<b>Figure 2.8.</b> The FWHM pulse duration measured by the SHG FROG as a function of GDD applied by the Dazzler along with a least squares fit to a hyperbola. ....	45
<b>Figure 2.9.</b> The third order nonlinearity in the high dynamic range autocorrelator makes pre- and post- pulses distinguishable. Overlap of the main pulse in the fundamental arm with the pre-pulse of the second harmonic arm ( $\tau - 1$ ) gives a third harmonic signal equal to the square of the signal from overlapping the main pulse of the second harmonic arm with the pre-pulse of the fundamental arm.....	46
<b>Figure 2.10.</b> Sample third order autocorrelation trace of the amplified pulse. Higher resolution scans are shown around areas with known pulse structure.....	48
<b>Figure 2.11.</b> Schematic layout of an adaptive optics loop utilizing a reference arm for downstream aberration correction. First, a loop is closed with the SID4 behind the laser focus correcting the beam to a perfect diverging wave front. These mirror voltages are then used to obtain a reference wave front upstream of the final focusing optic. For daily operation, the loop is closed with the SID4 in this reference arm which corrects for aberrations in the full laser chain.....	52
<b>Figure 2.12.</b> Measured laser wave front and focal spot before (a) and after (b) convergence of the adaptive optics loop. The phase measurements are in units of waves with $\lambda = 800nm$ . The wave front curvature and tilts have been removed for clarity. The spatial scale is the same in both focal spot images though the color scales are individually normalized. ....	54
<b>Figure 2.13.</b> Schematic drawing of the inverted field autocorrelator (IFA). A pulse with angular spatial chirp is sent through a modified Mach-Zehnder interferometer and interfered with a slight tilt in the direction perpendicular to the angular spatial chirp. Interference fringes will be visible on the CCD only in the region where the pulses overlap within a coherence length. ....	56
<b>Figure 2.14.</b> Inverted field autocorrelation traces before (a) and after (c) correction of a 0.5 $\mu rad/nm$ angular chirp on a 39 fs pulse. The focal spot before (b) the correction is elliptical and becomes much more symmetric after improvement of the grating parallelism (d).....	57
<b>Figure 3.1.</b> Experimental setup for making plasma waveguides in cluster jets. A 140 ps channel forming pulse is focused with an axicon lens over the elongated cluster jet.	

A synchronized femtosecond pulse is focused onto the end of the plasma waveguide through a hole in the axicon. Plasma density is measured using femtosecond transverse interferometry, and guided modes are monitored by relay imaging the exit mode to a CCD camera. .... 68

**Figure 3.2.** Temporal evolution of a plasma waveguide formed from an Nd:YAG laser pulse (250 mJ, 140 ps) interacting with a nitrogen cluster jet. The cluster jet is cooled to a gas reservoir temperature of -170° C and held at 400 psi. The plasma density is initially peaked on axis, but hydrodynamic expansion of the hot plasma creates a density minimum on axis and a radially propagating shock wall. .... 69

**Figure 3.3.** Consecutive exit modes from a 1 cm long nitrogen plasma waveguide injected with a 50 mJ, 40 fs laser pulse focused to a 13 μm FWHM spot size and delayed by 450 ps with respect to the 250 mJ Nd:YAG channel forming pulse. Average measured energy throughput was 50% with a standard deviation of 11%. Maximum throughput reached 79%. .... 70

**Figure 3.4.** (a) Cluster jet nozzle with externally attached 100 μm thick sapphire skimmers. (b) 3D printed nozzle with integrated 400 μm thick skimmers. Both are shown in the same custom cryogenic cooling jacket. .... 71

**Figure 3.5.** Extracted phase shift profiles of a nitrogen plasma waveguide before and ~1 ps after guiding a femtosecond pulse. The waveguide alone (a) has a 250 μm density ramp. Injection of a 0.5 TW pulse (b) and a 2 TW pulse (c) show the presence of a small amount of residual monomer gas at the entrance to the plasma waveguide. The associated exit mode profiles still show a bright Gaussian spot on axis. The color scale is the same on all three phase images. .... 72

**Figure 3.6.** Phase shift profiles of the exit of a nitrogen plasma waveguide before (a) and ~1 ps after (b) guiding a 0.4 TW laser pulse. The difference between the two profiles (c) reveals additional ionization only outside the waveguide. Abel inverted density profiles before and after guiding a 10 TW pulse (d) also show additional ionization only outside the waveguide. .... 73

**Figure 3.7.** Energy throughput and normalized intensity at the exit of a 1 cm nitrogen plasma waveguide with on axis density  $5 \times 10^{18} \text{ cm}^{-3}$  as a function of incident laser power. The injected pulse is 40 fs FWHM with a spot size of 13 μm. Exit modes are shown for incident powers 0.1, 0.4, and 2 times the critical power for relativistic self-focusing. .... 75

**Figure 3.8.** Laser spectrum before and after it is guided through a 1 cm nitrogen plasma waveguide. Spectral broadening is observed with a redshifted tail indicative of coupling to plasma density perturbations. .... 76

**Figure 3.9.** Abel inverted electron density profiles produced by focusing the Nd:YAG channel forming pulse with an axicon lens (a) and an f/20 spherical lens (b). Lineouts along the dashed white line show a nearly parabolic density profile in the axicon case and a flat density profile in the lens focusing case. .... 77

**Figure 3.10.** (a) Optical spectra of the 10 TW pulse before (blue) and after interaction with a flat (black) and guiding (red) electron density profile, each with a peak on axis density of  $1.4 \times 10^{19} \text{ cm}^{-3}$ . A low intensity (0.4 TW) guided mode (b) shows a

Gaussian mode with 14 $\mu\text{m}$ FWHM. High power (10 TW) exit modes from the channel profile (c) and flat density profile (d) show improved confinement by the plasma waveguide.....	79
<b>Figure 3.11.</b> Electron beam profiles from the $\text{N}^{5+}$ waveguide (a) and the $\text{N}^{5+}$ flat density profile (b). A typical spectrum (c) shows acceleration with a peak at 60 MeV while the highest energy spectrum (d) is peaked near 120 MeV.....	80
<b>Figure 3.12.</b> Charge density plots from Turbowave 2D PIC simulations after 1.4 mm propagation in a He-like nitrogen plasma waveguide (a) and a hydrogen plasma waveguide (b) with the same electron density profile. No beam injection is observed in the hydrogen channel case. The longitudinal (c) and transverse (d) phase space of the electrons ionized from $\text{N}^{5+}$ to $\text{N}^{6+}$ in the waveguide after 1.4 mm propagation show similar beam profile and energy as observed in experiments.....	82
<b>Figure 4.1.</b> Experimental setup for creating modulated plasma waveguides using (a) a ring grating to modulate the focused intensity of the channel generating pulse and (b) wire obstructions for creating density modulations by periodically interrupting cluster flow. The general DLA scheme is also presented.....	88
<b>Figure 4.2.</b> Abel inverted density profile of wire modulated plasmas as a function of probe delay. After $\sim 1$ ns delays a density minimum develops on axis providing a suitable density profile for optical guiding. Axial density modulations with a 220 $\mu\text{m}$ period are generated by obstructing the cluster flow with 25 $\mu\text{m}$ diameter tungsten wires.....	89
<b>Figure 4.3.</b> Lineouts of phase profiles in a plasma generated over a cluster jet obstructed by a single wire as a function of cluster jet reservoir temperature. At high temperatures and low mean cluster sizes shock waves are clearly evident while only a ballistic shadow of the wire appears at low temperatures and large mean cluster sizes.....	90
<b>Figure 4.4.</b> Concept of a segmented waveplate used for generating approximately radially polarized light. Slices of a $\lambda/2$ waveplate are arranged with slowly varying orientation of the birefringent crystal's slow axis. This causes a varying rotation of the laser polarization with the azimuthal angle.....	92
<b>Figure 4.5.</b> A pellicle beamsplitter cut in half with a razor blade was used to transform a linearly polarized Gaussian beam into an approximation of a Hermite-Gaussian $\text{TEM}_{01}$ mode. The angle of the pellicle was tuned to apply a $\pi$ phase shift on one half of the beam with respect to the other.....	94
<b>Figure 4.6.</b> The focus of the half-pellicle beam (a) resembles a pure $\text{TEM}_{01}$ Hermite-Gaussian mode (b). Lineouts along the maxima are compared in (c). .....	95
<b>Figure 4.7.</b> The Abel inverted density profile of the first 1.4 mm of an 11 mm nitrogen plasma waveguide (a) with a lineout shown in (b). A Gaussian input mode with an 11 $\mu\text{m}$ spot size (c) is guided with approximately 60% energy throughput and the same spot size as the input mode (d).....	97

<b>Figure 4.8.</b> Series of guided modes at the exit of an 11 mm nitrogen plasma waveguide. The modes retain the two-lobe structure of the injected near-TEM <sub>01</sub> mode with an energy throughput of ~30%. .....	98
<b>Figure 5.1.</b> Custom fabricated straight (a) and tapered (b) nozzles with ~100 μm throats. The gas jet is held in a custom cooling block (c) which can cool the jet to cryogenic temperatures. ....	101
<b>Figure 5.2.</b> Experimental setup for characterizing the high density gas jet (a). Density measurements were made using transverse interferometry. A raw interferogram (b) and Abel inverted density profile (c) are shown along with a raw image of Rayleigh scattering used to measure the cluster size and density in the jet. ....	107
<b>Figure 5.3.</b> Sample 2D hydrogen molecule density profile (a) with 1000 psi backing pressure and -160° C reservoir temperature and lineouts 70, 100, and 200 μm above the nozzle (b). The peak density as a function of height decays exponentially (c) and the FWHM increases linearly with height above the jet (d). ....	109
<b>Figure 5.4.</b> Nitrogen molecule density versus time delay at 200 μm above the 100 μm needle nozzle with the jet reservoir held at 800 psi and -110° C for 500 μs, 1000 μs, and 1500 μs open times.....	110
<b>Figure 5.5.</b> Peak jet density 200 μm above the 100 μm needle nozzle as a function of valve backing pressure at a fixed reservoir temperature -160° C (113 K) (a) and as a function of reservoir temperature at a fixed backing pressure 1000psi (b). ....	111
<b>Figure 5.6.</b> Density as a function of height above the needle (solid) and tapered (dashed) nozzles with 50 (green), 100 (red), and 150 (blue) μm throat all at -160° C and 1000 psi . ....	112
<b>Figure 5.7.</b> Average cluster density (a) and average cluster size (b) as a function of radial position at various heights above the 150 μm diameter nozzle orifice at jet backing pressure and temperature 1000 psi and -160° C.....	116
<b>Figure 5.8.</b> Rayleigh scatter signal versus backing pressure (a) and cluster density (solid line) and size (dotted line) at a height ~1 mm above the 150 μm nozzle (b) with the jet reservoir held at -160° C. ....	117
<b>Figure 6.1.</b> Experimental setup. A horizontally polarized Ti:Sapphire laser pulse (10-50 mJ, 50 fs, λ=800 nm) interacts with a cryogenically-cooled, dense thin H <sub>2</sub> gas jet (a), whose neutral and plasma density profiles are measured by 400 nm probe interferometry (b). A portion of the transmitted laser pulse is reflected by a pellicle (c) and measured by a spectrometer (d). The electron beam from the jet is apertured by a 1.7mm horizontal slit (e), enters a 0.13 T permanent magnet spectrometer, and is dispersed on an aluminum foil-shielded LANEX screen (f), which is imaged by a low noise CCD camera (not shown). (f) shows example quasi-monoenergetic and exponential spectra for a 40 mJ pulse at N <sub>e</sub> =2×10 <sup>20</sup> cm <sup>-3</sup> . Shadowgraphic imaging of the laser interaction region above the needle orifice (g) (needle seen as a shadow at bottom) and imaging (g) and spectroscopy (h) of the wave breaking flash. The pump polarization could also be rotated to the vertical by a half wave plate. ....	121

**Figure 6.2.** Single shot electron beam images for energies  $> 1$  MeV for a range of laser energies and peak profile electron densities. The colour palette was scaled up by  $10\times$  for the 10 mJ column. The onset laser power for detectable electron beam generation was  $\sim 3P_{cr}$  across our range of conditions. .... 123

**Figure 6.3. (a)** Accelerated electron spectra for peak jet electron density  $4.2\times 10^{20}$   $\text{cm}^{-3}$  for varying laser energy. The inset shows total charge  $>2$  MeV as a function of laser energy. The range of effective temperatures of these exponential-like distributions is indicated. The horizontal black lines indicate the experimental uncertainty in the energy, determined by geometry-limited spectrometer resolution. The dashed curve is a 3D PIC simulation for 40 mJ pump which has been scaled by a factor 0.14 to line up with the experimental curve for 40 mJ. **(b)** Accelerated electron spectra at laser energy 40 mJ for varying peak electron density. The dashed curves are from 3D PIC simulations and were scaled by the factor 0.14. .... 124

**Figure 6.4.** Top panel: Side images of intense radiation flashes from wave breaking (10 shot averages). The horizontally polarized pump laser pulse propagates left to right. Image intensities are normalized to the maximum intensity within each column. The vertical dashed line is the centre of the gas jet, whose profile is shown in the lower left. The 40 mJ,  $1.1\times 10^{20}$   $\text{cm}^{-3}$  image for vertical pump polarization (enhanced  $10\times$ ), is dominated by 800 nm Thomson scattering on the left and the flash on the right. Bottom panel: Spectra (10 shot averages) of the flash for conditions enclosed by the dashed black box in the top panel. .... 127

**Figure 6.5.** A sample spectral interferogram between the broadband wave breaking flash and a compressed supercontinuum pulse generated in a Xe gas cell. Fringes are visible across the full 250 nm supercontinuum bandwidth, showing that the broadband flash is spectrally coherent. .... 130

**Figure 6.6.** 2D PIC simulations showing contributions of LWFA and DLA to electron energy gain for a fixed peak plasma density  $N_e = 0.07N_{cr}$  for drive laser energies 15-100mJ. Each blue dot is a tracked electron. Regions above and to the left of the solid red line indicate DLA as the dominant form of acceleration, whereas regions below and to the right are dominated by LWFA. The dashed red diagonal marks zero net energy gain. LWFA dominates acceleration at low drive laser energies, transitioning to DLA at high drive laser energies. .... 132

# Chapter 1: Introduction

## ***1.1 Motivation and outline of the dissertation***

For nearly a century, particle accelerators have been tools of discovery in a wide variety of fields, enabling a number of advances in physics, chemistry, medicine, and biology. Modern RF electron accelerators use periodic, resonantly excited copper cavities phased such that a relativistic electron experiences a constant accelerating force over the length of the accelerator. Accelerating gradients in RF linear accelerators are limited to  $<100$  MV/m by electrical breakdown at the walls of the copper cavities [1,2] with typical accelerating gradients operating near  $\sim 10$  MV/m [1]. These copper cavities can be staged over long distances to reach GeV electron energies while keeping the RF field strength below the breakdown threshold. Smaller machines can supply few MeV electrons in relatively compact devices for applications such as materials processing or electron radiography [3]. The  $\sim 10$  MV/m maximum accelerating gradient is what leads to the large footprint of high energy linear accelerators, and unless advancements in accelerator technology can yield higher gradients future TeV scale electron beams will require RF linacs stretching 10s of kilometers. Further, widespread application of lower energy (1-10 MeV) electron beams is limited by the size and expense of the electron injectors, RF sources, and cavity structures required for linear accelerators.

The application of high power lasers to particle acceleration has been studied as a way to reach much higher accelerating gradients with the aim of making much cheaper, more compact electron and ion accelerators [4–6]. With the advent of chirped pulse amplification [7,8] and the use of Ti:Sapphire as a gain medium [9,10],

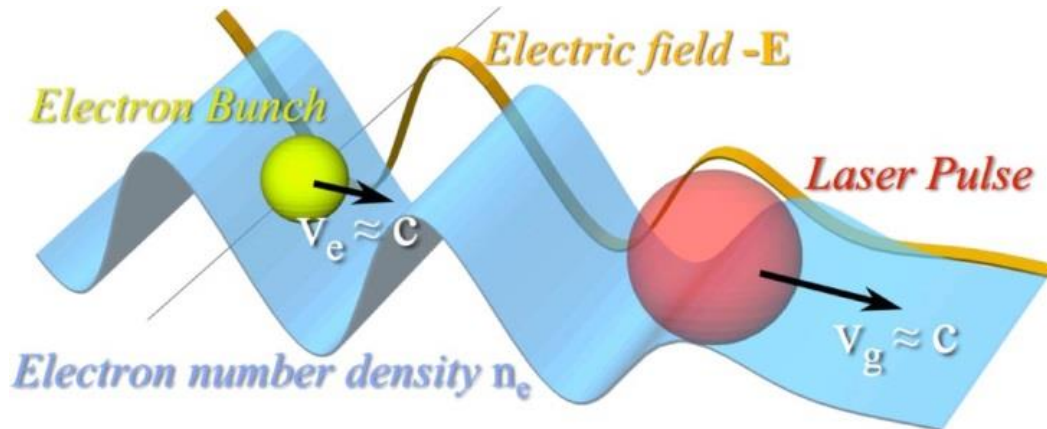


**Figure 1.1.** Basic schematic of a laser wakefield accelerator. The high intensity laser pulse drives a charge density wave in a plasma traveling with a phase velocity near the speed of light. The high amplitude electrostatic field associated with the charge density wave can accelerate a co-propagating electron bunch to high energy. Image from ref [250].

achievable laser intensities have risen dramatically in the last thirty years, with reported peak intensities in excess of  $10^{22}$  W/cm<sup>2</sup> [11]. Peak fields at the focus of femtosecond laser pulses routinely reach beyond 1 TV/m, and a number of schemes have been proposed for directly using them as drivers of next generation compact, high energy particle accelerators [12–16].

While the electric fields associated with femtosecond pulses are extremely strong they are, of course, oscillatory. As a result it is difficult for a particle to gain net energy directly from the laser pulse. In 1979, it was realized by Tajima and Dawson [17] that the plasma medium can act as a transformer between the fast oscillating laser electric fields and more slowly varying plasma fields. By far the most studied scheme for laser driven particle acceleration is the laser wakefield accelerator concept, which is illustrated in Fig. 1.1 [5,17,18]. In laser wakefield accelerators (LWFAs) the high intensity femtosecond laser pulse drives a nonlinear plasma wave. At typical densities in the range  $10^{18}$ - $10^{19}$  cm<sup>-3</sup>, the plasma wave's electrostatic field can be ~100 GV/m, with the plasma wave traveling at the laser



group velocity. This moving electrostatic structure can accelerate a properly phased electron beam to high energy.

Laser driven accelerators have a number of unique properties that make them very promising as next generation accelerators. First, the accelerating fields associated with laser driven accelerators like the LWFA are typically  $10^3$ - $10^4$  times stronger than those of standard RF accelerators. This means that, in principle, the total footprint of a particle accelerator could be drastically reduced, especially when GeV or multi-GeV beams are desired. Next, laser based accelerators driven by femtosecond pulses generally produce femtosecond radiation bursts. For example, electron bunch durations in LWFAs are intrinsically much shorter than a plasma wavelength which, for typically used plasma densities  $\sim 10^{18}$ - $10^{19}$   $\text{cm}^{-3}$ , corresponds to periods  $\sim 10$ - $100$  fs. Further, the radiation source size is approximately the laser focal spot size which is typically  $\sim 10$   $\mu\text{m}$ . The small source size and ultrashort bunch duration enable ultrashort, ultra-bright x-ray sources derived from the high energy electron beams which can be used for high resolution imaging applications as well as ultrafast x-ray or relativistic particle based pump-probe experiments [19].

Currently, laser plasma accelerators are limited in many practical applications by the stability of the electron beam parameters and the repetition rate of available drive laser sources. While improvements on the control and stability of wakefield accelerators have been demonstrated in recent years [20–23], the vast majority of laser wakefield accelerator experiments use joule-class, low repetition rate ( $< 10$  Hz) laser systems. Indeed, the petawatt laser systems required to drive GeV accelerators are only accessible at large facilities and stretch the idea of a “table-top” accelerator.

This dissertation describes experiments using structured gas targets to reduce the drive laser energy needed for production of relativistic electron beams. In the rest of this chapter a brief introduction to the physics of laser wakefield accelerators will be described followed by an introduction to quasi-phase-matched direct acceleration of electrons in a corrugated plasma waveguide [12]. Chapter 2 describes the 25 TW femtosecond laser system used to perform the experiments in this dissertation. Chapter 3 presents experiments on the generation and characterization of plasma waveguides for extending the laser-plasma interaction length at relativistic intensity. An experiment demonstrating the effectiveness of the plasma waveguide for stabilizing the production of wakefield accelerated relativistic electron beams is also described. A novel laser driven acceleration scheme, called quasi-phase-matched direct laser acceleration (QPM-DLA), is presented at the end of this chapter as well as in Chapter 4. Chapter 4 presents experimental progress towards the realization of the QPM-DLA concept including novel methods for producing modulated plasma waveguides and, for the first time, controlled guiding of quasi-radially polarized pulses in a plasma waveguide. Chapters 5 and 6 are related to the development of a seed source of relativistic electrons for use in the QPM-DLA proof-of-principle. Chapter 5 describes a thin  $\sim 100 \mu\text{m}$  scale high density hydrogen gas jet capable of reaching plasma densities above  $10^{21} \text{ cm}^{-3}$ . Chapter 6 describes experiments using this gas jet where relativistic electron beam generation is demonstrated using sub-terawatt femtosecond laser pulses. Accompanying the electron acceleration is intense coherent radiation in the optical frequency range associated with wave breaking and injection of electrons into the accelerating phase of the plasma wave. Measurements

of this broadband “flash” are consistent with half cycle,  $\sim 1$  fs optical radiation associated with the unipolar acceleration of the electrons in the wakefield. The dissertation concludes with a discussion of future research directions.

## ***1.2 Laser wakefield acceleration***

Laser wakefield accelerators were first proposed in 1979 by Tajima and Dawson [17], well before the technology existed for generating laser intensities high enough to efficiently drive nonlinear plasma waves. With advances in laser technology, in particular the advent of the chirped pulse amplification technique [7,8], compact multi-terawatt laser systems became readily available, and laser based acceleration experiments were performed by a number of groups world-wide. The first laser wakefield experiments were operated with relatively long pulse lasers ( $\sim 1$  ps) in the self-modulated regime and demonstrated acceleration gradients in excess of 100 GV/m [24–27]. Electrons were accelerated to energies  $\sim 10$  MeV with total beam charges  $>1$  nC. However, in this regime the accelerated electrons had exponential energy distributions, with a very small fraction at high energy, and large beam divergences.

In 2004 three groups simultaneously achieved accelerated bunches of much lower divergence and energy spread by controlling the laser and plasma parameters so that only a single oscillation of the plasma wave was driven to wave breaking and the laser-plasma interaction length was shorter than a dephasing length [28–30]. The electron beams in these experiments were quasi-monoenergetic ( $\sim 100$  MeV with a few percent energy spread) with low divergence ( $\sim 10$  mrad). Since 2004 the reproducibility and control of these beams has been greatly improved [20,22,23].

Laser wakefield experiments have pushed toward ever higher single stage energy gains with the current world record of 4 GeV produced in a 9 cm long plasma waveguide driven by a 300 TW laser [31]. Many experiments and theoretical proposals are also looking towards methods for generating electron beams with smaller energy spreads and lower transverse emittances, particularly for demanding applications such as injection of x-ray free electron lasers [32–34].

As the stability, reproducibility, and control of wakefield accelerators has improved, these ultrashort relativistic electron beams have been applied to the study of high energy photon sources. Multi-keV x-rays are generated by relativistic electrons executing betatron oscillations about the plasma wave ion column [35–38]. Thomson and Compton scattering experiments have been performed in the linear and recently nonlinear regimes, producing MeV gamma rays [19,39–41]. Wakefield accelerated electrons impinging on high Z targets have even been studied as a positron source [42,43]. As the achievable peak intensity of ultrashort pulses reaches ever higher, wakefield accelerated electron beams coupled to high intensity ( $\sim 10^{23}$  W/cm<sup>2</sup>) lasers could potentially study interesting QED physics such as quantum radiation reaction forces [44].

### 1.2.1 The ponderomotive force

The laser wakefield accelerator concept relies on the radiation pressure of a high intensity laser to drive a plasma wave. The force on the plasma due to the laser radiation pressure is often described via the ponderomotive force which is commonly expressed in terms of the laser normalized vector potential,  $\mathbf{a}_0 = e\mathbf{A}/mc^2$ , where  $\mathbf{A}$  is the laser vector potential,  $e$  is the elementary charge,  $m$  is the electron mass,  $c$  is the

speed of light, and the laser electric field is  $\mathbf{E} = -\frac{1}{c}\partial\mathbf{A}/\partial t$ . Relativistic corrections to the electron motion become important when  $a_0 \approx 1$ . The laser intensity can be related to  $a_0$  in practical units through

$$a_0 \cong 8.5 \times 10^{-10} [\lambda(\mu m)] \sqrt{I_0(W/cm^2)}. \quad (1.1)$$

For a laser pulse centered at  $\lambda = 0.8 \mu m$ ,  $a_0 \approx 1$  for pulse intensities  $I_0 \approx 2 \times 10^{18} W/cm^2$  based on equation (1.1). These intensities are routinely reached by tightly focusing femtosecond laser pulses.

The relativistic ponderomotive force in the plasma can be derived by considering the fluid momentum equation

$$\frac{1}{c} \frac{d\mathbf{u}}{dt} = \frac{1}{c} \frac{\partial \mathbf{u}}{\partial t} + \left( \frac{\mathbf{u}}{\gamma} \cdot \nabla \right) \mathbf{u} = \frac{1}{c} \frac{\partial \mathbf{a}_0}{\partial t} + \nabla \phi - \frac{\mathbf{u}}{\gamma} \times \nabla \times \mathbf{a}_0 \quad (1.2)$$

where  $\mathbf{u} = \gamma \mathbf{v}/c$  is the normalized fluid momentum,  $\gamma = \sqrt{1 + u^2}$  is the fluid Lorentz factor,  $\mathbf{a}_0$  is the laser normalized vector potential, and  $\phi = e\Phi/mc^2$  is the normalized scalar potential associated with charge separation in the plasma.

Recognizing that

$$\left( \frac{\mathbf{u}}{\gamma} \cdot \nabla \right) \mathbf{u} = \frac{1}{\gamma} \left[ \frac{1}{2} \nabla u^2 - \mathbf{u} \times \nabla \times \mathbf{u} \right]$$

and

$$\frac{1}{2\gamma} \nabla u^2 = \frac{1}{2\gamma} \nabla \gamma^2 = \nabla \gamma$$

equation (1.2) becomes

$$\frac{1}{c} \frac{\partial (\mathbf{u} - \mathbf{a}_0)}{\partial t} = \nabla (\phi - \gamma) + \frac{\mathbf{u}}{\gamma} \times \nabla \times (\mathbf{u} - \mathbf{a}_0). \quad (1.3)$$

The generalized ponderomotive force,  $\mathbf{F}_p$ , arises from the  $\nabla \gamma$  term in equation (1.3)

so that

$$\mathbf{F}_p = -mc^2 \nabla \gamma = -\frac{mc^2}{\gamma} \nabla u^2/2. \quad (1.4)$$

This can be related back to the laser vector potential by noticing that  $\mathbf{u}_\perp \approx \mathbf{a}_0$  from conservation of canonical momentum which is exact when the system is one dimensional, i.e. the spot size  $w_0$  satisfies  $w_0 \gg \lambda_p \gg \lambda$ . In this limit  $\mathbf{F}_{p,z} = -\frac{mc^2}{\gamma} \frac{\partial}{\partial z} a_0^2/2$ . Experiments in this dissertation were performed with laser vector potentials  $a_0 \geq 1$  and  $w_0 \sim \lambda_p$ , so the ponderomotive force is best described by equation (1.4).

The ponderomotive force is independent of the sign of the particle charge and will always act to expel charges from regions of high intensity. The ponderomotive force on the ions will be weaker than the ponderomotive force on the electrons by a ratio  $\mathbf{F}_e/\mathbf{F}_i = m_e/m_i$  where  $m_e$  and  $m_i$  are the electron and ion masses. Since  $m_e/m_i \sim 10^{-3}$  the ion motion is usually negligible compared to the electron motion, and the ions are normally considered to be stationary.

### 1.2.2 Laser wakefields

In the weakly relativistic regime ( $a_0 \ll 1$ ) the form of the plasma wave driven by the laser ponderomotive force can be found analytically if it is assumed that the drive laser pulse is non-evolving [45]. While experiments in this dissertation were performed at intensities  $a_0 \geq 1$ , the weakly relativistic treatment shows very clearly that the laser ponderomotive force is responsible for driving plasma waves and can act as a transformer of high intensity laser fields to quasi-static longitudinal accelerating fields. It also shows that the plasma wave is most efficiently excited when the laser pulse duration  $\tau_L \sim 2\pi/\omega_p$ . These insights apply even in the

relativistic regime. Here we assume a cold plasma and stationary ions. These assumptions are justified considering the temperature of a field ionized plasma ( $\sim 10$  eV) is typically much smaller than the electron ponderomotive energy in the laser field ( $\sim 100$  eV – 1 MeV) and the ion displacement due to the ponderomotive force is  $(m_e/m_i)^2 \sim 10^{-6}$  times the electron displacement. In the cold fluid limit the plasma continuity equation, Lorentz force law, and Poisson equation can be used to solve for the wakefields

$$\frac{\partial \delta n}{\partial t n_0} + \nabla \cdot \mathbf{v} = 0 \quad (1.5)$$

$$m \frac{\partial \mathbf{v}}{\partial t} = -e(\mathbf{E}_\perp + \frac{\mathbf{v}}{c} \times \mathbf{B}_\perp + \mathbf{E}_z) \quad (1.6)$$

$$\nabla \cdot \mathbf{E} = 4\pi e \delta n \quad (1.7)$$

where  $\delta n$  is a perturbation about the static plasma electron density  $n_0$ ,  $\mathbf{v}$  is the plasma fluid velocity,  $m$  is the electron mass,  $e$  the elementary charge,  $\mathbf{E}_\perp$  and  $\mathbf{B}_\perp$  are the laser transverse fields, and  $\mathbf{E}_z$  is the longitudinal field associated with the plasma wave. The fluid velocity consists of fast and slowly varying components,  $\mathbf{v} = \mathbf{v}_f + \mathbf{v}_s$ . The slowly varying part of the fluid velocity responds to the ponderomotive force so that equation (1.6) becomes

$$m \frac{\partial \mathbf{v}_s}{\partial t} = \mathbf{F}_p - e\mathbf{E}_z = -\frac{1}{4} m c^2 \nabla a_0^2 - e\mathbf{E}_z. \quad (1.8)$$

Taking the time derivative of (1.5) and the divergence of (1.8) gives

$$\frac{\partial^2 \delta n}{\partial t^2 n_0} = -\frac{\partial}{\partial t} \nabla \cdot \mathbf{v}_s = \frac{1}{4} c^2 \nabla^2 a_0^2 - \frac{e}{m} \nabla \cdot \mathbf{E}_z. \quad (1.9)$$

Using Poisson's equation

$$\frac{e}{m} \nabla \cdot \mathbf{E}_z = \frac{4\pi e^2}{m} \delta n = \frac{4\pi e^2 n_0}{m} \frac{\delta n}{n_0} = \omega_p^2 \frac{\delta n}{n_0}. \quad (1.10)$$

where  $\omega_p^2 = 4\pi n_0 e^2 / m_e$  plasma frequency. Substituting (1.10) into (1.9) gives

$$\left( \frac{\partial^2}{\partial t^2} + \omega_p^2 \right) \frac{\delta n}{n_0} = \frac{c^2}{4} \nabla^2 a_0^2. \quad (1.11)$$

Thus, oscillations in the plasma density are driven by the divergence of the ponderomotive force.

Equation (1.11) can be formally solved using the Green's function for the one-dimensional harmonic oscillator

$$\frac{\delta n}{n_0} = \frac{c^2}{4\omega_p} \int_{-\infty}^t dt' \sin[\omega_p(t-t')] \nabla^2 a^2(\mathbf{r}, t'). \quad (1.12)$$

The longitudinal field is found from (1.12) using Poisson's equation to be

$$\mathbf{E}_z = -\frac{\omega_p m c^2}{4e} \int_{-\infty}^t dt' \sin[\omega_p(t-t')] \nabla a^2(\mathbf{r}, t'). \quad (1.13)$$

The full solution is then obtained by integrating over the temporal shape of the laser pulse. These solutions are valid in the weakly relativistic regime ( $a^2 \ll 1$ ) where the density perturbation is small ( $\delta n/n_0 \ll 1$ ) and the longitudinal field is well below the cold nonrelativistic wave breaking field  $E_z \ll E_0 = mc\omega_p/e$ . The plasma wakefield propagates with a phase velocity  $v_p$ , which is approximately equal to the laser group velocity  $v_g = c\sqrt{1 - \omega_p^2/\omega^2}$ . Further, the wakefield is most efficiently excited when the laser pulse duration  $\tau_L \sim 2\pi/\omega_p$ , and the transverse size of the plasma wave is approximately the laser spot size.

The plasma wake in the nonlinear regime ( $a_0^2 \geq 1$  and  $E_z \geq E_0$ ) can be found in the one dimensional case [46–49] by making the quasi-static approximation so that



the drive laser and plasma fluid variables are assumed to depend only on the light frame coordinate  $\zeta = z - v_p t$ , where  $v_p \cong v_g$  is the plasma wave phase velocity which is approximately equal to the laser group velocity. Using conservation of canonical momentum ( $\mathbf{u}_\perp = \mathbf{a}$ ) and transforming equation (1.2) to the  $\zeta$  coordinate frame gives

$$\gamma - \phi - \beta_p u_z = 1 \quad (1.14)$$

where again  $\mathbf{u} = \gamma \mathbf{v}/c$  is the normalized fluid momentum,  $\gamma = \sqrt{1 + u^2}$  is the fluid Lorentz factor,  $\beta_p = v_p/c$ , and  $\phi$  is the normalized scalar potential [48,49]. From the continuity equation in  $\zeta$  coordinates we have

$$(\beta_p - \beta_z)n = \beta_p n_0 \quad (1.15)$$

where  $\beta_z = v_z/c = u_z/\gamma$  [48]. Equations (1.14) and (1.15) can be substituted into Poisson's equation for the normalized scalar potential to find

$$\frac{\partial^2 \phi}{\partial \zeta^2} = k_p^2 \gamma_p^2 \left\{ \beta_p \left[ 1 - \frac{\gamma_\perp^2}{\gamma_p^2 (1 + \phi)^2} \right]^{-1/2} - 1 \right\} \quad (1.16)$$

where  $\gamma_\perp^2 = 1 + u_\perp^2 = 1 + a^2$  and  $\gamma_p^2 = (1 - \beta_p^2)^{-1}$  [48–50]. Equation (1.16) can be solved numerically given an initial laser pulse profile. The wake electric field can then be found from

$$E_z = -E_0 \partial \phi / \partial \zeta \quad (1.17)$$

where  $E_0 = mc\omega_p/e$  is the cold nonrelativistic wave breaking field. Once the scalar potential is found by solving equation (1.16), the other fluid quantities can be found from [5,50]

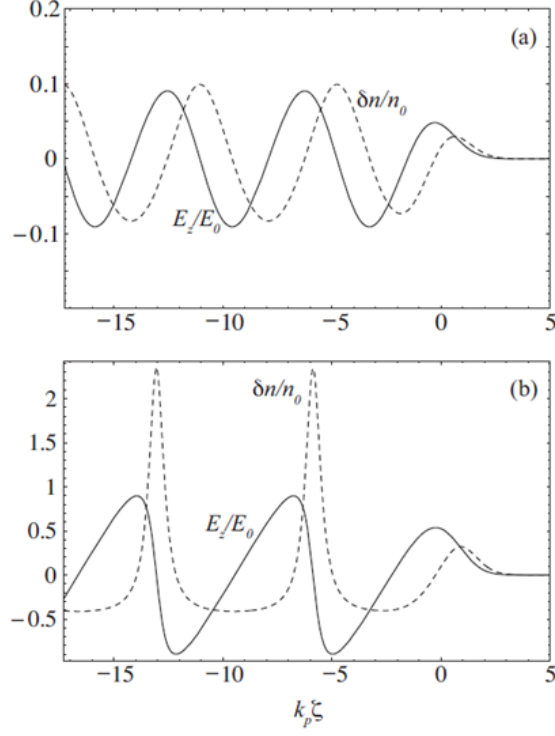


**Figure 1.2.** The density variation averaged over the laser frequency time scale,  $\delta n/n_0$ , (dashed curve) and axial electric field,  $E_z/E_0$ , (solid curve) of a plasma wave driven by a Gaussian laser pulse with RMS length  $L=k_p^{-1}$  and peak vector potential  $a_0 = 0.5$  (a) and  $a_0 = 2.0$  (b). The pulse is moving to the right centered at  $k_p \zeta = 0$  and the fluid quantities are found by numerically solving equation (1.16)-(1.18). Figure from ref [5].

$$n/n_0 = \gamma_p^2 \beta_p \left[ \left( 1 - \frac{\gamma_\perp^2}{\gamma_p^2 (1 + \phi)^2} \right)^{-1/2} - \beta_p \right] \quad (1.18)$$

$$u_z = \gamma_p^2 (1 + \phi) \left[ \beta_p - \left( 1 - \frac{\gamma_\perp^2}{\gamma_p^2 (1 + \phi)^2} \right)^{1/2} \right] \quad (1.19)$$

$$\gamma = \gamma_p^2 (1 + \phi) \left[ 1 - \beta_p \left( 1 - \frac{\gamma_\perp^2}{\gamma_p^2 (1 + \phi)^2} \right)^{1/2} \right]. \quad (1.20)$$

The result of solving equation (1.16)-(1.18) numerically for a Gaussian drive laser pulse of the form  $a(\zeta) = a_0 \exp(-\zeta^2/4L^2) \cos(k\zeta)$  with the RMS pulse length satisfying  $k_p L = 1$  is shown in Fig. 1.2 for the cases  $a_0 = 0.5$  and  $a_0 = 2.0$  [5]. In

the mildly relativistic case ( $a_0 = 0.5$ ), the density perturbation and axial electric field are nearly sinusoidal with a period  $\lambda_p = 2\pi/k_p$ . In contrast, in the highly relativistic case ( $a_0 = 2.0$ ), the wave steepens, the plasma period lengthens, and the axial electric field takes on a sawtooth shape.

In typical experimental conditions, the drive laser pulse undergoes significant evolution and effects such as relativistic self-focusing [51,52] make the problem highly three dimensional in nature. The experiments in this dissertation were performed in a highly nonlinear ( $a_0 \geq 1$ ), multi-dimensional regime ( $w_0 \sim \lambda_p$ ). Modelling of the experimental systems is, therefore, typically done using numerical simulations using either 3D fully relativistic fluid models [53,49] or kinetic simulations [54,55]. Particle in cell (PIC) simulations software, coupled with advances in high performance computing, have greatly improved the ability to model laser-driven wakefield acceleration, and more generally laser-plasma interactions.

### 1.2.3 Pulse propagation and self-modulation

As discussed above, the plasma wake is most efficiently driven by a laser pulse with temporal extent approximately equal to the plasma period. However, even if the drive pulse is much longer than the plasma period, large amplitude plasma waves can be excited through self-modulation of the laser by the plasma wave [25,51,53,56]. In this case the drive laser pulse longitudinally breaks up into a series of pulselets, each separated by the plasma wavelength. This can be qualitatively understood from the solution for the plasma density wave. Equation (1.12) shows that the plasma wave will be driven with a frequency  $\omega_p$  and wavelength  $\lambda_p = 2\pi c/\omega_p$ . Therefore a laser pulse with longitudinal extent longer

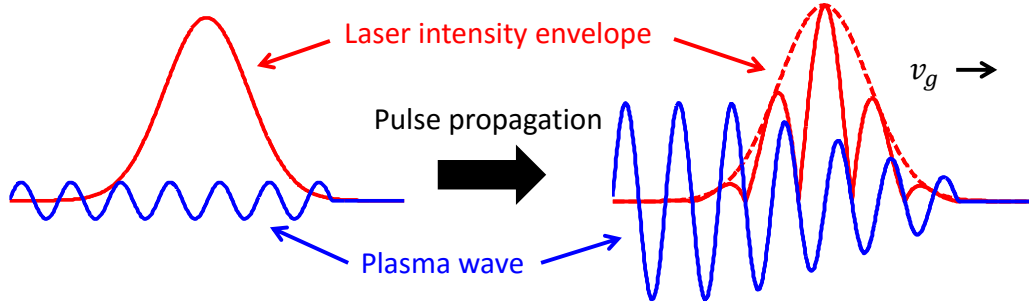


**Figure 1.3.** Self-modulation of the pulse by the driven plasma wave can result in high amplitude waves. The laser pulse (red) initially drives a low amplitude plasma wave (blue). The plasma wave represents a longitudinally varying refractive index which, after sufficient propagation distance, can modulate the pulse amplitude on a scale of the plasma wavelength. The individual pulselets resonantly drive the plasma wave, resulting in a higher wave amplitude. The dashed line on the right shows the original pulse intensity envelope.

than  $\lambda_p$  will experience alternating regions of low and high plasma density. The high density regions will defocus the laser pulse and the pulse can be focused into regions of low density. Furthermore, the pulse group velocity is higher in the low density plasma regions than in the high density regions, causing pulse compression on a scale of  $\lambda_p$ . These effects serve to modulate the pulse into a series of pulses, each of which resonantly drive the plasma wave, as illustrated in Fig. 1.3.

Laser wakefield acceleration in this “self-modulated” regime is important when working with relatively high density plasmas. For example, many early wakefield experiments were operated in the self-modulated regime when ultrashort (<100 fs) pulses were not available [25,27,56–58]. The experiments outlined in Chapter 6 of this dissertation demonstrate a laser wakefield accelerator driven by a 50 fs laser pulse interacting with plasma at densities  $1 - 4 \times 10^{20} \text{ cm}^{-3}$ , with corresponding plasma periods in the range 11 fs – 5.7 fs. These experiments operate in the self-modulated wakefield accelerator regime. The time dependent refractive

index associated with the axial plasma density modulations within the laser pulse lead to significant changes in the frequency spectrum of the drive laser pulse. Raman side bands are observed in the self-modulated regime, and the frequency spectrum of the pulse exiting the accelerator is useful as a diagnostic of the plasma wave amplitude [24,58,59].

Efficient acceleration of electron beams often requires the drive laser pulse to propagate at high intensity over many Rayleigh lengths. This can be achieved by implementing plasma guiding structures where the electron density follows a profile well-approximated as parabolic,  $n(r) = n_0 \left(1 + \frac{\Delta n}{n_0} \left(\frac{r}{w_{ch}}\right)^2\right)$ , where  $\Delta n = n(w_{ch}) - n(0) \geq \frac{1}{\pi r_e w_{ch}^2}$  is the depth of the plasma waveguide,  $r_e$  is the classical electron radius, and  $w_{ch}$  is the radius of the lowest order guided mode [60]. A nonrelativistic laser pulse experiences the refractive index profile  $\eta(r)^2 = 1 - \frac{n(r)}{n_{cr}} = 1 - \frac{n_0}{n_{cr}} \left(1 + \frac{\Delta n}{n_0} \frac{r^2}{w_{ch}^2}\right)$ , which is peaked on axis. This index profile admits bound Laguerre-Gaussian modes and matched guiding of a (nonrelativistic) laser pulse is achieved for a Gaussian beam of spot size  $w_{ch}$  [61].

At sufficiently high intensity, relativistic self-focusing [51,52] becomes important and can lead to nonlinear guiding in a uniform density plasma. In this case the plasma frequency is modified by the relativistic motion of the plasma electrons so that the refractive index becomes

$$\eta(r)^2 = 1 - \frac{\omega_p^2(r)}{\omega^2} = 1 - \frac{\omega_{p0}^2}{\gamma(r)\omega^2} \approx 1 - \frac{\omega_{p0}^2}{\omega^2} + \frac{\omega_{p0}^2}{\omega^2} \frac{a(r)^2}{4}$$

where  $\omega_{p0}$  is the nonrelativistic plasma frequency. If the laser vector potential is peaked on axis, as is the case for lowest order laser modes, the refractive index is peaked on axis, and the pulse feels a focusing force [51,53]. Relativistic self-focusing is similar to nonlinear self-focusing found in Kerr media, and will focus the pulse in the plasma until driven plasma waves stop the pulse collapse. A more complete description of pulse guiding and self-focusing is provided in Chapter 3 of this dissertation as well as in references [5,45,53].

### 1.2.4 Electron injection

While the driven plasma wave represents an accelerating structure, the plasma electrons oscillating in a plasma wave will not have sufficient initial velocity to be trapped and accelerated along with the wave. An electron will be trapped in the accelerating region of the wake only if it is injected with sufficient initial momentum such that the electron velocity is approximately the plasma wave phase velocity [62]. The Lorentz factor associated with the plasma wave phase velocity,  $v_p$ , is  $\gamma_p = (1 - v_p^2/c^2)^{-1/2} \approx \omega/\omega_p = \sqrt{n_{cr}/n_e}$  where  $n_e$  is the ambient electron density. Note that the phase velocity is reduced for higher plasma densities, so the trapping threshold is substantially reduced in the high density acceleration experiments presented in Chapter 6.

Self-injection of background electrons into the wake can occur when the plasma wave amplitude is driven to the wave breaking limit [24,63,64]. In the 1D nonlinear regime, the maximum sustainable electric field amplitude, or wave breaking field, is given by  $E_{WB} = \sqrt{2(\gamma_p - 1)}E_0$  where  $E_0 = cm\omega_p/e$  is the cold

nonrelativistic wave breaking field. At these field amplitudes, electron orbits can gain sufficient momentum from the plasma wave to be injected into the accelerating region. Field amplitudes up to the wave breaking limit can be reached by using very high  $a_0$  drive laser pulses (i.e. the blow-out regime) or in high density, self-modulated wakefield accelerators.

Two dimensional effects have been shown to lower the laser amplitude threshold for driving plasma waves to the wave breaking limit [65]. In this case, transverse variations in the plasma frequency across the laser pulse spot size cause curvature of the plasma wave phase fronts. These transverse variations can be caused by a channel structure where the density is higher off axis or by the relativistic dependence of the plasma frequency on the laser pulse amplitude. The curvature of the plasma wave phase fronts increases for wave periods farther behind the drive laser pulse until the regular wave structure is destroyed by self-intersection of the electron trajectories and transverse wave breaking. When the electron fluid displacement is of the same order as the wave curvature radius a fraction of the electrons can be injected and trapped in the accelerating region of the wake [65]. The complicated, highly nonlinear nature of transverse wave breaking normally necessitates numerical simulation for accurate prediction of the drive pulse amplitude required to achieve self-injection. PIC simulations of the high density experiments described in Chapter 6 show highly curved wake phase fronts and transverse injection of electrons, leading to the observed MeV electron beams.

Self-injection, while ostensibly the easiest method for achieving injection into the plasma wave, does not provide fine control of the injection phase or position

within the accelerator. This can lead to fluctuation in the output beam energy spectrum and charge. As such, controlled injection of external bunches or background plasma electrons into the nonlinear plasma wake has received a significant amount of theoretical and experimental attention [20,34,66–68]. Multi-pulse techniques have been proposed as a means of controlling the injection phase and position. Successful experimental implementations demonstrated electron beams with tunable mean energy and few percent energy spread [20,69]. For example, controlled injection has been achieved by pre-acceleration of background electrons by the ponderomotive force of a tightly focused “injector” pulse [20,67].

Recently, ionization of high Z dopants within the laser produced plasma has become a preferred method for controlled injection [70–74]. In this scheme, the laser produced plasma is formed in a gas typically consisting of a large fraction of helium or hydrogen with a small fraction ( $< 10\%$ ) of a higher atomic number gas such as nitrogen or argon. The high Z dopant is not fully ionized in the leading edge of the wakefield drive pulse. The particular dopant is chosen such that ionization of the inner shell electrons occurs near the peak intensity of the drive pulse. These electrons are “born” within the wake and can become trapped in the wake potential and accelerated to high energy. While the ionization injection technique can lower the injection threshold and provide relatively low emittance beams [75], continuous injection of electrons into the wake leads to large electron beam energy spreads. Combining optical injection techniques with ionization injection has been proposed for generating ultra-low emittance, low energy spread electron beams [32,76].



### 1.2.5. Acceleration limits and dephasing

The energy gain from laser wakefield accelerators is fundamentally limited by the depletion of the drive laser pulse energy and the mismatch between the accelerated electron bunch velocity and the drive pulse group velocity. Laser diffraction is also a limiting factor on the length, and thereby single stage energy gain, of wakefield accelerators. However, as shown in Chapter 3, plasma waveguides and/or relativistic self-focusing can avoid this limitation. The dephasing length,  $L_d$ , can be estimated by considering an electron moving at  $v_e \approx c$  across a quarter plasma wavelength (i.e. through the region of the wake with both a longitudinal accelerating field and radially focusing field) [17]. For a pulse traveling at group velocity  $v_g$  through a uniform plasma this gives

$$\frac{\lambda_p}{4} = (c - v_g) \frac{L_d}{c} = \left( 1 - \sqrt{1 - \frac{\omega_p^2}{\omega^2}} \right) L_d \approx \frac{\omega_p^2}{2\omega^2} L_d \xrightarrow{\text{yields}} L_d = \lambda_p^3 / 2\lambda^2.$$

The dephasing length increases as the plasma density decreases and  $\lambda_p$  increases. Channel guiding can decrease the dephasing length appreciably because of the slower group velocity of the pulse in the channel compared to a transversely uniform plasma [77]. Overcoming the dephasing length in the mildly relativistic regime by tapered or modulated plasma waveguides has been proposed with the goal of reaching higher single stage energy gains [78,79].

The pulse depletion length,  $L_{dep}$ , in the linear regime can be estimated by comparing the wake energy to the laser pulse energy,  $E_z^2 L_{dep} \cong E_L^2 c \tau_p$  where  $E_z$  is the wake electric field,  $E_L$  is the laser electric field, and  $c \tau_p$  is the pulse length [47].

The wake electric field is found by solving equation (1.17) for a given pulse shape.

Assuming a square pulse shape of duration  $\lambda_p/2$  gives a depletion length of

$$L_{dep} \cong \frac{\lambda_p^3}{\lambda^2} \frac{2}{a_0^2} = L_d \frac{2}{a_0^2}.$$

In the mildly relativistic regime, it should be noted that  $L_d \ll L_{dep}$ . However, as the pulse amplitude increases the dephasing and depletion lengths become comparable.

Estimates of the maximum energy gain of an electron in a wakefield accelerator have been made through analytic and numerical studies. The energy gain in the mildly relativistic, dephasing length limited regime can be obtained through  $\Delta W_{max} = e\langle E_z \rangle_{\lambda_p/4} L_d$ , where the accelerating field is averaged over the plasma wave phase region with both accelerating and radially focusing fields. In this regime, Hubbard et al [77] obtain a maximum energy gain of

$$\frac{\Delta W_{max}}{m_e c^2} \sim \frac{a_0^2}{\sqrt{1 + a_0^2/2}} \left( \frac{\lambda_p}{\lambda_0} \right)^2 \left( 1 + \frac{2\lambda_p^2}{\pi^2 w_{ch}^2} \right)^{-1} \quad (1.21)$$

where the factor of  $\left( 1 + \frac{2\lambda_p^2}{\pi^2 w_{ch}^2} \right)^{-1}$  arises from considering the correction to the dephasing length caused by the slower laser group velocity in a plasma waveguide with matched spot size  $w_{ch}$  compared to a uniform plasma. A phenomenological study of energy scaling in the highly nonlinear, 3D blow-out regime ( $a_0 \gg 1$ ) was performed by Lu et al. arriving at the scaling law

$$\frac{\Delta W_{max}}{m_e c^2} \cong \left( \frac{P}{m^2 c^5 / e^2} \right)^{\frac{1}{3}} \left( \frac{\lambda_p}{\lambda} \right)^{\frac{4}{3}}$$

where  $P$  is the drive laser power,  $\lambda_p$  the plasma wavelength, and  $\lambda$  the laser pulse wavelength [80]. This regime assumes a pulse length matched to the plasma wavelength and a peak power above the critical power for relativistic self-focusing.

These scaling laws suggest that higher single stage energy gains can be achieved by driving accelerators with lower plasma density. However, efficiently driving high amplitude plasma waves at low densities requires increasingly longer pulse durations ( $c\tau \sim \lambda_p$ ) and higher energy drive lasers are necessary to maintain the same  $a_0$ . Following this scaling, current state of the art high energy wakefield accelerators are driven by  $\sim 100$  TW – 1 PW scale laser systems in low density ( $< 10^{18}$  cm $^{-3}$ ) plasmas with the goal of reaching  $\sim 10$  GeV single stage energy gains [31]. Conversely, for applications where lower energy electron beams are suitable, the requirement for a high energy drive laser is greatly relaxed. As demonstrated in Chapter 6, this leads to 1 – 10 MeV electron beams accelerated by femtosecond laser pulses with energy as low as  $\sim 10$  mJ.

### ***1.3 Quasi-phase-matched direct laser acceleration***

While laser wakefield acceleration has received the most theoretical and experimental attention from the laser-driven accelerator community, several other techniques have been proposed for achieving high gradient acceleration using intense lasers. Many of these schemes, such as the inverse Cherenkov accelerator [15,16,81], the semi-infinite vacuum accelerator [82], and the vacuum beat wave accelerator [83], suggest the direct use of the laser electric field or ponderomotive force as the accelerating field. These schemes can lead to low emittance, ultrashort electron

bunches but tend to suffer from a modest acceleration gradient ( $< 40$  MV/m) and an acceleration distance limited to approximately a Rayleigh length.

More recently, nano-structured dielectric materials injected with moderate intensity femtosecond laser pulses have shown promise as next generation high gradient accelerators “on a chip” [14]. The dielectric materials are fabricated to form a series of resonant cavities for optical wavelengths in direct analogy to the resonant cavity slow-wave structures used in standard RF linacs. Dielectric accelerators could potentially achieve  $\sim 1$  GV/m accelerating fields when driven by high efficiency, high repetition rate fiber lasers with pulse energy  $\sim 1$   $\mu$ J and pulse lengths  $\sim 1$  ps. With continued development of nano-fabrication techniques and short pulse fiber laser technology, dielectric accelerators could offer a very efficient and compact platform for acceleration of relativistic electron beams.

Much of the work presented in this dissertation was performed in support of a proof of concept demonstration of another direct acceleration scheme, namely quasi-phase-matched direct laser acceleration (QPM-DLA) in an axially modulated plasma waveguide [12,84]. The QPM-DLA scheme requires three main components for operation: a modulated plasma waveguide, a radially polarized laser pulse, and a seed source of relativistic electrons. Chapter 3 demonstrates a method for generation of a plasma waveguide which is used in Chapter 4 to create modulated channels. Also in Chapter 4 generation and guiding of a quasi-radially polarized pulse, which acts as the accelerating field in the DLA scheme, is demonstrated. Finally, Chapters 5 and 6 describe the production of a potential seed source of relativistic electrons which could be used for a QPM-DLA proof of concept experiment.

The QPM-DLA technique proposes using an axially modulated plasma waveguide to guide femtosecond laser pulses with a longitudinal field component over many Rayleigh lengths. As shown in Chapter 4, higher order transverse modes supported by the corrugated plasma channel have a significant axial field component. The corrugated waveguide structure can be shown [12,84] to generate axial field harmonics propagating with a phase velocity given by

$$\frac{v_p}{c} = 1 + \frac{\bar{N}_{e,0}}{2N_{cr}} + \frac{4}{k_0^2 w_{ch}^2} - \frac{mk_{mod}}{k_0}$$

where  $\bar{N}_{e,0}$  is the longitudinally averaged on axis electron density,  $N_{cr}$  is the plasma critical density associated with the drive laser frequency,  $k_0 = 2\pi/\lambda_0$  is the laser wavenumber,  $w_{ch}$  is the matched spot size of the channel,  $k_{mod} = 2\pi/d_{mod}$  is the wavenumber associated with the density modulation period  $d_{mod}$ , and  $m$  is an integer. For suitable choice of plasma density  $\bar{N}_{e,0}$ , channel modulation period  $d_{mod}$ , and mode number  $m$ , the phase velocity of the axial mode can be set such that  $v_p \leq c$ . The guided pulse phase velocity can, therefore, be set equal to the velocity of an externally injected relativistic electron bunch. If the injected pulse has a significant axial field component, for example a radially polarized  $TEM_{01}^*$  mode, then the electron will gain energy from the laser as the two co-propagate.

The attractiveness of the QPM-DLA technique stems from the essentially linear energy gain of the electron bunch with the laser field strength. A simple scaling law for the energy gain in the QPM-DLA process was developed by York *et al.* [12] by considering the maximum energy gain  $\Delta E_{DLA}$  of a highly relativistic test electron accelerated in a modulated channel,

$$\frac{\Delta E_{DLA}}{m_e c^2} \sim 4\delta a_0 \left(\frac{\sigma_z}{w_{ch}}\right) \left(\frac{\lambda_p}{\lambda_0}\right)^2 \left(1 + \frac{2\lambda_p^2}{\pi^2 w_{ch}^2}\right)^{-2} \quad (1.22)$$

where  $\delta = \frac{N_{e,max} - \bar{N}_{e,0}}{\bar{N}_{e,0}}$  is the modulation depth of the corrugated plasma waveguide,  $a_0$  is the laser normalized vector potential,  $\sigma_z$  is the longitudinal extent of the laser pulse,  $\lambda_p$  is the plasma wavelength, and  $\lambda_0$  is the laser wavelength. This can be compared to the scaling law for wakefield acceleration given above by equation (1.21). For typical experimental parameters  $\lambda_0 = 800 \text{ nm}$ ,  $w_{ch} = 15 \text{ }\mu\text{m}$ ,  $a_0 = 0.25$ ,  $\frac{\sigma_z}{c} = 300 \text{ fs}$  corresponding to a 1.9 TW laser power,  $\bar{N}_{e,0} = 7 \times 10^{18} \text{ cm}^{-3}$ ,  $\delta = 0.9$ , and a modulation period  $d_{mod} = 349 \text{ }\mu\text{m}$ , York *et al.* [12] calculate a peak energy gain of  $\frac{\Delta E_{DLA}}{m_e c^2} \sim 1000$ . This is comparable to the energy gain  $\frac{\Delta E_{LWFA}}{m_e c^2} \sim 750$  calculated in [77] for a wakefield accelerator driven by a 7.16 TW laser in a suitable plasma channel. However, the linear dependence of  $\Delta E_{DLA}$  on  $a_0$  implies that even with peak powers  $\sim 10 \text{ GW}$  typical of common CPA regenerative amplifiers,  $\frac{\Delta E_{DLA}}{m_e c^2} \sim 50$ . In this energy range, the highly nonlinear wakefield accelerator is generally unable to operate.

The initial velocity of the externally injected electron bunch is an important requirement for a successful proof of principle QPM-DLA experiment. For a fixed modulation period,  $d_{mod}$ , and fixed longitudinally averaged plasma density,  $\bar{N}_{e,0}$ , over the length of the accelerator, changes in the electron velocity due to acceleration by the laser field will cause it to dephase unless the electron is already sufficiently relativistic (and thus does not experience a significant change in velocity due to

acceleration). This can be quantified by a trapping condition on the electron bunch which requires that the bunch Lorentz factor satisfy

$$\gamma_{th} \cong \left( \frac{k_m w_{ch}}{4\delta a_0} \right) \left( \frac{N_{cr}}{\bar{N}_{e,0}} \right)$$

where  $a_0$  is the laser normalized vector potential ( $a_0 \ll 1$ ) [84,85]. In practice, this leads to a requirement for already highly relativistic electron beams. For example, for a modulation period  $d_{mod} = 350 \mu m$ , modulation depth  $\Gamma = 0.9$ , laser spot size  $w_{ch} = 12 \mu m$ , laser normalized amplitude  $a_0 = 0.1$ , laser critical density  $N_{cr} = 1.7 \times 10^{21} cm^{-3}$  for an 800 nm Ti:Sapphire drive laser, and  $\bar{N}_{e,0} = 1 \times 10^{19} cm^{-3}$  we find that  $\gamma_{th} = 102$ , so the injected electron beam must have an energy of at least  $\sim 50$  MeV to experience linear energy gain in the modulated waveguide. Yoon et al. [85] showed that the required initial electron momentum can be drastically reduced by using a ramped plasma density or, equivalently, a ramped modulation period to phase match the interaction between the laser pulse and accelerating electron beam as the electron velocity increases. Indeed, PIC simulations performed by Yoon et al. demonstrated the feasibility of using density ramps to trap and accelerate electron bunches with initial energy as low as 5 MeV.

The seed electron source has proven to be a significant impediment to a proof of concept demonstration of the QPM-DLA technique. The seed source should be at least 5 MeV to satisfy the initial trapping threshold given suitable ramping of the plasma density or modulation period. For highest efficiency the bunch duration should be significantly shorter than the  $\sim 100$  fs drive pulse duration. Further, femtosecond scale synchronization with the drive pulse is required, which implies an optically generated, or at least optically triggered, seed electron source. Finally, since

potential high repetition rate operation is the hallmark of the QPM-DLA scheme, a seed source capable of high repetition rate is ideal. The standard wakefield accelerators described in Sec. 1.2 meet the first three requirements, but the  $>100$  mJ laser systems used to drive these accelerators are not readily available at high repetition rates. The low divergence and energy spread available from wakefield accelerators is actually something of a drawback as an injector for the QPM-DLA scheme. This type of seed beam demands extremely precise alignment into the corrugated waveguide and precise matching of the modulation period to the accelerated beam energy, assuming the beam energy is not already high enough that a ramped modulation period is unnecessary.

The high density self-modulated wakefield accelerator presented in Chapter 6 of this dissertation is a good candidate as an ultra-short, femtosecond synchronized, high repetition rate injector for a QPM-DLA experiment. The experiments presented make use of the scaling laws for relativistic self-focusing and self-phase modulation to drive a high amplitude plasma wave with sub-terawatt,  $\sim 10$  mJ laser pulses in a high density ( $> 10^{20} \text{ cm}^{-3}$ ) plasma. Wave breaking and self-injection lead to  $\sim 500$  pC electron beams with exponential energy distributions reaching well above the required 5 MeV threshold in a moderately collimated beam with  $\sim 200$  mrad divergence angle. Thus, between the plasma channel generation results presented in Chapter 3, the modulation techniques and quasi-radially polarized mode guiding presented in Chapter 4, and the high repetition rate seed source presented in Chapter 6, all the components necessary for a proof of principle QPM-DLA experiment have been demonstrated.



## Chapter 2: The UMD 25 TW Laser System

### **2.1 Overview of high peak power, femtosecond laser systems**

#### **– Chirped Pulse Amplification and Ti:Sapphire lasers**

The field of intense laser-plasma interactions has been enabled by the rapid advancement and availability of multi-terawatt femtosecond laser systems [86,87]. Indeed, within the past decade a number of commercially available systems capable of reaching relativistic intensities have come to market, moving the tools required for studying relativistic optics from large facilities into university laboratories. The vast majority of these systems are based on Ti:Sapphire ( $\text{Ti:Al}_2\text{O}_3$ ) gain media employing the chirped pulse amplification (CPA) technique [8,86,87]. Ti:Sapphire was developed in the mid-1980s as a solid state lasing medium and has become the gain medium of choice for nearly all multi-terawatt femtosecond laser systems primarily due to its extremely broad gain bandwidth which allows lasing between 670-1070 nm. Due to this broad bandwidth, Ti:Sapphire oscillators have been demonstrated to support pulses as short as two optical cycles [88,89], and commercial oscillators operating with pulse durations  $\sim 20$  fs are now ubiquitous. Other optical and mechanical properties, such as a large stimulated emission cross section, large saturation fluence, and high thermal conductivity make Ti:Sapphire an excellent choice for use as a gain medium in laser amplifiers [9,90]. The fluorescence lifetime of Ti:Sapphire, however, is short, only 3.2  $\mu\text{s}$ , which means pulsed laser systems are generally required as a pump with the absorption band peaking around 500 nm.

Peak powers in the multi-terawatt regime generally require multiple stages of amplification. Direct amplification of femtosecond pulses is severely limited by

nonlinear phase accumulation, which can lead to severe beam distortion or self-focusing and laser crystal damage. The CPA technique [7,8] avoids these issues by first applying a large linear chirp to the ultrashort pulse prior to amplification, typically stretching the pulse by a factor of  $\sim 1000$ . The resulting pulse peak intensity is small enough to be amplified without risking damage to the amplifier rods. A pulse compressor then removes the linear chirp applied by the stretcher and any material dispersion in laser chain, ideally returning the amplified pulse to its original femtosecond-scale duration.

## **2.2 UMD 25 TW Ti:Sapphire Laser Architecture**

All of the experiments in this dissertation were performed using a 25 TW Ti:Sapphire laser system delivering a maximum of 0.9 J on target with a full width at half maximum pulse duration as short as 39 fs. The system was designed as a 20 TW system by Coherent, Inc. It was subsequently upgraded to a 25 TW system using a more energetic pump laser, and incorporating a deformable mirror – wave front sensor loop for phase front control and a Fastlite Dazzler acousto-optic phase modulator for adaptive spectral phase control. The system architecture, depicted in Fig. 2.1, employs a standard CPA design. The output of a Coherent Micra femtosecond oscillator is stretched and amplified in a Coherent Legend regenerative amplifier followed by amplification in a four pass bowtie amplifier. After amplification the pulse is compressed back to 39 fs with a time-bandwidth product of  $\Delta t_{FWHM} \Delta \nu_{FWHM} \cong 0.472$ . A pulse with a Gaussian spectral amplitude will have a time bandwidth product of  $\Delta t_{FWHM} \Delta \nu_{FWHM} \cong 0.441$ , which for our 26 nm FWHM amplified bandwidth corresponds to a 36.5 fs FWHM pulse duration.

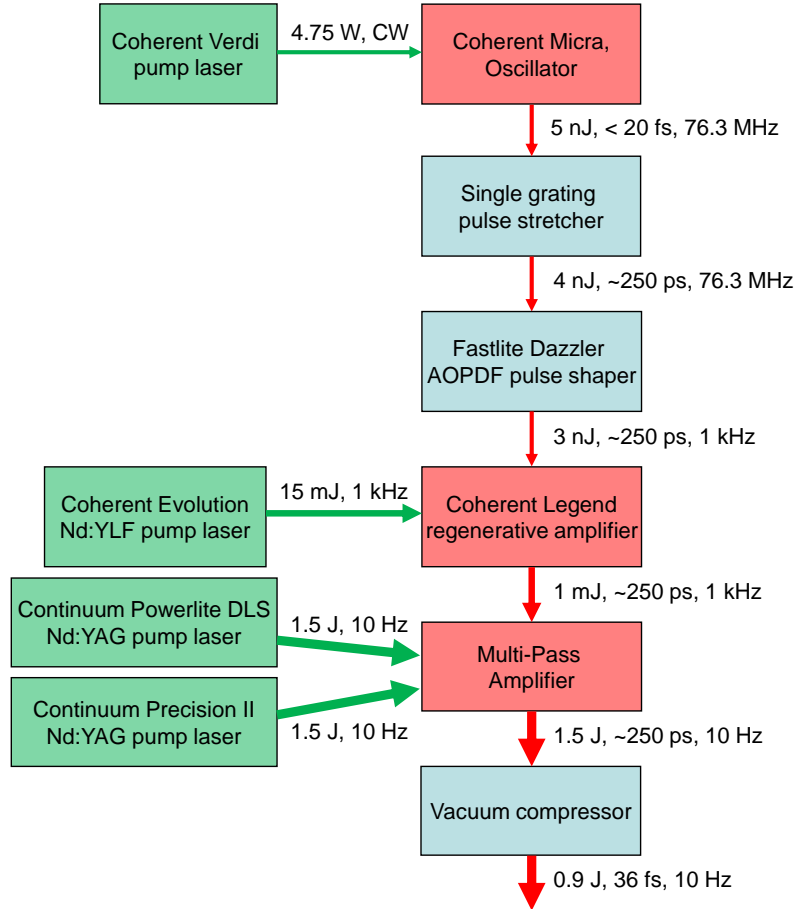


**Figure 2.1.** Block diagram of the 25 TW laser system used to perform the experiments in this dissertation.

The Coherent Micra is a Kerr lens modelocked femtosecond oscillator pumped by a 4.75W continuous wave Nd:YVO<sub>4</sub> laser (Coherent Verdi). It delivers <20 fs pulses with bandwidths ~80 nm centered at 790 nm. The Micra operates at a repetition rate of 76.3 MHz with output pulses synchronized to the oscillator of a home built ~140ps Nd:YAG laser system, described at the end of this chapter. Intra-cavity bandwidth tuning is achieved through a pair of Brewster prisms which compensate for the material dispersion within the cavity.

The ~5 nJ, < 20 fs pulses from the Micra are sent through a Faraday isolator to a single grating stretcher which adds positive group delay dispersion, stretching the

pulse to ~250 ps. After the stretcher, the pulse passes through an acousto-optic phase modulator (Fastlite Dazzler) which is used to correct higher order spectral phase from the laser chain. The use of the Dazzler for pulse shaping will be discussed in detail below. After phase modulation the pulse is injected into a 1 kHz regenerative (regen) amplifier (Coherent Legend) pumped by a 15 W, Q-switched Nd:YLF laser (Coherent Evolution). Electro-optic Pockels cells enable controlled switching of the seed pulse into the regen cavity and switching out of the amplified pulse. The Pockels cells operate by applying a ~1 ns rise time high voltage pulse across a KD\*P crystal. The electro-optic (Pockels) effect is an electric field-induced birefringence in the KD\*P crystal. The voltage (electric field) and thickness of the KD\*P are tuned for half wave rotation after double passing the crystal. High contrast polarizing optics within the regen cavity then trap the seed pulse only when its polarization has been rotated by the switch in Pockels cell. After a sufficient number of round trips within the cavity (approximately 24 in our system) the gain saturates and the switch out Pockels cell is fired, rotating the pulse polarization back to vertical and rejecting the amplified pulse out of the resonator. The pulse is amplified in the regen to ~800  $\mu$ J, providing a total gain of  $\sim 10^5$  with a nanosecond pre-pulse contrast of  $\sim 1000:1$ .

The strong gain within the regenerative amplifier affects the spectral characteristics of the amplified pulse. The fluence of the k-th pass through the amplifier is given by

$$I_k = TI_S \ln\{e^{g_0(\omega)L} [e^{I_{k-1}/I_S} - 1] + 1\} \quad (2.1)$$

where  $T$  is the transmission in a single resonator round trip,  $I_S$  is the saturation fluence (1 J/cm<sup>2</sup> for Ti:Sapphire), and  $g_0(\omega)$  is the frequency dependent small signal gain

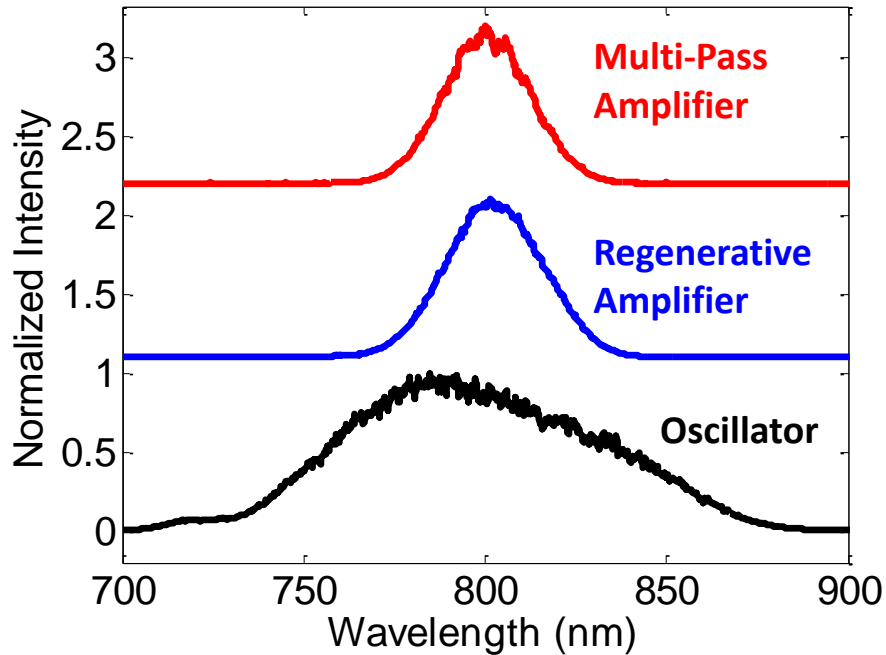


**Figure 2.2.** Spectrum of the laser pulse at various points in the amplification chain. Gain narrowing reduces the spectral bandwidth in the regenerative and multi-pass amplifiers to a final bandwidth of 26 nm, with the majority of the narrowing occurring in the regenerative amplifier. Gain shifting, again primarily in the regenerative amplifier, shifts the center wavelength from 790 nm in the oscillator to 808 nm after amplification.

coefficient [91]. The frequency dependence of the small signal gain coefficient leads to a large difference in the final amplification near the peak of the Ti:Sapphire gain curve compared to the wings [92–94]. This effect, known as gain narrowing, can lead to drastic reduction in the amplified pulse bandwidth. As evidenced by Fig. 2.2, gain narrowing reduces the pulse bandwidth from the ~80 nm FWHM oscillator bandwidth to 34 nm FWHM after the regenerative amplifier.

Second, gain saturation in the last few passes through the regenerative amplifier shifts the center of the pulse spectrum from an 800 nm center wavelength to ~808 nm. With a positive chirp on the seed pulse, the redder frequencies arrive at the amplifier rod before the bluer frequencies. At gain saturation this means the red frequencies experience a larger gain than the blue frequencies, thereby red-shifting

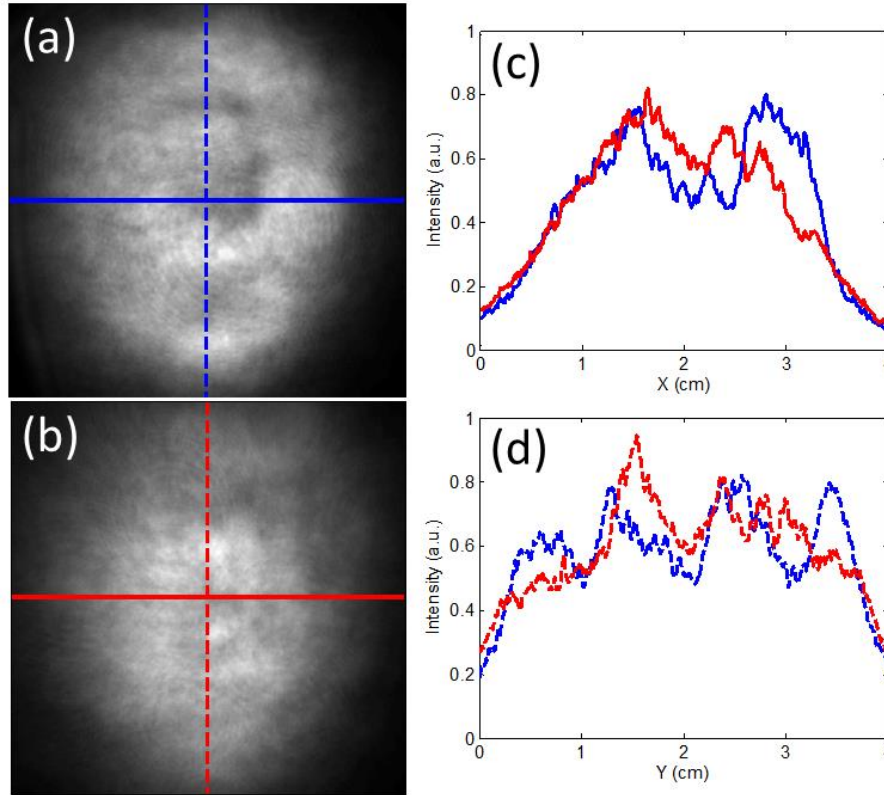


**Figure 2.3.** Amplified and expanded beam profile before (a) and after (b) implementing a vertical beam inversion after the second pass of the MPA. Lineouts along the x (c) and y (d) axes show a moderate improvement in the beam uniformity after the beam flip.

the entire pulse spectrum [93]. Gain narrowing in the regenerative amplifier is a particular issue in this system as it represents the main factor limiting the achievable pulse duration.

The pulse proceeds from the regenerative amplifier through an external Pockels cell into a bowtie configuration multipass amplifier (MPA). The external Pockels cell reduces the pulse repetition rate from 1 kHz to 10 Hz and improves the nanosecond pre-pulse contrast from the regen to better than  $10^6:1$ . The Gaussian mode beam from the regenerative amplifier is then expanded to a 2.5 mm FWHM and executes four passes through the MPA's 1" diameter Ti:Sapphire rod. After the second pass, a periscope flips the beam vertically to average out any top-bottom

spatial irregularities. The effect of the periscope addition to the MPA is shown in Fig. 2.3 which shows the amplified beam profile. The total energy before and after addition of the periscope was unchanged. The MPA's Ti:Sapphire rod is symmetrically end-pumped by two 10 Hz, Q-switched, frequency doubled Nd:YAG laser systems delivering 1.5 J each at  $\lambda=532$  nm. The pump beams are relay imaged with a slight demagnification so that they have a 9 mm diameter top hat profile at the MPA rod. Gain in the MPA was simulated by iteratively solving equation (2.1) starting with the measured beam profile and energy from the regen output. The pulse energy after each pass, shown in Fig. 2.4(a), shows saturation on the last pass through the MPA with total output energy of 1.43 J and 47% extraction efficiency. The measured beam out of the MPA has a  $\sim 9$  mm diameter top hat profile, shown in Fig. 2.4(b), and measured pulse energy of 1.4 J.

After amplification, the beam passes through a waveplate – thin film polarizer (TFP) combination which is used for laser pulse energy control during experiments.

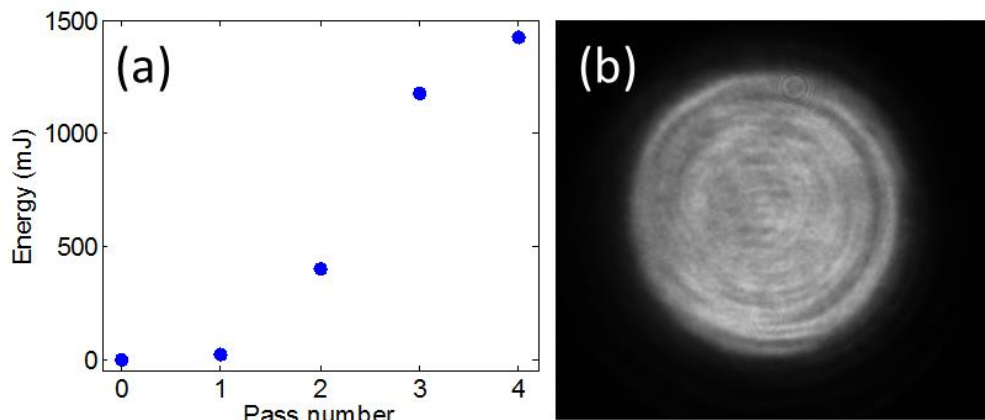


**Figure 2.4.** (a) Theoretical energy output per pass in the MPA pumped by two 9 mm diameter, 1.5 J frequency doubled Nd:YAG lasers. The seed pulse reaches gain saturation on the fourth pass. (b) Measured seed beam profile after the fourth and final pass through the MPA crystal. The pulse energy is 1.4 J.

The TFP, when used in transmission, has a fairly poor extinction ratio of only 9:1. However, the pulse compressor is polarization dependent and attenuates any vertically polarized component of the laser pulse with ~1% transmission. Before entering the pulse compressor, the amplified beam is expanded to a 4 cm diameter to reduce the total fluence on the compressor gratings below 100 mJ/cm<sup>2</sup>, the rule-of-thumb maximum fluence for gold gratings [95]. Pulse compression is achieved using a Treacy-style grating compressor [96] housed in a vacuum chamber (the “vacuum compressor”) with approximately 63% energy throughput. Maximum on-target energy of 900 mJ and pulse duration of 39 fs produces a maximum 25 TW peak power on target.

## ***2.3 Spectral phase compensation using an acousto-optic modulator***

### **2.3.1 Dispersion and higher order spectral phase in femtosecond laser pulses**

An electric field component of a general laser pulse at a fixed point in space can be described in the time domain as

$$E_{laser}(t) = E_0(t)e^{-i\omega_0 t + \Phi(t)}$$

where  $E_0(t) = \sqrt{I(t)}$  is the electric field amplitude,  $I(t)$  is the laser intensity,  $\omega_0$  is the carrier frequency, and  $\Phi(t)$  is the pulse temporal phase. Similarly, the spectral representation of the pulse,  $\tilde{E}(\omega)$ , can be written in terms of a complex spectral amplitude and phase as

$$\tilde{E}(\omega) = \tilde{E}_0(\omega)e^{i\phi(\omega)}.$$



The time domain pulse representation is linked to its frequency domain counterpart through the Fourier transform pair

$$E(t) = \frac{1}{2\pi} \int_{-\infty}^{\infty} \tilde{E}(\omega) e^{-i\omega t} d\omega$$

$$\tilde{E}(\omega) = \int_{-\infty}^{\infty} E(t) e^{i\omega t} dt.$$

From this relationship we can see that complete characterization of the pulse can be achieved through measurement of the pulse amplitude and phase in either the time or frequency domain. The spectral phase  $\phi(\omega)$  can be expanded in powers of  $(\omega - \omega_0)$  as

$$\phi(\omega) = \phi_0 + (\omega - \omega_0)\phi_1 + \frac{(\omega - \omega_0)^2\phi_2}{2} + \frac{(\omega - \omega_0)^3\phi_3}{3!} \dots$$

where  $\phi_n = \frac{d^n \phi}{d\omega^n}$ . The zero order term,  $\phi_0$ , represents a constant phase offset of the carrier frequency with respect to the peak of the pulse envelope or some other reference time, and is thus called the “carrier-envelope” phase. The first order dispersion  $\phi_1$  represents a delay in the time domain. The second order dispersion, or group delay dispersion (GDD), describes a linear frequency chirp in the time domain. Higher order dispersions ( $\phi_3, \phi_4, etc.$ ) yield nonlinear frequency chirps and more complicated time domain pulse shape distortions. For an arbitrary spectral amplitude,  $\tilde{E}(\omega)$ , the shortest pulse duration in the time domain will occur when the spectral phase is linear, meaning that  $\phi_2$  and higher order dispersion terms in  $\phi(\omega)$  all vanish. Therefore, in short pulse CPA systems careful attention must be paid to dispersion management along the amplifier chain.

In any CPA chain, the pulse picks up spectral phase from dispersive elements, such as the gratings in a pulse stretcher and compressor, as well as from material dispersion inside the laser chain. A pulse propagating through an optical medium of length  $L$  will distort in the time domain due to the dependence of the refractive index on wavelength where the accumulated higher order spectral phase is given by

$$\begin{aligned}\phi_2 &= \frac{\lambda^3 L}{2\pi c^2} \frac{d^2 n}{d\lambda^2}, \\ \phi_3 &= -\frac{\lambda^4 L}{4\pi^2 c^3} \left( 3 \frac{d^2 n}{d\lambda^2} + \lambda \frac{d^3 n}{d\lambda^3} \right), \\ \phi_4 &= \frac{\lambda^5 L}{8\pi^3 c^4} \left( 12 \frac{d^2 n}{d\lambda^2} + 8\lambda \frac{d^3 n}{d\lambda^3} + \lambda^2 \frac{d^4 n}{d\lambda^4} \right).\end{aligned}$$

Additionally, most grating stretchers and compressors will add higher order spectral phase due to optical aberrations [97,98]. The total spectral phase accumulated along the laser chain is then the sum of the spectral phase accumulated from the stretcher, material dispersion, and the compressor

$$\phi_{total}(\omega) = \phi_{stretcher}(\omega) + \phi_{material}(\omega) + \phi_{compressor}(\omega) \quad (2.2)$$

where

$$\phi_{material}(\omega) = \sum_{i=1}^N n_i(\omega) \frac{\omega}{c} L_i$$

is the spectral phase accumulated from each of the  $N$  components the pulse passes through. Like orders can be grouped in equation (2.2) so that

$$\begin{aligned}\phi_{2,total} &= \phi_{2,stretcher} + \sum_{i=1}^N \frac{\lambda^3 L_i}{2\pi c^2} \frac{d^2 n_i}{d\lambda^2} + \phi_{2,compressor} \\ \phi_{3,total} &= \phi_{3,stretcher} - \sum_{i=1}^N \frac{\lambda^4 L_i}{4\pi^2 c^3} \left( 3 \frac{d^2 n_i}{d\lambda^2} + \lambda \frac{d^3 n_i}{d\lambda^3} \right) + \phi_{3,compressor}\end{aligned}$$

$$\phi_{4,total} = \phi_{4,stretcher} + \sum_{i=1}^N \frac{\lambda^5 L_i}{8\pi^3 c^4} \left( 12 \frac{d^2 n_i}{d\lambda^2} + 8\lambda \frac{d^3 n_i}{d\lambda^3} + \lambda^2 \frac{d^4 n_i}{d\lambda^4} \right) + \phi_{4,compressor}$$

A properly designed stretcher-compressor pair will ideally be able to satisfy

$$\phi_{2,total} = \phi_{3,total} = \phi_{4,total} = 0 \text{ so as to achieve the shortest pulse possible.}$$

In practice, it is difficult to fully compensate for material dispersion using simple grating based stretcher and compressor pairs. Fundamental to the CPA technique is the addition and compensation of quadratic spectral phase or chirp by the stretcher and compressor, and fine adjustments to the incidence angle in the compressor can partially compensate for cubic spectral phase. However, uncompensated third and fourth order spectral phase can cause significant pulse distortion in the time domain. This section describes the measurement and compensation of higher order spectral phase components in our laser chain using the frequency resolved optical gating (FROG) technique for pulse measurement and an acousto-optic programmable dispersive filter (AOPDF) for spectral phase compensation.

### 2.3.2 Second harmonic FROG

Modelling of ultrashort laser-plasma interaction experiments requires a complete diagnosis of the pulse shape in the time domain. A number of femtosecond pulse measurement techniques have been proposed and demonstrated with wide variation in accuracy and complexity [99–102]. Femtosecond scale characterization of the amplified pulse shape was performed using the second harmonic generation frequency resolved optical gate (SHG FROG) technique, based on the simplicity of

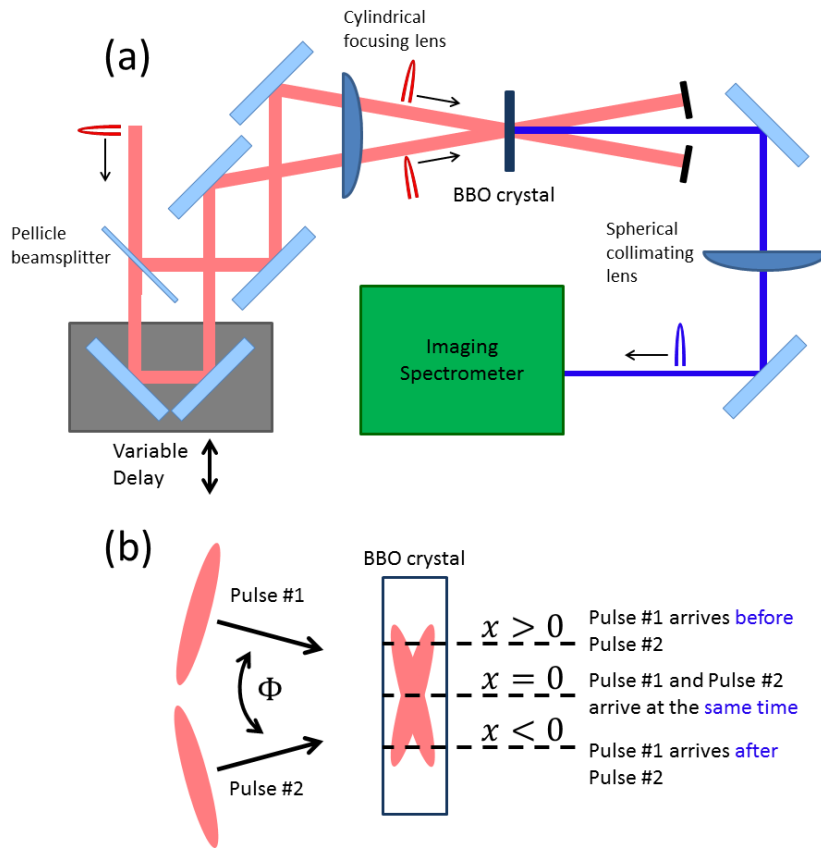


**Figure 2.5.** (a) A schematic of the single shot SHG FROG used for characterization of the pulse spectral amplitude and phase. The pulse is split using a thin pellicle beamsplitter and focused using a cylindrical lens into a BBO crystal. Focusing using a cylindrical lens allows the time delay,  $\tau$ , to be mapped onto the geometrical dimension,  $x$ , perpendicular to the direction of focusing as illustrated in (b). The sum frequency signal pulse is imaged to the entrance slit of an imaging spectrometer to form the complete SHG FROG spectrogram in a single shot.

the measurement and the ability of the SHG FROG to fully reconstruct the ultrashort pulse in the time domain. The SHG FROG produces a time-frequency spectrogram by spectrally resolving an autocorrelation of the measured pulse. The FROG signal takes the form

$$I_{FROG}(\omega, \tau) = \left| \int_{-\infty}^{\infty} E(t - \tau)E(t + \tau) \exp(-i\omega t) dt \right|^2,$$

where  $E(t)$  is the time dependent laser electric field and  $\tau$  represents the delay between the pulse arrival times in the SHG crystal, as shown in Fig. 2.5, which is

mapped onto a spatial dimension of the SHG signal by the crossing of the two beams in the BBO crystal. The delay,  $\tau$ , is related to the crossing angle,  $\Phi$ , and the transverse distance across the crystal,  $x$ , by  $\tau = \frac{nx \sin(\Phi/2)}{c}$  where  $n$  is the crystal refractive index,  $c$  is the speed of light, and  $x = 0$  at the location in the crystal where the two pulses arrive at the same time. The SHG signal is imaged from the crystal to the entrance slit of an imaging spectrometer which spectrally resolves the SHG signal at each delay point to form the full FROG spectrogram.

Reconstruction of the pulse amplitude and phase was performed using commercial reconstruction software [103] with measured spatial and spectral calibrations. The problem of retrieving pulse amplitude and phase from a FROG trace has been shown to be equivalent to the 2D phase retrieval problem frequently encountered in image processing [102], and the software implements the method of generalized projections to solve this reconstruction problem. The reconstruction accuracy can be quantified by the ‘‘FROG error’’ defined by

$$G = \sqrt{\frac{1}{N^2} \sum_{i,j=1}^N |I_{meas}(\omega_i, \tau_j) - \mu I_{ret}(\omega_i, \tau_j)|^2}$$

where  $I_{meas}(\omega_i, \tau_j)$  is the measured FROG spectrogram,  $I_{ret}(\omega_i, \tau_j)$  is the spectrogram retrieved by the algorithm, and  $\mu$  is a normalizing constant that minimizes  $G$  [102]. This is effectively a measurement of the sum of squares error between the measured and retrieved FROG traces. A FROG error below 1% of the peak intensity of the FROG trace is generally considered as an acceptable reconstruction.

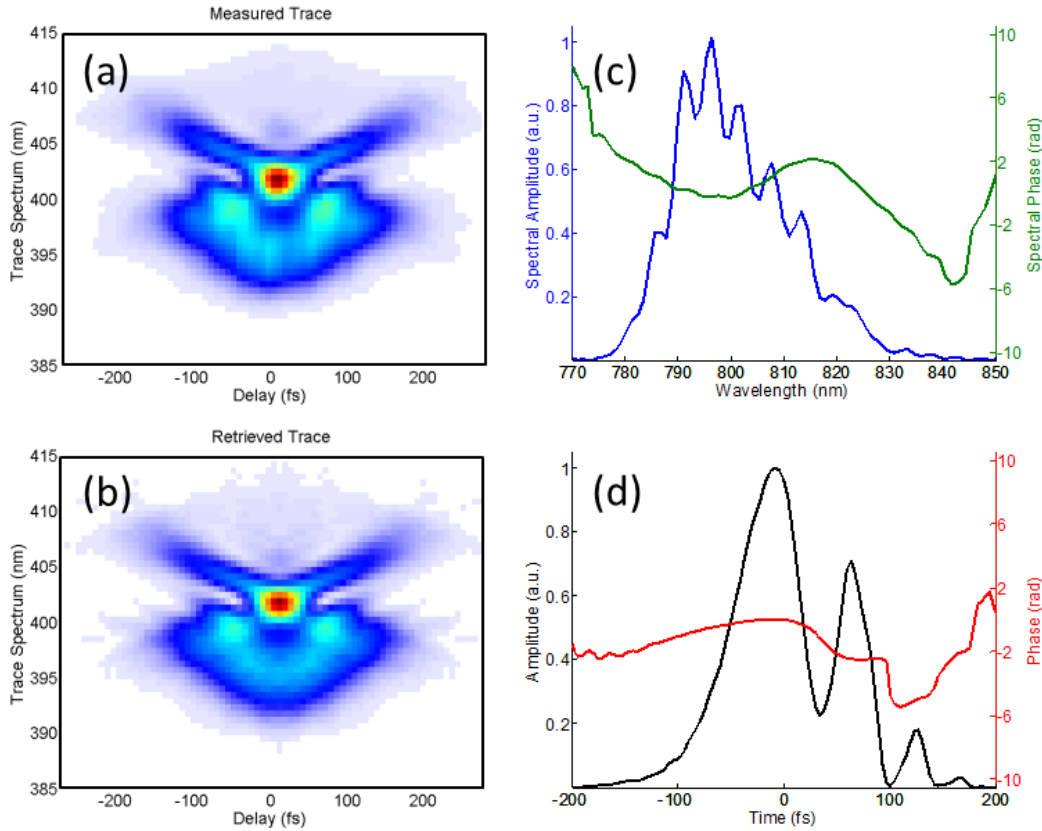


**Figure 2.6.** SHG FROG measurement of a pulse exhibiting strong cubic spectral phase. The measured trace (a) and retrieved trace (b) closely match, with a FROG error of 0.006. Extracted spectral domain (c) and time domain (d) representations of the pulse electric field amplitude and phase show the effect of non-negligible third order spectral phase.

A sample FROG trace is shown in Fig. 2.6(a) with the reconstructed FROG trace shown in Fig. 2.6(b). The frequency domain amplitude and phase corresponding to the reconstructed FROG trace are shown in Fig. 2.6(c), and the time domain pulse intensity and phase are shown in Fig. 2.6(d). The spectral phase of the measured pulse in Fig. 2.6 exhibits a strong cubic dependence which causes the multi-peaked structure seen in the time domain representation of the pulse. The SHG FROG geometry suffers from an ambiguity in the direction of time caused by the trace symmetry with respect to delay. Thus, the subsidiary peaks in the time domain reconstruction may have arrived either before or after the main peak.

The direction of time ambiguity can be resolved by adding a small amount of third order phase with a known sign with, for example, the acousto-optics programmable dispersive filter (AOPDF) described in the next section. Alternatively, an etalon can be inserted into the beam in advance of the SHG FROG. The etalon will generate a post pulse, so reconstruction of a FROG trace containing both pulses will fix the direction of increasing time.

### **2.3.3 Spectral phase compensation with an acousto-optic programmable dispersive filter**

As mentioned above, higher order components of the pulse spectral phase, arising mainly from material dispersion, can be difficult to compensate and will distort an ultrashort pulse away from its bandwidth-limited duration. Figure 2.6(d) shows an example of our pulse with temporal “wings” caused mainly by uncompensated third order phase from the amplifier chain. Novel compressor designs have been used for complete compensation of the third and fourth order spectral phase along a full CPA laser chain without the use of adaptive pulse shaping [97,98]. However, these designs can be complicated and adaptive pulse shaping methods have shown great flexibility in compensating spectral phase in CPA systems without necessitating perfect stretcher-compressor matching [104–106]. These methods can also control spectral amplitude, allowing for mitigation of effects such as gain narrowing and gain shifting [106].

An acousto-optic programmable dispersive filter (AOPDF) was installed in the laser chain between the stretcher and regenerative amplifier. The AOPDF (Fastlite Dazzler [107]) is comprised of a programmable RF signal generator and a

piezoelectric transducer attached to a bulk birefringent crystal. The RF pulse applied to the transducer generates a sound wave in the birefringent crystal counter-propagating to the incident optical pulse. If the RF pulse is of a single frequency, the incident optical pulse, polarized along the ordinary birefringence axis, undergoes Bragg scattering and couples to an extraordinary wave. The phase matching condition for Bragg scattering in the crystal is  $\mathbf{k}_2 \cong \mathbf{k}_1 + \mathbf{q}$ , where  $\mathbf{k}_1$  is the incident optical wave vector,  $\mathbf{k}_2$  is the scattered optical wave vector, and  $\mathbf{q}$  is the acoustic wave vector. Further, the frequencies must satisfy the energy conservation relation  $\omega_2 = \omega_1 + \Omega$ . The Bragg condition is satisfied for only a narrow frequency band in the optical pulse, so in this configuration the RF pulse acts as a programmable optical filter where the optical frequency selection is controlled through the RF frequency of the acoustic wave. Since  $\omega_1 \gg \Omega$  the optical frequency remains effectively unchanged, but the amplitude and phase at  $\omega_1$  of the extraordinary-coupled optical field *is* changed.

For pulse shaping in the AOPDF, a programmable, chirped RF pulse is used to satisfy the Bragg condition across a broad optical bandwidth within the birefringent crystal [106,108,109]. The variation in the instantaneous frequency of the RF pulse within the crystal controls the longitudinal position in which a selected optical frequency will be scattered from an ordinary into an extraordinary wave. This, in turn, controls the relative delay between frequency components in the optical pulse. Thus, the maximum time window over which the AOPDF can shape the optical pulse is given by the difference in optical transit times between the ordinary and extraordinary axes of the birefringent crystal. For our Dazzler this is an



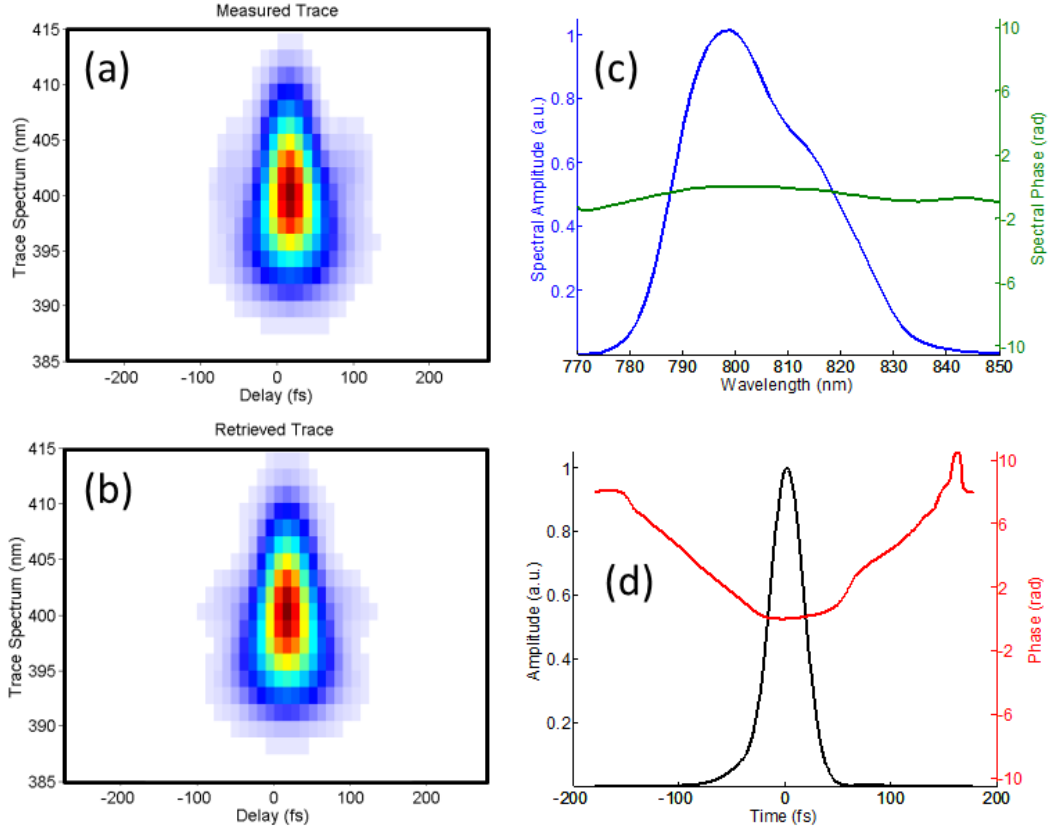


**Figure 2.7.** Measured (a) and retrieved (b) SHG FROG traces after spectral phase compensation by the Dazzler AOPDF. The retrieved spectral phase (c) is much flatter and the retrieved temporal intensity envelope (d) is nearly bandwidth limited with FWHM pulsewidth 39 fs.

approximately 8 ps time window. More precisely, the acousto-optic interaction leads to terms in the frequency domain wave equation of the form

$$S_2(\omega_2) \exp[i(k_2z - \omega t)] \propto S_1(\omega_1) \exp[i(k_1z - \omega_1 t)] \times S_{ac}(\Omega) \exp[i(qz - \Omega t)]$$

where  $S_1$  and  $S_2$  are the incident and scattered complex spectral amplitudes for the optical waves and  $S_{ac}$  is the complex spectral amplitude for the acoustic wave [108].

Given the phase matching conditions this leads to  $S_2(\omega_2) = S_1(\omega_1) S_{ac}(\Omega)$ . In the time domain the scattered optical wave is a convolution of the incident optical wave with the acoustic wave. Therefore, given known input,  $S_1(\omega_1)$ , and a required output,  $S_2(\omega_2)$ , the required acoustic filtering function,  $S_{ac}(\Omega)$  can be easily

computed. With RF pulses in the ~50 MHz range with ~20 MHz bandwidths, pulse shaping over optical bandwidths >100 nm centered at 800 nm can be achieved, allowing for pulse shaping even in the few cycle regime [110].

The Fastlite Dazzler AOPDF installed between the stretcher and regen was used in conjunction with pulse measurements by an SHG FROG to compensate for higher order dispersion in the amplifier chain. For initial pulse measurements an RF waveform compensating for the material dispersion within the Dazzler crystal was used and the SHG FROG was placed after the vacuum compressor. The FROG trace and reconstructed pulse shown in Fig. 2.6 show temporal wings associated with uncompensated higher order phase, mainly 3<sup>rd</sup> order. The measured spectral phase was then fed back into the Dazzler software controlling the RF waveform in the AOPDF. This procedure was iterated until a flat spectral phase at the end of the amplifier was achieved, typically only requiring two or three iterations. Figure 2.7 shows a FROG trace and reconstructed pulse after phase optimization with the Dazzler. The wings are nearly eliminated, and the FWHM pulse duration is reduced to 39 fs. The Dazzler can also be used in experiments for fine control of the time-domain pulse shape. Figure 2.8 shows a plot of the FWHM pulse duration measured in the SHG FROG as a function of GDD applied by the Dazzler. The pulse duration has a hyperbolic dependence on the GDD as expected [101], and a least squares fit gives the minimum pulse duration as 38.7 fs.

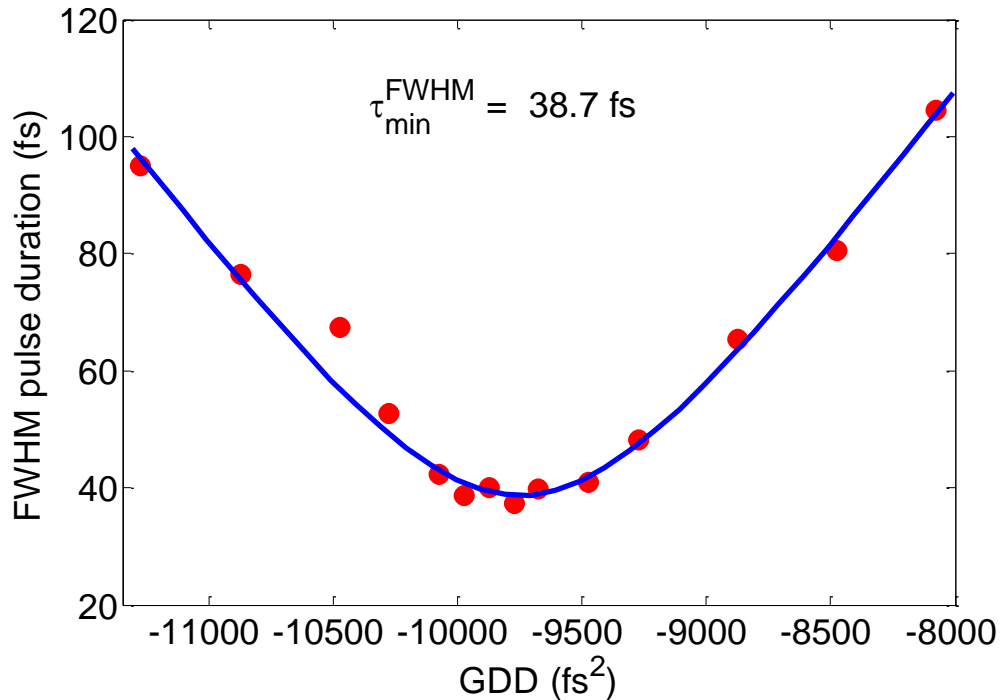


**Figure 2.8.** The FWHM pulse duration measured by the SHG FROG as a function of GDD applied by the Dazzler along with a least squares fit to a hyperbola.

## ***2.4 Laser pre-pulse characterization by third order***

### ***autocorrelation***

With peak intensities of our 25 TW laser system exceeding  $10^{19} \text{ W/cm}^2$ , ionization of a target medium can occur well in advance of the main peak of the ultrashort laser pulse. For this reason the temporal structure of the laser pulse must be well-characterized over a wide temporal window and with a high dynamic range. Particularly in laser-solid or laser-cluster interactions, where collisional ionization can play an important role, knowledge of the picosecond and nanosecond ‘pre-pulse’ contrast is important to prevent unintended plasma generation prior to the main pulse arrival.

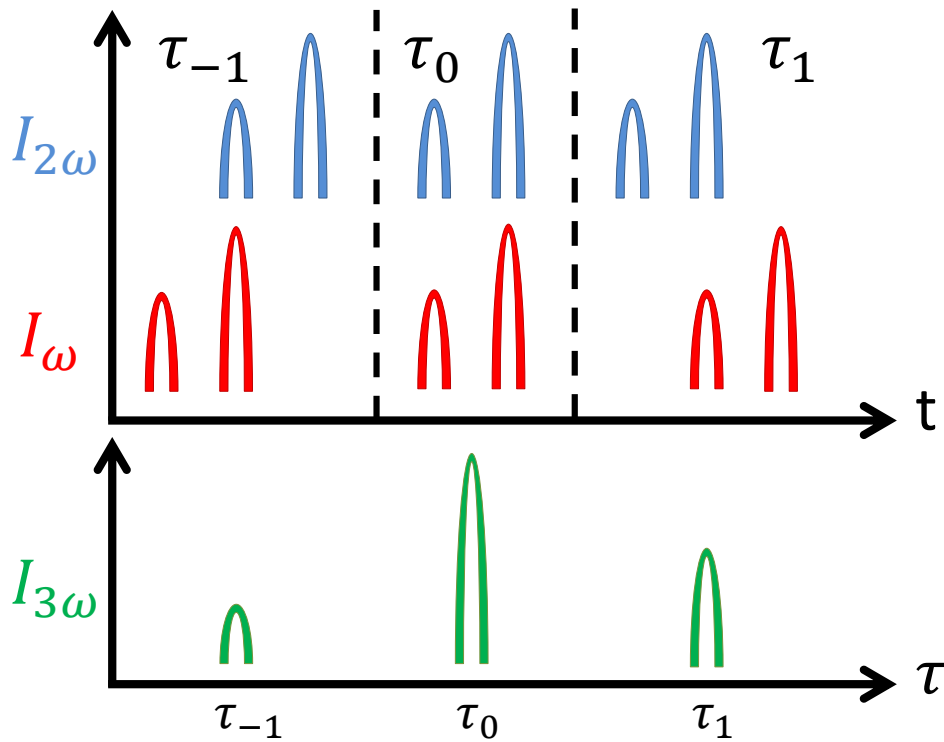


**Figure 2.9.** The third order nonlinearity in the high dynamic range autocorrelator makes pre- and post- pulses distinguishable. Overlap of the main pulse in the fundamental arm with the pre-pulse of the second harmonic arm ( $\tau_{-1}$ ) gives a third harmonic signal equal to the square of the signal from overlapping the main pulse of the second harmonic arm with the pre-pulse of the fundamental arm.

Pre-pulse and pulse pedestal measurements are made using a commercial third order scanning autocorrelator (Ultrafast Innovations [111]). For the autocorrelation measurement the beam is sent through a calibrated variable attenuator, then split into two arms, one of which is upconverted to the second harmonic while the other arm is sent through a variable delay line. The second harmonic and fundamental are then combined in a thin beta barium borate (BBO) crystal to generate a signal at the third harmonic of the femtosecond pulse. The signal is given by

$$I_{3\omega} = \int_{-\infty}^{\infty} I_{\omega}(t - \tau) I_{2\omega}(t) dt$$

and the delay,  $\tau$ , between the fundamental and second harmonic is swept to map out the third order autocorrelation function over a  $\sim 650$ ps time range.

The use of a third order nonlinearity yields advantages for high contrast pulse measurements. First, the third harmonic signal is inherently background free since neither the fundamental or second harmonic arm can make a third harmonic photon alone. This is in contrast to second harmonic or polarization gating techniques where each arm can contribute background photons at the fundamental or second harmonic frequencies. Second, the use of a third order nonlinearity breaks the symmetry between positive and negative delays in the autocorrelation function, providing an unambiguous time direction. This enables distinguishing between pre-pulses and post-pulses. As the delay of the fundamental arm is scanned across the second harmonic arm, a pre-pulse will generate two peaks in the autocorrelation function, one at the delay where the pre-pulse in the fundamental arm overlaps with the main pulse in the second harmonic arm and one at the delay where the pre-pulse in the second harmonic arm overlaps with the main pulse in the fundamental arm. This is illustrated schematically in Fig. 2.9. The main pulse to pre-pulse contrast (i.e. the ratio of the main pulse to pre-pulse intensity) in the second harmonic beam will be equal to the main pulse to pre-pulse contrast of the fundamental arm squared due to the intensity dependence of the second harmonic signal. This means the third harmonic signal amplitude which comes from overlapping the main pulse in the fundamental arm with the pre-pulse in the second harmonic arm ( $\tau_{-1}$  in Fig. 2.9) will be equal to the square of the third harmonic signal amplitude arising from an overlap of the main pulse in the second harmonic arm with a pre-pulse in the fundamental

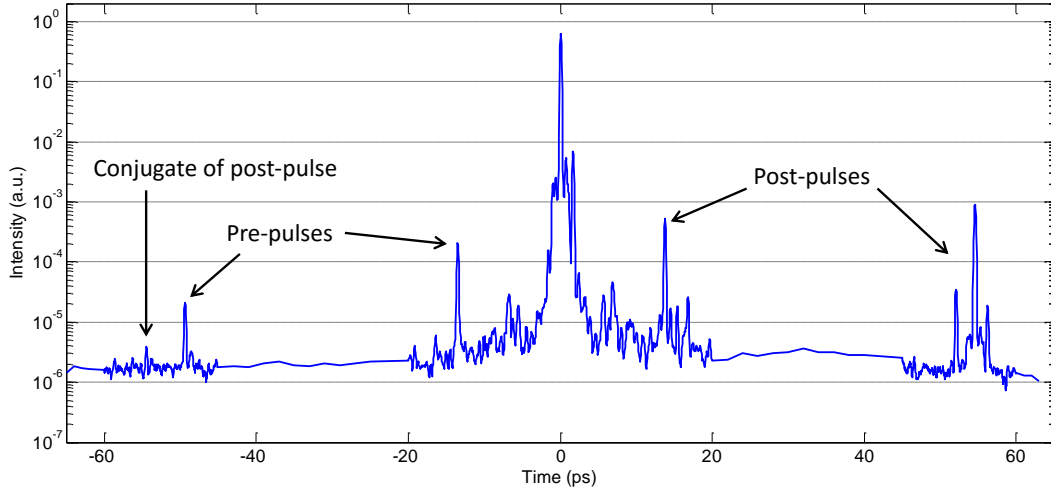


**Figure 2.10.** Sample third order autocorrelation trace of the amplified pulse. Higher resolution scans are shown around areas with known pulse structure.

arm ( $\tau_1$  in Fig 2.9). Therefore, to distinguish pre-pulses from post-pulses we look for peaks at exactly opposite delay in the autocorrelation trace. The larger of the two peaks represents the true position and contrast of the pre- or post-pulse.

Figure 2.10 shows an example third order autocorrelation trace of our 25 TW laser system. A number of features can be observed. First, the main pulse sits on a nanosecond scale pedestal at  $\sim 10^{-6}$  contrast (the measurement dynamic range is  $\sim 10^9$ ). This is a common feature of CPA laser systems and arises from amplified spontaneous emission (ASE) within the power amplifiers. Next, a post pulse at 56 ps and a pre-pulse at 48 ps are observed at the  $10^{-3}$  and  $10^{-5}$  level, respectively, along with symmetric pre- and post-pulses at 13.5 ps with a contrast of  $5 \times 10^{-4}$ . Finally, the pulse sits on a ps-scale pedestal at the  $10^{-3}$  level, which likely arises from a bandwidth mismatch on the many dielectric mirrors used through the system [112].

In experiments presented in Chapter 6 the laser was focused to  $\sim 10^{18}$  W/cm<sup>2</sup> into a high density hydrogen gas target. Since the intensity required for barrier suppression ionization in hydrogen is  $\sim 10^{14}$  W/cm<sup>2</sup> and the pulse exhibits prepulses at

13.5 ps and 2 ps with contrasts above  $10^{-4}$ , care must be taken to understand the effects of preionization in these experiments. However, since typical hydrodynamic time scales in field-ionized plasmas are  $\sim 10$ -100ps, we do not expect significant hydrodynamic motion prior to the main pulse arrival.

## **2.5 Laser wave front correction using an adaptive optics loop**

### **2.5.1 Diffraction limited focusing, $M^2$ , and Strehl ratio**

While high temporal contrast on the scale of  $10^{-3}$  or better can be obtained in the leading edge of the ultrashort pulse, achieving high *spatial* contrast at the focus often tends to be much more difficult. The spot size to which a laser can be focused is intrinsically limited by diffraction. Under the paraxial approximation, the field profile at the focal plane of a lens or curved mirror represents the Fraunhofer diffraction pattern of the input field with a magnification dependent on the focal length of the lens. If we consider a Gaussian beam focusing with a convergence half angle  $\theta$ , then the Gaussian transverse intensity profile at the focus will have a  $1/e^2$  radius  $w_0 = \frac{\lambda}{\pi\theta}$ . This is the smallest spot size achievable for a given focusing f-number ( $f/\# = \frac{f}{D} \approx \frac{1}{2\theta}$ ) and such a spot is said to be diffraction limited [91].

Spatial intensity and phase aberrations on the focusing beam will cause non-optimal interference of the component waves contributing to the net field at the focal plane, causing focal spot distortion and reduced peak fluence. A common measure of beam focusability is the  $M^2$  factor which is defined by  $w_L = M^2 \frac{\lambda}{\pi\theta} = M^2 w_0$ . Here

$w_L$  is the measured radius at the beam waist which should be calculated through the second order moment of the intensity as

$$\frac{w_L^2}{2} = \frac{\int r^2 I(r) dA}{\int I(r) dA}.$$

A realistic, aberrated beam can therefore be described as  $M^2$  times diffraction limited. A second measure of beam quality relevant to the focusing of high intensity lasers is the Strehl ratio. For small spatial aberrations the Strehl ratio is defined as the ratio of the peak intensity in the focal plane in the presence of phase front aberration to the peak intensity obtained if no phase aberration were present [86]. This measurement effectively distinguishes between focal spot degradation due to spatial phase errors from error caused by non-Gaussian intensity profiles by only referencing the measured peak intensity to the maximum achievable peak intensity with the measured intensity profile.

## **2.5.2 Correction of laser phase front aberrations using closed loop adaptive optics**

Adaptive optics loops for correcting optical aberrations have been employed in high resolution astronomical telescopes for many years with the goal of removing wave front distortions caused by the Earth's atmosphere as well as those originating from the telescope itself [113]. The goal of the adaptive optics loop is to remove wave front distortions introduced in an imaging (or focusing) system by applying a compensating wave front distortion with an additional optical element. This compensating distortion is normally applied by a "deformable mirror" which can controllably change its shape in response to an electrical or mechanical force. In order



to properly compensate the spatial phase aberrations and achieve diffraction limited imaging (focusing) the wave front must be measured using a wave front sensor of sufficient accuracy and resolution.

More recently, adaptive optics loops have been applied for correction and shaping of laser focal profiles [114–117]. There have been a number of techniques demonstrated for controlled shaping of a laser phase front profile, ranging from MEMS devices to liquid crystal spatial light modulators to more conventional piezoelectric deformable mirrors [118–120]. The large beam diameters and peak fluences of multi-terawatt to petawatt systems has necessitated use of piezoelectric and actuator driven deformable mirrors [11,86,114,115] .

Phase front measurement is achieved through either Shack-Hartmann wave front sensors or through shearing interferometry techniques [11,121,122]. Both of these techniques rely on the measurement of local phase gradients relative to a reference flat wave front. For example, the four-wave shearing interferometer (Phasics SID4) used for wave front measurement in our laser system measures the interference between different orders of a beam diffracted from a 2D grating placed in front of a CCD. The diffraction orders are slightly tilted on the CCD so that interference occurs between four slightly different parts of the incident beam. The intensity maxima in the interference pattern will move based on the incident phase gradient which can be recovered using Fourier image processing techniques. Finally, numerical integration of the recovered phase gradient yields the wave front of the beam.

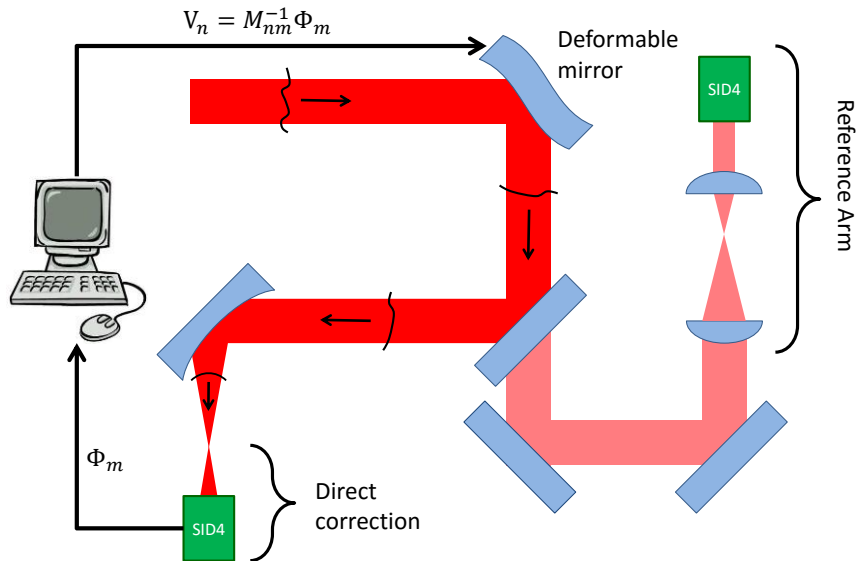


**Figure 2.11.** Schematic layout of an adaptive optics loop utilizing a reference arm for downstream aberration correction. First, a loop is closed with the SID4 behind the laser focus correcting the beam to a perfect diverging wave front. These mirror voltages are then used to obtain a reference wave front upstream of the final focusing optic. For daily operation, the loop is closed with the SID4 in this reference arm which corrects for aberrations in the full laser chain.

A closed loop adaptive optics system consisting of a bimorph deformable mirror for wave front control and a four-wave shearing interferometer for wave front measurement has been implemented on the 25 TW laser system. A schematic layout of the closed adaptive optics loop is shown in Fig. 2.11. The bimorph deformable mirror (NightN Ltd.) consists of 48 electrodes attached to two piezoelectric ceramic discs which are then glued to a thin, dielectric coated substrate. The wave front sensor is a Phasics SID4 four-wave lateral shearing interferometer operating with 160x120 measurement points. The plane of the deformable mirror is imaged to the wave front sensor so as to maintain a linear relationship between applied mirror voltages and measured wave front distortion. When this is the case, measuring the phase response of a voltage applied to each individual electrode on the deformable mirror provides a basis onto which an arbitrary wave front can be decomposed. This

calibration procedure yields a transfer matrix,  $M_{mn}$ , such that the wave front distortion  $\Phi_m$  is related to the vector of deformable mirror voltages,  $V_n$ , by  $\Phi_m = M_{mn}V_n$ . Since there are generally many more measurement points than mirror electrodes,  $M_{mn}$  is not a square matrix. However, a pseudo-inverse of the transfer matrix,  $M_{nm}^{-1}$ , can be found via singular value decomposition such that the required mirror voltages can be found from the desired phase front,  $\Phi_{aim}$ , via  $M_{nm}^{-1}\Phi_{aim} = V_{mirror}$ . The loop is closed by measuring a distorted wave front, computing the phase difference between the measured phase and a flat or reference phase, then computing and applying the required mirror voltages to achieve the desired phase profile in the measurement plane. This process is iterated until it converges to the desired wave front profile.

In practice, the laser wave front is measured in two places to correct for the full optical path. First, the wave front sensor is placed in the diverging beam after the laser focus. A loop is closed, converging to a perfect spherical wave front with a beam divergence corresponding to the focusing geometry. The convergence to a perfect spherical wave front should give an ideal wave front near the focus, and a set of reference voltages are saved. Next, for daily operation the SID4 is placed in a secondary measurement arm looking at a small portion of the laser split from the main beam. The deformable mirror voltages corresponding to the perfect spherical wave front near the focus are applied and a reference interferogram is obtained in the measurement arm. For day to day operation the loop is then closed to the reference

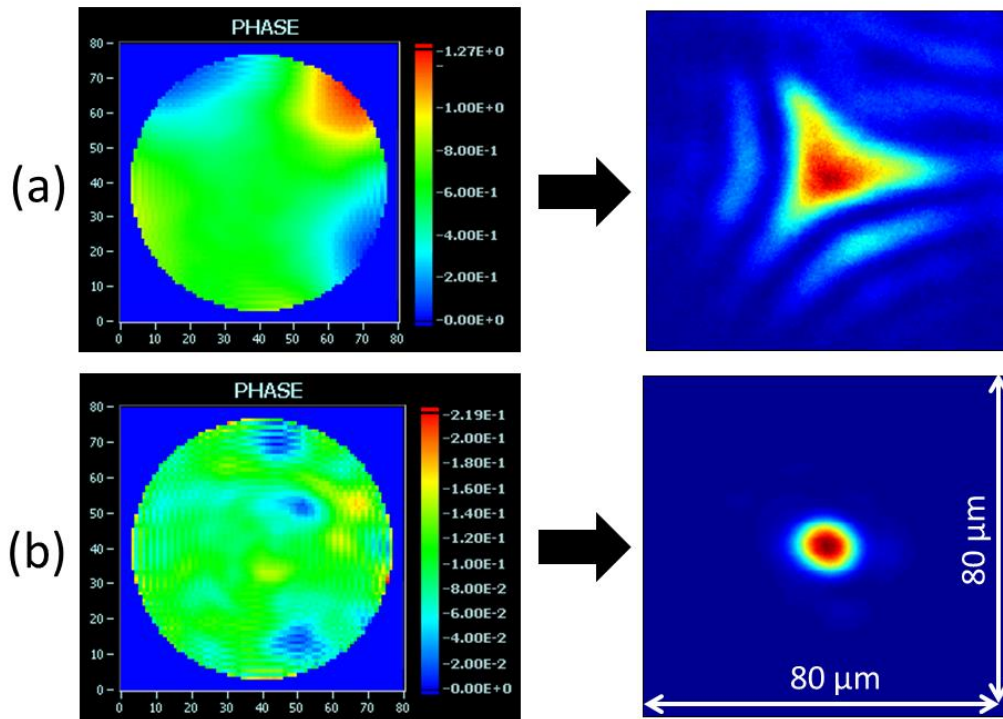


**Figure 2.12.** Measured laser wave front and focal spot before (a) and after (b) convergence of the adaptive optics loop. The phase measurements are in units of waves with  $\lambda = 800nm$ . The wave front curvature and tilts have been removed for clarity. The spatial scale is the same in both focal spot images though the color scales are individually normalized.

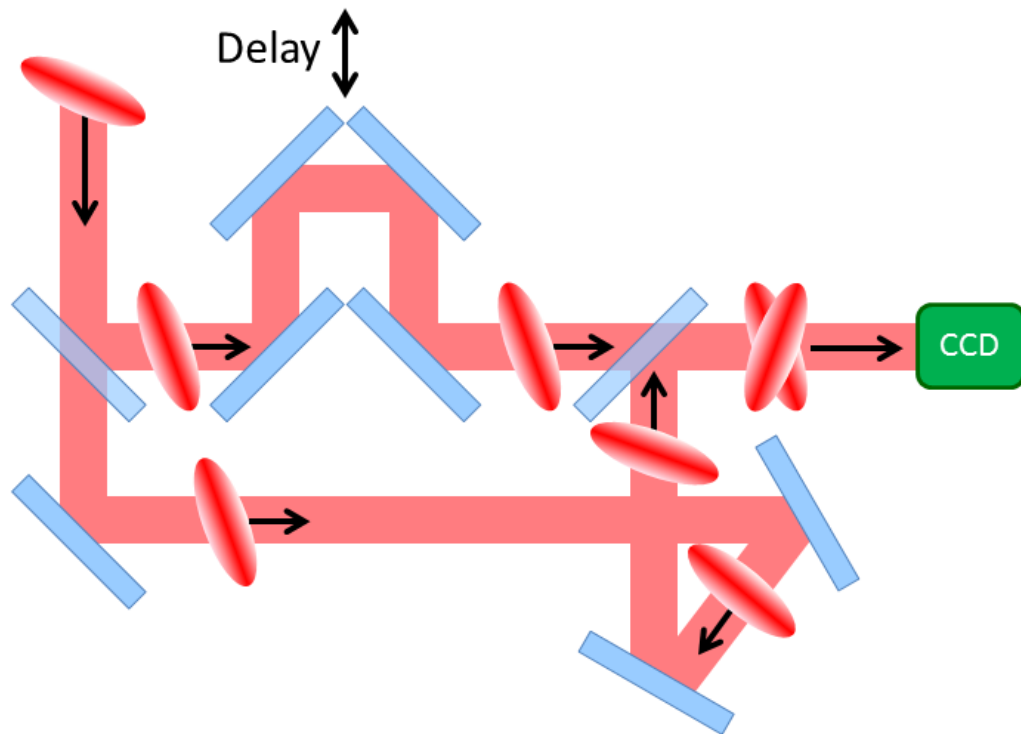
phase front. The use of the reference interferogram effectively removes sensitivity to aberrations in the reference arm so long as they remain constant and allows for wave front correction downstream of the wave front measurement.

Figure 2.12 shows two pairs of phase fronts and corresponding laser focal spots before and after correction by the adaptive optics loop. The beam is focused using a poor optical quality f/9.5 off axis parabolic mirror, which has a surface accuracy worse than one wave peak to valley. The loop is able to correct the wave front error yielding a dramatic enhancement of the peak intensity at the focal spot. The beam Strehl ratio at the focus is 0.12 without correction and improves to 0.97 after convergence of the adaptive optics loop.

## ***2.6 Measurement of spatiotemporal effects***

A final class of measurement required to achieve peak energy density on target in an ultrashort laser experiment is the characterization and mitigation of spatiotemporal effects [123–126]. The main spatiotemporal aberrations present in CPA laser systems are angular chirp and transverse spatial chirp [124,126]. Angular spatial chirp occurs when the angle of the wave vector varies slightly as a function of frequency in the pulse. This leads to a tilt of the plane of peak laser intensity with respect to the beam propagation direction. A beam focused with angular spatial chirp will have a longer pulse duration near the beam waist, potentially causing a substantial reduction in the peak intensity [124,126]. Transverse spatial chirp occurs when the pulse's component frequencies travel in the same direction but are spatially separated across the beam diameter. This causes incomplete overlap of the beam frequencies in the focus, and therefore short pulse duration and high intensity exist in only a narrow region about the beam waist. Transverse spatial chirp has been proposed as a controlled way of avoiding nonlinear pulse propagation for laser surgery and laser machining applications [127–129].

For large beam diameters and short pulse durations (wide spectra), relevant levels of angular and transverse spatial chirp can be difficult to detect. In particular, angular chirp is known to arise in CPA systems from slight misalignments of the compressor diffraction gratings. A simple system proposed for the detection of angular chirp is the inverted field autocorrelator (IFA) [124]. The IFA is a simple Mach-Zehnder or Michelson interferometer in which one arm has an extra reflection which inverts the beam along one transverse dimension. A schematic representation



**Figure 2.13.** Schematic drawing of the inverted field autocorrelator (IFA). A pulse with angular spatial chirp is sent through a modified Mach-Zehnder interferometer and interfered with a slight tilt in the direction perpendicular to the angular spatial chirp. Interference fringes will be visible on the CCD only in the region where the pulses overlap within a coherence length.

of the IFA is shown in Fig. 2.13. The two arms of the IFA are interfered with a slight tilt in the direction perpendicular to the dimension with suspected pulse front tilt. If a beam passed through an IFA has pulse front tilt spanning a distance greater than approximately the coherence length of the pulse, interference fringes will not be observed across the full beam. Figure 2.14(a) shows an IFA trace of the amplified beam with  $0.5 \mu\text{rad}/\text{nm}$  angular chirp, and figure 2.14(c) shows the IFA trace after a 4 arcminute correction to the rotation of the second compressor grating. The rotation of the compressor grating improves the parallelism of the gratings within the compressor and eliminates the angular chirp. The angular chirp also causes ellipticity in the focal spot of the focused beam due to the difference in wave vectors across the diameter of

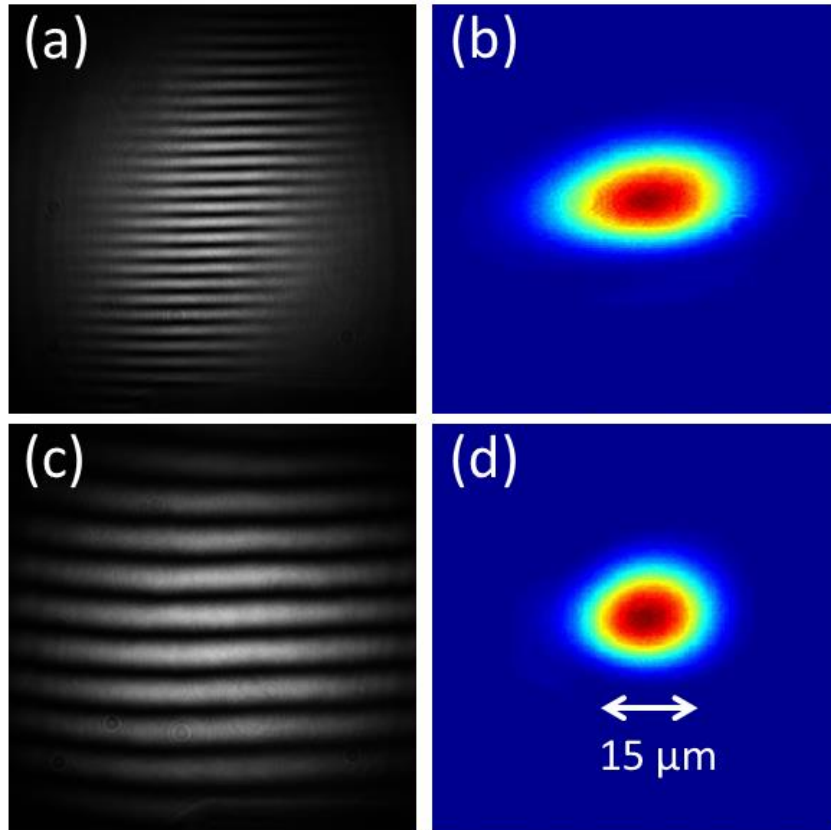


**Figure 2.14.** Inverted field autocorrelation traces before (a) and after (c) correction of a  $0.5 \mu\text{rad}/\text{nm}$  angular chirp on a 39 fs pulse. The focal spot before (b) the correction is elliptical and becomes much more symmetric after improvement of the grating parallelism (d).

the focusing optic. Figure 2.14(b) shows the elliptical focal spot of a beam with angular chirp, and Fig. 2.14(d) shows the focal spot after correction of the grating parallelism.

## ***2.7 Modelocked Nd:YAG Laser System***

The output of the 25 TW laser system was synchronized with the output of a home built 140 ps, 800 mJ Nd:YAG laser system operating at 1064 nm with a 10 Hz repetition rate. The 38 MHz pulse train from the Nd:YAG oscillator (Time-Bandwidth Products GE-100) was synchronized to the 76 MHz Micra pulse train

using a commercial synchronization system (Coherent Synchrolock). The Synchrolock used a feedback loop monitoring the two oscillator pulse trains and adjusted motorized stages within the Micra cavity to match the frequency of the Micra pulse train to twice the frequency of the GE-100 pulse train. The phase difference between the pulse trains was also controllable, so that amplified pulses from the two lasers could be timed to reliably arrive at a target synchronized to within  $< 10$  ps. The Nd:YAG pulse was used as the channel forming pulse in the high intensity guiding experiments presented in Chapters 3 and 4, requiring synchronization of the Nd:YAG and Ti:Sapphire laser systems on a  $\sim 10$  ps time scale for stable shot-to-shot guiding.

The modelocked oscillator for the Nd:YAG system outputs  $\sim 700$  mW in a 38 MHz train of 140 ps pulses. The repetition rate of the oscillator output is reduced to 10 Hz by a Pockels cell and polarizing beam splitter combination and injected into a regenerative amplifier (RGA). The RGA is a self-filtering unstable resonator design and outputs  $\sim 10$  mJ pulses at 10 Hz [130]. The second amplification stage in the Nd:YAG system is a two pass ring amplifier which boosts the pulse energy to  $\sim 100$  mJ. A TFP-waveplate combination after the ring amplifier allows control of the total laser energy output. Following the TFP, the beam is sent through a vacuum spatial filter to eliminate strong diffraction rings caused by overfilling the ring amplifier rod. The diffraction rings must be removed by the vacuum spatial filter in order to prevent self-focusing and damage in the final, single-pass amplifier which boosts the pulse energy from 100 to 800 mJ. The details of the Nd:YAG laser design and operating principles can be found in previous work [131].



## Chapter 3: Optical guiding at relativistic intensities in cluster-based plasma channels

### ***3.1 Introduction to plasma channel guiding***

Diffraction of focused pulses is a serious practical limitation to many applications of high intensity laser-matter interactions which require long interaction lengths at high intensity [5]. Such applications include laser wakefield acceleration of electrons [5,17] and the generation of coherent radiation in the x-ray [19], extreme ultraviolet [132–134], and THz range [135]. As outlined in Chapter 2, diffraction of a focused laser pulse in vacuum limits the region of peak intensity to scale lengths on the order of a Rayleigh length,  $z_R = \pi w_0^2 / \lambda$ , where  $w_0$  is the transverse  $1/e^2$  focal spot size and  $\lambda$  is the laser wavelength. Without any sort of optical guiding this implies that longer interaction lengths (larger  $z_R$ ) require larger spot sizes and therefore higher energy pulses to maintain the same peak intensity. This quickly becomes a practical limitation when relativistic intensities are desired over many centimeters.

The study of electromagnetic waves propagating in hollow conducting ducts, or waveguides, was first studied by Lord Rayleigh over a century ago [136], and the same basic principle of light confinement through structured index profiles has become an integral part of modern transport of electromagnetic radiation. For example, the graded or step index fiber optic cable is able to transport light up to many kilometer distances with sub-millimeter spot sizes. Optical waveguides offer one solution to the practical issue of maintaining ultrahigh peak intensities over long

distances. The peak intensity of a multi-millijoule, focused femtosecond laser pulse, though, is well beyond the damage threshold of a standard material fiber. Indeed, material damage in solids sets in at intensities  $\sim 10^{12}$  W/cm<sup>2</sup> while focused femtosecond lasers can reach intensities well above  $10^{18}$  W/cm<sup>2</sup>. At these relativistic intensities, only plasma is immune to conventional material damage, so experimental and theoretical work has been undertaken to demonstrate and understand guiding of femtosecond laser pulses in plasmas.

### 3.1.1 Self guiding and relativistic self-focusing

Plasma nonlinearities such as ponderomotive charge displacement and relativistic corrections to the plasma refractive index can affect laser pulse propagation at high intensity. When a relativistic intensity pulse propagates through an initially uniform plasma, the plasma frequency is modified due to the mass increase that occurs near the peak velocity of the driven electrons as well as the density perturbation caused by the laser ponderomotive force (i.e. the plasma wave) so that

$$\omega_p^2(r) = \frac{4\pi N(r)e^2}{\gamma(r)m_e} = \frac{\omega_{p,0}^2 N(r)}{\gamma(r) N_0}$$

where  $N_0$  is the ambient plasma electron density,  $e$  is the elementary charge,  $\gamma(r) = \sqrt{1 + \frac{a(r)^2}{2}}$  is the Lorentz factor assuming a linearly polarized laser,  $a(r)$  is the pulse normalized vector potential which is a function of the radial coordinate  $r$ ,  $m_e$  is the electron rest mass, and  $\omega_{p,0}$  is the nonrelativistic plasma frequency [51,137]. The plasma refractive index in the limits  $a_0 \ll 1$  and  $\delta N(r) = N(r) - N_0 \ll N_0$  is then

$$\eta(r) = \sqrt{1 - \frac{\omega_{p,0}^2}{\gamma(r)\omega^2} \frac{N(r)}{N_0}} \approx 1 - \frac{\omega_p^2}{2\omega^2} \left( 1 - \frac{a(r)^2}{4} + \frac{\delta N(r)}{N_0} \right)$$

where  $\omega$  is the laser frequency and it is assumed that the plasma is sufficiently underdense ( $\omega_p/\omega \ll 1$ ). The relativistic mass shift leads to a graded index profile with a maximum at the most intense part of the usually centrally peaked intensity profile. Like Kerr self-focusing in a neutral gas, a critical power for relativistic self-focusing can be derived as

$$P_{cr} = \frac{2ce^2}{r_e^2} \frac{\omega_p^2}{\omega^2} \approx 17 \frac{\omega_p^2}{\omega^2} = 17 \frac{N_{cr}}{N_e} GW$$

provided the pulse duration is much longer than the plasma period [46,52]. At powers above  $P_{cr}$ , relativistic self-focusing in the plasma proceeds until ponderomotive charge displacement reduces the electron density inside the regions of high intensity [53]. The self-focused pulse can then be trapped and guided in the driven high amplitude plasma wave, a process sometimes called ponderomotive channeling or ponderomotive charge displacement self-guiding.

Experimentally, relativistic self-focusing and ponderomotive channeling have been demonstrated by many groups in gas jets and static gas cells for distances up to a few tens of Rayleigh lengths [28,30,138,139]. Provided the laser power satisfies  $P > P_{cr}$ , ponderomotive channeling is arguably the simplest method for maintaining a relativistic interaction over many Rayleigh lengths as the confining index profile is automatic assuming an initial intensity profile peaked on axis. However, self-focusing at low densities, required for  $\sim$  GeV wakefield accelerators, requires increasingly high powers because  $P_{cr} \propto N_e^{-1}$ .

Further, Sprangle et al. showed that for pulses shorter than a plasma period relativistic self-focusing is much less effective because the ponderomotive charge displacement and relativistic contributions to the refractive index tend to cancel [46,53]. Considering the 1D longitudinal force balance equation between the laser ponderomotive force,  $F_p = -\frac{1}{4}mc^2\nabla a_0^2$  (Eqn. (1.4) in the limit  $a \ll 1$ ) and the space charge force due to the plasma wave yields

$$\nabla \cdot F_p = -\frac{1}{4}mc^2\nabla^2 a_0^2 = \nabla \cdot (-eE) = 4\pi e^2(N - N_0).$$

Rearranging this and using the (non-relativistic) formula for  $\omega_p$  gives

$$\frac{1}{4}\nabla^2 a_0^2 \approx \frac{1}{4}\frac{\partial^2}{\partial z^2} a_0^2 = k_p^2 \frac{\delta N}{N_0}$$

where  $k_p = \omega_p/c$ . If  $\frac{\partial^2}{\partial z^2} a_0^2 \sim k_p^2 a_0^2$ , which is true for pulses with longitudinal extent on the order of the plasma wavelength, then  $a^2/4 \sim \delta N/N_0$  and the self focusing and ponderomotive displacement terms in the refractive index tend to cancel. Therefore, relativistic self-focusing is less effective for wakefield accelerators operating in the driven or resonant regime.

### 3.1.2 Optical guiding in pre-formed plasma waveguides

Guiding high intensity pulses can also be achieved through the use of pre-formed plasma waveguides [60]. As an example, consider a plasma with a parabolic density profile given by  $N(r) = N_0 + \Delta N r^2/w_{ch}^2$  where  $\Delta N = N(w_{ch}) - N(0) \geq \frac{1}{\pi r_e w_{ch}^2}$  is the difference between the on axis density and the density at a radius  $w_{ch}$  equal to the radius of the lowest order guided mode, and  $r_e$  is the classical electron radius. In this case, the refractive index

$$\eta(r)^2 = 1 - \frac{N(r)}{N_{cr}} = 1 - \frac{N_0}{N_{cr}} \left( 1 + \frac{\Delta N}{N_0} \frac{r^2}{w_{ch}^2} \right) \quad (3.1)$$

is peaked on axis. In the frequency domain the wave equation for an electromagnetic wave,  $\tilde{E}(\omega)$ , propagating through the plasma is

$$\left( \nabla^2 + \frac{\omega^2}{c^2} \eta(r)^2 \right) \tilde{E} = \nabla \left( -\frac{1}{\eta(r)^2} \tilde{E} \cdot \nabla \eta(r)^2 \right). \quad (3.2)$$

The right hand side of equation (3.2) can be neglected if  $\Delta E/E \ll \Delta(\eta^2)/\eta^2$  over the transverse size of the plasma channel [61]. In this limit the solutions to the wave equation are transversely polarized, or TEM, modes. For typical guided modes the field is well contained by the plasma waveguide so,  $|\Delta E/E| \sim 1$ , while the typical maximum change in the refractive index over the same distance is  $|\Delta\eta/\eta| \sim 10^{-2}$  [61]. For higher order modes or spot sizes approaching the laser wavelength (i.e. non-paraxial beams), the polarization term cannot be neglected. Neglecting the polarization term and taking the ansatz solution to equation (3.2) of a wave propagating in the  $+z$  direction,  $E(x, y, z, t) = u(x, y)e^{i(\beta z - \omega t)}$ , the wave equation reduces to

$$\left( \nabla_{\perp}^2 + \frac{\omega^2 \eta(r)^2}{c^2} - \beta^2 \right) u(x, y) = 0.$$

Substituting in equation (3.1) gives

$$\left( \nabla_{\perp}^2 + k_0^2 \left( 1 - \frac{N_0}{N_{cr}} - \frac{\Delta N}{N_{cr}} \frac{r^2}{w_{ch}^2} \right) - \beta^2 \right) u(x, y) = 0.$$

Introducing the propagation wavenumber in the channel

$$\kappa^2 = k_0^2 \left( 1 - \frac{\beta^2}{k_0^2} - \frac{N(r)}{N_{cr}} \right) \quad (3.3)$$

the wave equation reduces to

$$(\nabla_{\perp}^2 + \kappa^2)u(x, y) = 0. \quad (3.4)$$

This admits strictly bound modes if  $\kappa^2$  is strictly negative beyond some radius and leaky modes if  $\kappa^2 < 0$  out to some radius after which  $\kappa^2 > 0$  [61]. For the parabolic index case, there can only be bound modes since  $n(r)^2 \rightarrow -\infty$  as  $r \rightarrow \infty$ . This is, of course, unphysical but can be used to good approximation if the plasma waveguide is much larger than the bound mode size. For the specific case of the parabolic index profile, an analytical solution to equations (3.3) and (3.4) can be found, and the transverse modes are Laguerre-Gaussian polynomials

$$u(r, \phi) = a_{pm} e^{-\frac{r^2}{w_{ch}^2}} \left( \frac{2r^2}{w_{ch}^2} \right) L_p^m \left( \frac{2r^2}{w_{ch}^2} \right) e^{im\phi}$$

with propagation wavenumber

$$\beta_{pm}^2 = k^2 - 4\pi r_e N_{e0} - \left( \frac{4}{w_{ch}^2} \right) (2p + m + 1).$$

At high intensities, the effects of relativistic self-focusing and plasma wave generation must also be taken into account so that the index profile is given by

$$\eta(r) = 1 - \frac{\omega_{p0}^2}{2\omega^2} \left( 1 + \frac{\Delta N}{N_0} \frac{r^2}{w_{ch}^2} - \frac{a(r)^2}{4} + \frac{\delta N(r)}{N_0} \right).$$

Properly matched guiding, where the laser spot size remains constant over the full interaction length, taking into account all of these effects is complicated, but can be achieved to some extent by tailoring the pre-formed plasma profile to compensate nonlinear index modifications at high intensities [29,140].

Optical guiding in pre-formed plasma channels was first demonstrated through the hydrodynamic expansion of a plasma formed by focusing an intense pulse with an axicon lens into a high Z backfill gas [60]. The axicon focused  $\sim 100$  ps pulse

avalanche ionizes the backfill gas then heats the resulting plasma. The plasma expands at the ion sound speed and a shock wall forms, creating a nearly parabolic density profile out to the shock radius. Plasma waveguides formed in backfill gas suffer from poor coupling caused by ionization of the backfill by the high intensity pulse as it is injected into the waveguide [141,142]. Gas and cluster jet sources have been developed to avoid this drawback and will be described in the next section. The “ignitor-heater” method for generating plasma waveguides through hydrodynamic expansion in lower  $Z$  gases was demonstrated by separating the ionization and heating steps [143]. A femtosecond pulse ionizes the low  $Z$  gas and the resulting plasma is heated by a secondary  $\sim 100$  ps pulse. The subsequent expansion again creates a nearly parabolic density profile near the plasma axis. The ignitor-heater technique was used to demonstrate optical guiding at relativistic intensities in a hydrogen plasma waveguide for the first time [144].

A second commonly used method for generating pre-formed plasma channels is through electrical discharge in a gas filled capillary [145,146]. Ablation of the capillary walls can create a plasma density profile with a minimum on axis [145], or cooling of the plasma discharge at the capillary walls can create a temperature gradient resulting in a nearly parabolic density profile [146]. Capillary discharge waveguides have the advantage of avoiding additional channel-forming lasers which must be timed to the  $\sim 10$  ps level. Guiding in a capillary-based channel has been demonstrated over 9 cm, producing a current record 4.2 GeV wakefield accelerated electron beam [31]. In contrast, waveguides generated by the hydrodynamic expansion technique are normally limited to lengths of about an inch by the energy

requirements of the channel-forming pulse. However, damage from ablation of the capillary walls leads to a relatively short capillary lifetime, and incompletely ionized impurities from the capillary walls can lead to ionization defocusing of an intense pulse within the channel. Measurement of the plasma transverse and longitudinal density profiles, easily performed using transverse probing techniques in gas jet based waveguides [147], is difficult for discharge-based waveguides because of the enclosed geometry of the capillary [148].

## ***3.2 Plasma waveguides generated in clustered gas targets***

### **3.2.1 Advantages of using cluster based targets**

Three main drawbacks of the hydrodynamic expansion method can be mitigated by the use of clustered gas targets rather than a simple monomer gas jet or backfill [149,150]. First, the use of clusters can improve the laser absorption by as much as a factor of 10, leading to deeper channel formation with lower drive pulse energy [151]. Second, the use of clusters allows channel formation at much lower on axis density. Finally, gas jet and backfill waveguides generally suffer from tapering at the channel entrance and exit caused by non-uniform density gas or laser intensity profiles. In a highly clustered gas target the individual cluster motion is ballistic [152]. Therefore skimmers can be used to create sharp  $\sim 100$   $\mu\text{m}$  entrance and exit ramps to the channel.

Clusters are aggregates of van der Waals bonded atoms or molecules of typical diameter  $\sim 1$ -100 nm which form by condensation during the expansion and subsequent cooling of a high pressure gas ejected into vacuum [153]. In the



experiments described in this chapter, multi-photon ionization on the leading edge of a 140 ps channel forming pulse, described in Chapter 2, creates an initial free electron population within the clusters. These free electrons, under influence of the strong laser field, collisionally ionize other atoms within the cluster leading to avalanche ionization of each individual cluster on a time scale  $< 1$  ps [151,154]. The high density nano-plasmas expand and merge on a  $\sim 1$ -10 ps time scale much shorter than the 140 ps channel forming pulse. Thus, the clusters act to create plasma with a much higher initial free electron population compared to an unclustered gas at the same average density. This plasma is then heated by the bulk of the channel forming pulse and hydrodynamically expands to form a waveguide [149,150].

At low electron densities in an unclustered gas, efficient collisional breakdown requires high gas density,  $N_0$ , due to the initially exponential growth of the electron density  $N_e(t) = N_{e0} \exp(SN_0t)$  where  $N_{e0}$  is the initial free electron density,  $N_0$  is the gas density, and  $SN_0$  is the collisional ionization rate. Waveguide formation in unclustered gases has been limited to minimum densities  $\sim 10^{19} \text{ cm}^{-3}$  by the exponential dependence of  $N_e$  on  $N_0$ . Further, the ionization generally occurs near the peak of the channel forming pulse so that only a fraction of the pulse energy is actually used to heat the plasma. This leads to absorption efficiencies of  $\sim 100$  ps heating pulses of only up to  $\sim 10\%$  in unclustered gas jets. In contrast, the ionization of the cluster jet occurs within each near solid density cluster early in the channel forming pulse, and the full pulse duration is used to heat the plasma, leading to absorption efficiencies up to 35%. A detailed description of long pulse absorption and waveguide formation in clustered gas targets can be found in [149,150].

### 3.2.2 Demonstration of efficient coupling into a cluster based plasma channel

Figure 3.1 shows an experimental setup for creating a plasma waveguide in an elongated cluster target. A  $\sim 140$  ps Nd:YAG pulse is focused with an axicon lens over a 1 cm cluster jet. The channel forming pulse is synchronized with the 25 TW Ti:Sapphire femtosecond laser system to within  $< 10$  ps. The Ti:Sapphire laser pulse is focused through a hole in the axicon onto the end of the  $\sim 100$   $\mu\text{m}$  diameter plasma. Guided mode profiles and energy throughputs are measured by imaging the guided Ti:Sapphire pulse onto a CCD camera. Electron density profiles are measured using

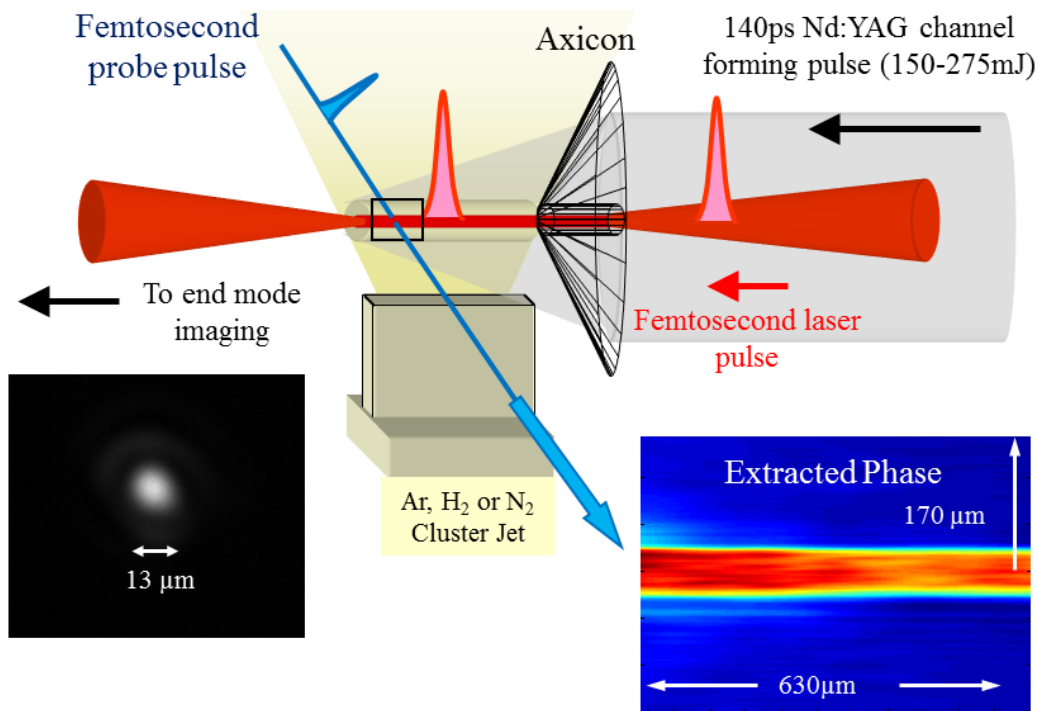


**Figure 3.1.** Experimental setup for making plasma waveguides in cluster jets. A 140 ps channel forming pulse is focused with an axicon lens over the elongated cluster jet. A synchronized femtosecond pulse is focused onto the end of the plasma waveguide through a hole in the axicon. Plasma density is measured using femtosecond transverse interferometry, and guided modes are monitored by relay imaging the exit mode to a CCD camera.

femtosecond transverse interferometry [147]. A portion of the Ti:Sapphire pulse is split from the main beam, frequency doubled, and directed transversely across the plasma. The plasma is imaged through a folded wave front interferometer onto a CCD camera. Phase extraction of the interferograms followed by Abel inversion allows extraction of the radial refractive index and plasma density within the field of view of the CCD assuming cylindrical symmetry [75,147].

Figure 3.2 shows the extracted radial density evolution of a plasma arising from the interaction of a 250 mJ Nd:YAG pulse with a nitrogen cluster jet. The initial density profile 100 ps after arrival of the channel forming pulse is peaked on

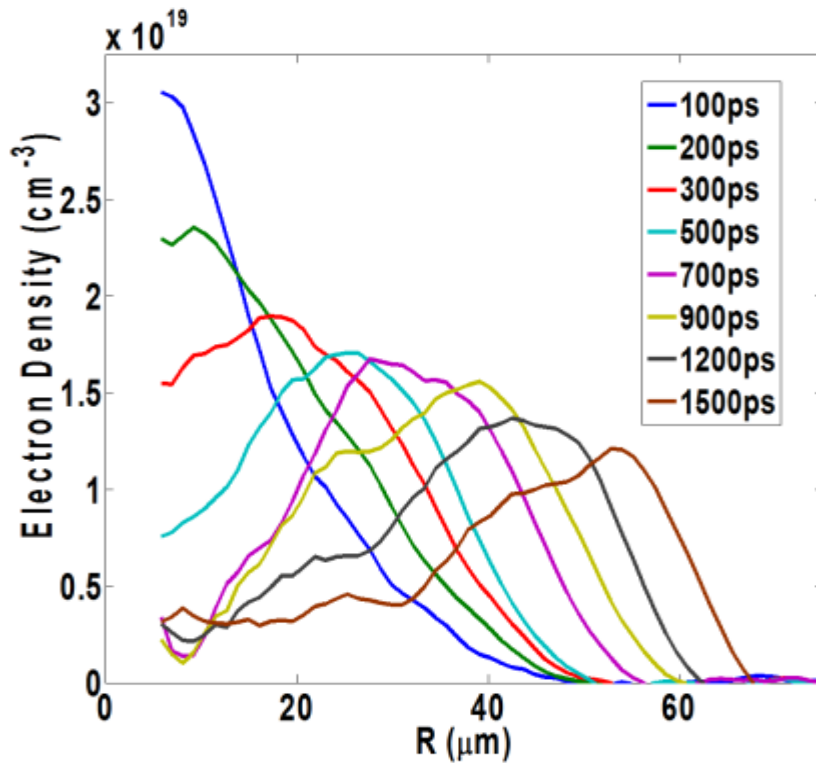


**Figure 3.2.** Temporal evolution of a plasma waveguide formed from an Nd:YAG laser pulse (250 mJ, 140 ps) interacting with a nitrogen cluster jet. The cluster jet is cooled to a gas reservoir temperature of  $-170^{\circ}\text{C}$  and held at 400 psi. The plasma density is initially peaked on axis, but hydrodynamic expansion of the hot plasma creates a density minimum on axis and a radially propagating shock wall.

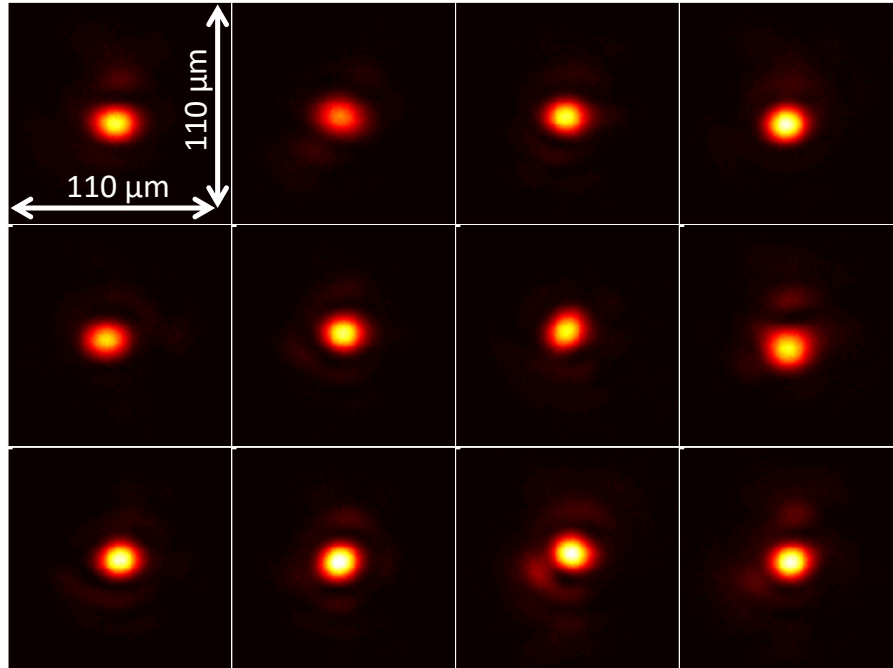


**Figure 3.3.** Consecutive exit modes from a 1 cm long nitrogen plasma waveguide injected with a 50 mJ, 40 fs laser pulse focused to a 13  $\mu\text{m}$  FWHM spot size and delayed by 450 ps with respect to the 250 mJ Nd:YAG channel forming pulse. Average measured energy throughput was 50% with a standard deviation of 11%. Maximum throughput reached 79%.

axis. A deep density depression develops 500 ps later with a refractive index profile capable of guiding an injected laser pulse with 13  $\mu\text{m}$  FWHM spot size. A sequence of twelve consecutive exit modes from the 1 cm long plasma waveguide is shown in Fig. 3.3, showing good mode stability. The injected 50 mJ, 40 fs laser pulse has a FWHM spot size of 13  $\mu\text{m}$  and is guided with a maximum efficiency of 79% and average efficiency of 50%.

Efficient guiding of the injected femtosecond laser pulse first requires efficient coupling into the plasma waveguide. The coupling efficiency of laser pulses injected into waveguides generated in unclustered gas jet and backfill targets was limited by  $\sim 1$  mm scale tapering of the electron density at the waveguide entrance. Ballistic flow of clusters in jets with a high cluster to monomer ratio has been shown



**Figure 3.4.** (a) Cluster jet nozzle with externally attached 100  $\mu\text{m}$  thick sapphire skimmers. (b) 3D printed nozzle with integrated 400  $\mu\text{m}$  thick skimmers. Both are shown in the same custom cryogenic cooling jacket.

to allow sculpting of gas density profiles on  $< 100 \mu\text{m}$  distance scales. Initially used for the purpose of creating modulated plasma waveguides [152,155], the same concept can be used to create sharp density transitions at the entrance and exit of the plasma waveguide. Images of two elongated cluster jet nozzles with thin skimmers at the entrance and exit are shown in Fig. 3.4. In Fig. 3.4(a) the 100  $\mu\text{m}$  thick sapphire skimmers are externally attached to the elongated nozzle. Figure 3.4(b) shows a 3D printed polycarbonate nozzle with integrated  $\sim 400 \mu\text{m}$  thick skimmers.

Figure 3.5 demonstrates the sharp density transition from vacuum to the plasma channel created by the sapphire skimmers. The phase shift imparted on a probe beam by the entrance of a plasma waveguide formed in a nitrogen cluster jet is shown in Fig. 3.5(a). The waveguide entrance exhibits a density ramp of approximately 250  $\mu\text{m}$ , significantly shorter than the  $>1 \text{ mm}$  density gradients associated with unclustered jets. Figure 3.5(b) and 3.5(c) show the same channel  $\sim 1 \text{ ps}$  after passage of a 0.5TW and 2 TW pulse, respectively, along with associated mode profiles at the exit of the 1 cm long waveguide. Though the channel entrance is sharp, there is still a small amount of unclustered, initially unionized gas at the

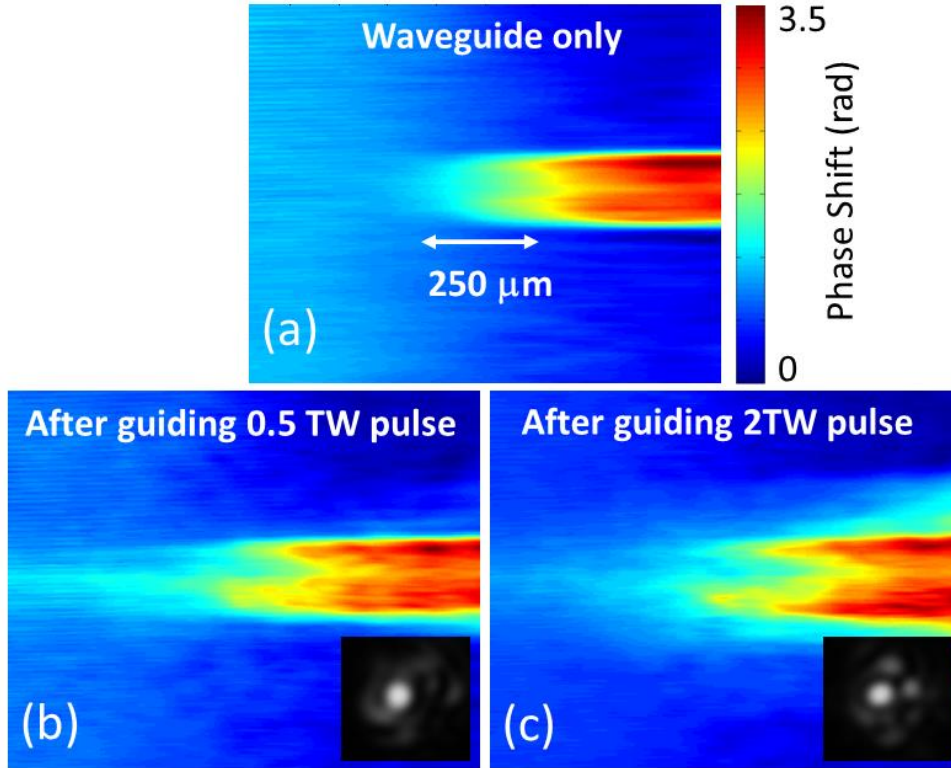


**Figure 3.5.** Extracted phase shift profiles of a nitrogen plasma waveguide before and  $\sim 1$  ps after guiding a femtosecond pulse. The waveguide alone (a) has a  $250 \mu\text{m}$  density ramp. Injection of a 0.5 TW pulse (b) and a 2 TW pulse (c) show the presence of a small amount of residual monomer gas at the entrance to the plasma waveguide. The associated exit mode profiles still show a bright Gaussian spot on axis. The color scale is the same on all three phase images.

channel entrance. For this particular channel Abel inversion of the phase profile in Fig 3.5(c) yields a plasma density in front of the waveguide of  $2 \times 10^{18} \text{ cm}^{-3}$ . This density is clamped above approximately 1 TW ( $\sim 10^{17} \text{ W/cm}^2$ ) in the injected pulse, consistent with ionization of the nitrogen monomers up to  $\text{N}^{5+}$ .

### 3.2.3 Measurement of nearly pure $\text{N}^{5+}$ plasma waveguides

Collisional ionization within clusters has been shown to lead to higher ionization states than can be achieved through field ionization alone. Further, the ionization level tends to halt at closed shell ion configurations where there is a

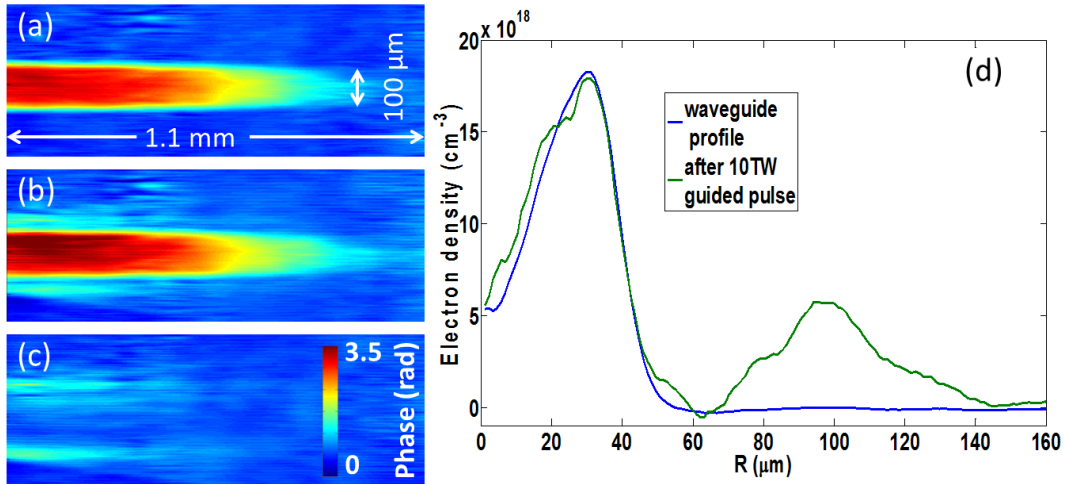


**Figure 3.6.** Phase shift profiles of the exit of a nitrogen plasma waveguide before (a) and  $\sim 1$  ps after (b) guiding a 0.4 TW laser pulse. The difference between the two profiles (c) reveals additional ionization only outside the waveguide. Abel inverted density profiles before and after guiding a 10 TW pulse (d) also show additional ionization only outside the waveguide.

significant jump in ionization potential, for example He-like nitrogen or Ne-like argon [156,157]. This can be important for channel guiding experiments where ionization induced defocusing is meant to be avoided or in laser plasma accelerator experiments where the ionization injection scheme is employed [75].

The He-like ionization state of the nitrogen plasma waveguide was verified by guiding a 15 mJ, 40 fs (0.4 TW) Ti:sapphire laser pulse. The guide exit mode peak intensity was  $10^{17} \text{ W/cm}^2$ , containing up to 80% of the injected pulse energy. Considering that the barrier suppression ionization threshold of Li-like  $\text{N}^{4+}$  (ionization potential 98 eV) ions is  $\sim 10^{16} \text{ W/cm}^2$ , any Li-like nitrogen ions in the channel would be ionized by the guided pulse, resulting in an increase in electron density easily detectable by interferometry. Figure 3.6 shows probe phase profiles near the exit of the plasma waveguide, taken before (a) and  $\sim 1$  ps after (b) guiding of the 0.4 TW pulse. Figure 3.6(c) is the difference between (a) and (b) and would reveal any extra ionization by the guided pulse. Further, Fig. 3.6(d) shows an Abel inverted

density profile before and after guiding of a 10 TW pulse. It is seen that the only additional ionization occurs outside the waveguide, where uncoupled laser energy interacts with neutral clusters, verifying that the plasma channel interior is dominated by the  $N^{5+}$  species. As an added check on the ionization state, the measured nitrogen molecule densities were approximately 10 times less than the average plasma densities, indicating 5 times ionization of each nitrogen atom.

### ***3.3 Guiding at relativistic intensities in pure $N^{5+}$ plasma waveguides***

As outlined in section 3.1, the guiding properties of a plasma channel can be significantly modified at relativistic intensities where nonlinear effects such as relativistic self-focusing and wake formation can modify the channel refractive index profile. Up to 12 TW pulses were injected into the  $\sim 1$  cm pure  $N^{5+}$  plasma waveguides shown in Fig. 3.5 and Fig. 3.6, with an on axis plasma density of  $5 \times 10^{18} \text{ cm}^{-3}$  and (non-relativistic) matched spot size of  $13 \mu\text{m}$ . The critical power for relativistic self-focusing at  $\lambda = 800 \text{ nm}$  and  $N_e = 5 \times 10^{18} \text{ cm}^{-3}$  is approximately 6 TW, so we should expect to see an onset of self-focusing at these power levels. Figure 3.7 shows the energy throughput and peak intensity normalized to the intensity of the injected pulse at the exit plane of the channel shown in Fig. 3.6(d) ( $N_0 = 5 \times 10^{18} \text{ cm}^{-3}, w_{ch} = 13 \mu\text{m}$ ) as a function of injected laser power. Example guided mode profiles for three different laser powers are also shown. Each point on Fig. 3.7 is an average over 100 shots. At low powers we see excellent guided throughput with nearly 70% energy throughput in a single Gaussian mode. However, as the intensity is increased to approach  $a_0 = 1$  and  $P = P_{cr}$  the relative



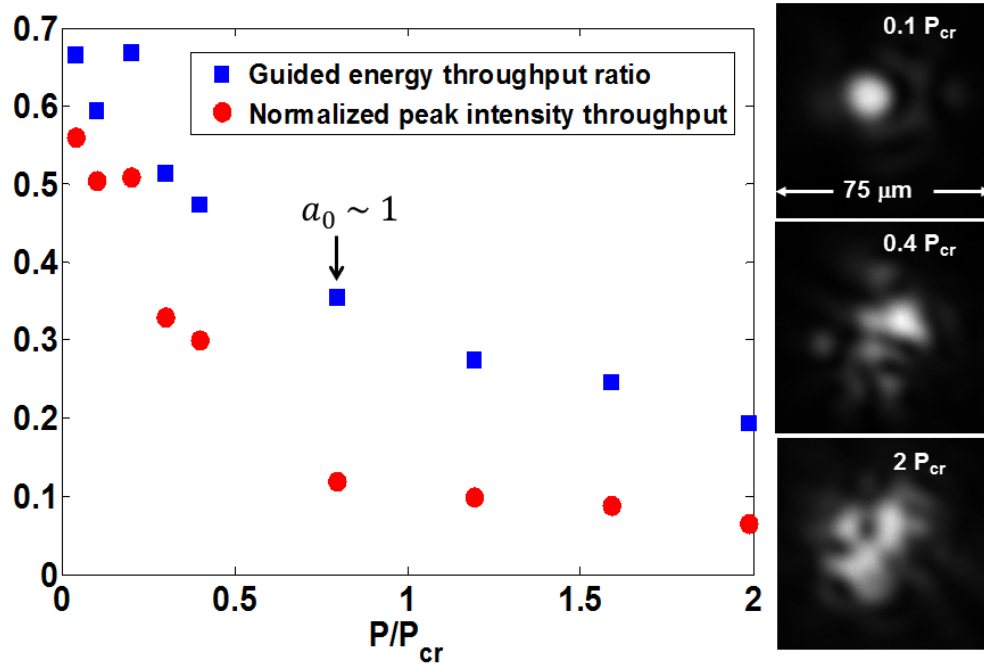


**Figure 3.7.** Energy throughput and normalized intensity at the exit of a 1 cm nitrogen plasma waveguide with on axis density  $5 \times 10^{18} \text{ cm}^{-3}$  as a function of incident laser power. The injected pulse is 40 fs FWHM with a spot size of 13  $\mu\text{m}$ . Exit modes are shown for incident powers 0.1, 0.4, and 2 times the critical power for relativistic self-focusing.

energy throughput decreases drastically, and the transverse profile at the channel exit is highly multi-mode.

Modification of the plasma refractive index by the relativistic laser pulse causes temporal as well as spatial modification of the pulse. Pulse self-compression and self-phase modulation in plasmas have been extensively studied both theoretically and experimentally. The symmetric red and blue shifting of a pulse in the driven wakefield regime has been suggested as a diagnostic for measuring the plasma wave amplitude in laser wakefield accelerators [158]. Measurements of the laser pulse spectrum at the exit of the nitrogen plasma waveguide were made to verify coupling of the pulse to plasma waves. Figure 3.8 shows the injected pulse spectrum and the spectrum at the exit of the plasma waveguide for 2.5 TW and 10 TW injected

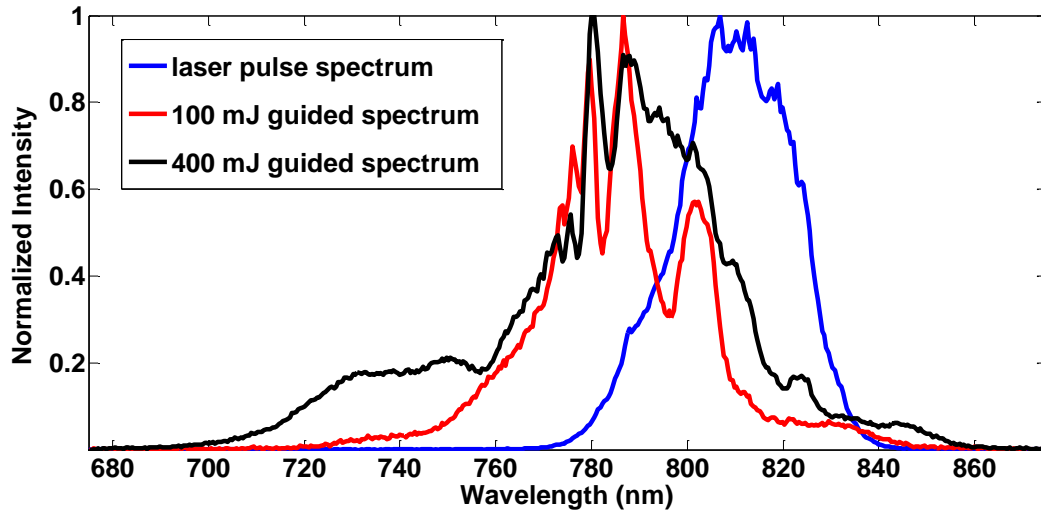


**Figure 3.8.** Laser spectrum before and after it is guided through a 1 cm nitrogen plasma waveguide. Spectral broadening is observed with a redshifted tail indicative of coupling to plasma density perturbations.

powers. The redshifted tail of the pulse at high intensity is indicative of coupling to plasma waves. Blue shifting of the pulse spectrum is likely caused by the ionization of the nitrogen monomers at the entrance to the waveguide.

### ***3.4 Ionization injected wakefield acceleration in an $N^{5+}$ waveguide***

Along with extending the high intensity interaction length, the pure  $N^{5+}$  plasma waveguide provides an abundant source of electrons for injection into a wakefield accelerator. Recently, ionization injection of high Z dopants was proposed and demonstrated to increase electron beam charge and lower the intensity threshold for electron trapping [70–74,159,160]. In this scheme, inner shell electrons of a high Z dopant are ionized near the peak of the drive laser pulse and are trapped in the potential well of the plasma wave. In previous experiments, the high-Z dopant typically does not exceed ~10% of the total density due to laser pulse refraction by

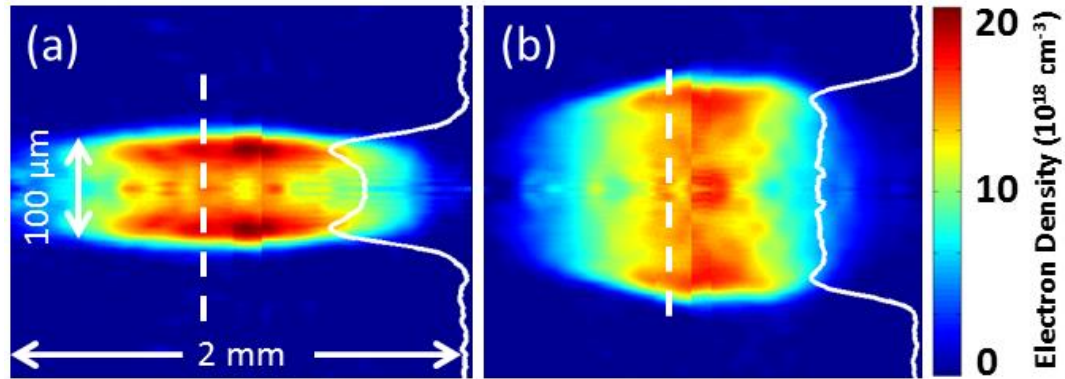


**Figure 3.9.** Abel inverted electron density profiles produced by focusing the Nd:YAG channel forming pulse with an axicon lens (a) and an  $f/20$  spherical lens (b). Lineouts along the dashed white line show a nearly parabolic density profile in the axicon case and a flat density profile in the lens focusing case.

the additional plasma density created on axis [160]. We have demonstrated ionization injection-assisted wakefield acceleration in a pure He-like nitrogen ( $N^{5+}$ ) plasma waveguide [75]. We have shown that use of a preformed plasma channel with a guiding structure stabilizes and narrows the accelerated electron beam compared to the use of a uniform transverse density profile [75].

The effect of the channel on electron beam generation was studied by focusing a Nd:YAG channel-forming pulse into a short,  $\sim 1.5$  mm, nitrogen cluster jet. When the 200 mJ, 140 ps channel-forming pulse was focused with an axicon lens the resulting plasma expanded to form a plasma waveguide as shown in Fig. 3.9(a). When an  $f/20$  lens was used to focus the Nd:YAG laser, a much broader plasma with a flat density profile was created as shown in Fig. 3.9(b). The target length of 1.5 mm is approximately equal to the wakefield accelerator dephasing length associated with the measured on axis plasma density of  $1.4 \times 10^{19} \text{ cm}^{-3}$  [80].

The wakefield drive pulse was an 800 nm, 40 fs Ti:sapphire laser pulse (see Chapter 2) focused by a  $f/9.5$  off-axis parabolic mirror (OAP) and steered by an 800

nm mirror to a 15  $\mu\text{m}$  FWHM spot with a peak normalized vector potential  $a_0 = 1.2$ . The drive pulse was synchronized with the plasma channel-forming pulse with less than 10 ps jitter and injected collinear to the plasma axis at an adjustable delay with respect to channel formation. For experiments with the plasma waveguide, the drive pulse was focused through a hole in the axicon, as shown in Fig. 3.1. For experiments with the flat plasma profile, the 1064 nm pulse was focused by a lens through an 800 nm turning mirror and onto the cluster target.

An image of this waveguide's low intensity exit mode, with spot size FWHM of 14  $\mu\text{m}$ , is shown in Fig. 3.10(b), in agreement with the calculated mode for this index profile. The low intensity exit mode shows guiding over approximately 2.5 Rayleigh lengths. By tuning the gas jet backing pressure, the peak on-axis density for both cases was set to  $1.4 \times 10^{19} \text{ cm}^{-3}$ . Both channels have long density ramps along the laser propagation axis which follow the neutral  $\text{N}_2$  molecule density profile. Particle-in-cell (PIC) simulations presented later show that the density gradient at the end of the channel helps to trap the ionized inner-shell electrons by expanding the plasma bucket, as has been reported by other groups [34].

A 10TW drive laser pulse with a peak intensity of  $3.3 \times 10^{18} \text{ W/cm}^2$  ( $a_0 = 1.2$ ) at the focus was injected into both pre-formed plasma density profiles. Figure 3.10(a) shows optical spectra of the drive pulse after exiting the flat and waveguide profiles. The spectrum from the waveguide shows a significant red wing, consistent with pulse self-phase modulation over the guide length by a large amplitude plasma wave [158], while the spectrum from the flat profile is largely blue-shifted due to significant interaction of the drive pulse with unionized clusters outside the flat plasma profile.

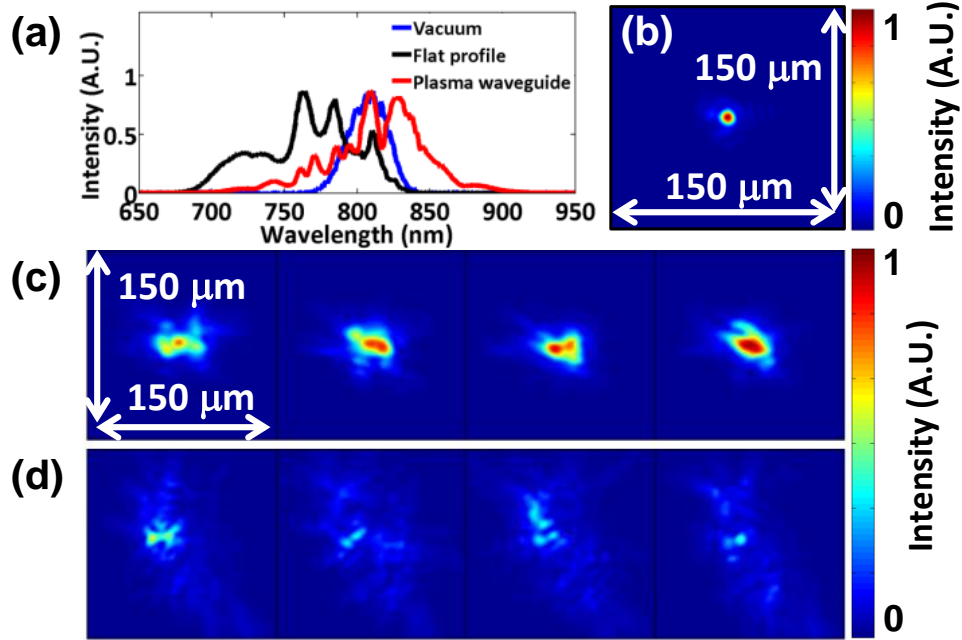


**Figure 3.10.** (a) Optical spectra of the 10 TW pulse before (blue) and after interaction with a flat (black) and guiding (red) electron density profile, each with a peak on axis density of  $1.4 \times 10^{19} \text{ cm}^{-3}$ . A low intensity (0.4 TW) guided mode (b) shows a Gaussian mode with 14  $\mu\text{m}$  FWHM. High power (10 TW) exit modes from the channel profile (c) and flat density profile (d) show improved confinement by the plasma waveguide.

Laser pulse exit mode images from the waveguide (Fig. 3.10(c)) show stable shot-to-shot confinement, although relativistic contributions to the waveguide index profile distort the mode compared to Fig. 3.10(b). By contrast, the beam from the flat profile (Fig. 3.10(d)) is not stable and shows a tight, relativistically self-focused spot that varies shot-to-shot along with significant unfocused energy outside of the flat plasma region. Interaction of the unfocused energy with unionized clusters explains the largely blue-shifted spectrum. This shows that even though the peak laser power satisfies  $P/P_{cr} > 3$  at the channel center, under our conditions the plasma waveguide is more effective than relativistic self-focusing in confining laser pulse energy to the propagation axis. This enables the guided pulse to drive a large amplitude plasma

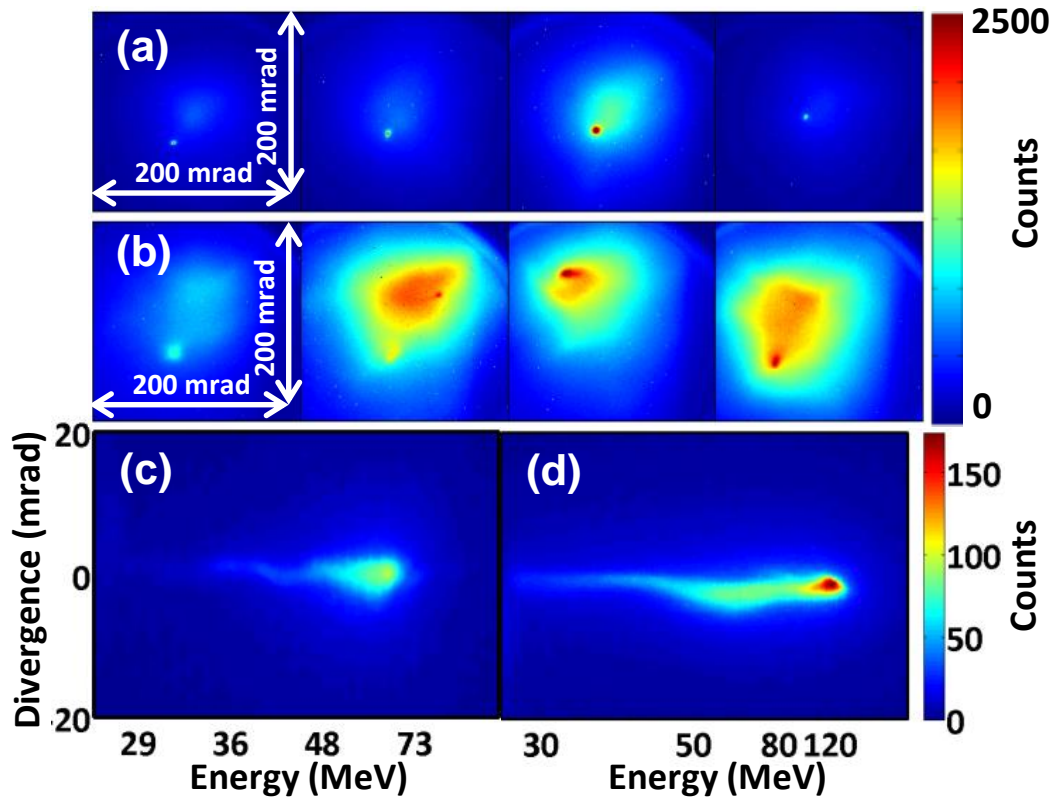


**Figure 3.11.** Electron beam profiles from the  $N^{5+}$  waveguide (a) and the  $N^{5+}$  flat density profile (b). A typical spectrum (c) shows acceleration with a peak at 60 MeV while the highest energy spectrum (d) is peaked near 120 MeV.

wave over a longer distance, resulting in the significant redshift missing in the flat plasma case.

The electron beam transverse profile and charge were measured using a Lanex fluorescing screen and published electron to photon conversion efficiencies [161,162]. The beam energy spectrum was measured using a 0.5 T magnetic spectrometer coupled to the same Lanex fluorescing screen. Figure 3.11 shows electron beam profiles from the waveguide plasma, (a), and from the flat waveguide, (b). The electron beam from the plasma waveguide is both more tightly collimated (2.8 mrad shot-averaged divergence vs. 6.6 mrad from the flat channel)

and more stable (12 mrad standard deviation in beam pointing vs. 42 mrad). The charge in the tightly collimated, energetic electron beams of (a) is estimated to be approximately 5 pC based on prior calibration of the Lanex fluorescence [162] and estimated efficiency of the imaging system.

For the plasma waveguide, we observed a quasi-monoenergetic peak as large as 120 MeV (d), with average peak energy  $\sim 65$  MeV (c), with a low energy tail extending down to 32 MeV. The low energy tail is commonly observed in ionization injection from continuous injection throughout the acceleration process [74,159,160]. For the flat channel, however, the electron energy could not be measured due to unstable beam pointing through the magnetic spectrometer.

To gain insight into the trapping and acceleration processes in the  $N^{5+}$  plasma waveguide 3D particle-in-cell simulations were performed using the code TurboWAVE [163], which includes a tunneling ionization model [164]. In order to assess the contribution of ionization injection from  $N^{5+}$  ions in the waveguide, simulations were performed for (i) a helium-like nitrogen plasma waveguide and (ii) a pre-ionized hydrogen channel with the same electron density profile as (i). A  $\lambda=800$  nm, 40 fs,  $3.3 \times 10^{18}$  W/cm<sup>2</sup> peak intensity pulse, with a 14  $\mu\text{m}$  FWHM beam waist was guided in both the  $N^{5+}$  and  $H^+$  plasma waveguides. Corresponding to the measured waveguide profile of Fig. 3.9(a), each end of the simulated channel had an initial 700 $\mu\text{m}$  linear density ramp with on-axis densities rising from  $8 \times 10^{18}$  cm<sup>-3</sup> to  $1.4 \times 10^{19}$  cm<sup>-3</sup>, with a 100  $\mu\text{m}$  plateau region in the middle. A short 50  $\mu\text{m}$  ramp at either end brought the plasma density to vacuum. The total charge was neutralized by distributing either  $N^{5+}$  or  $H^+$  ions within the channel.

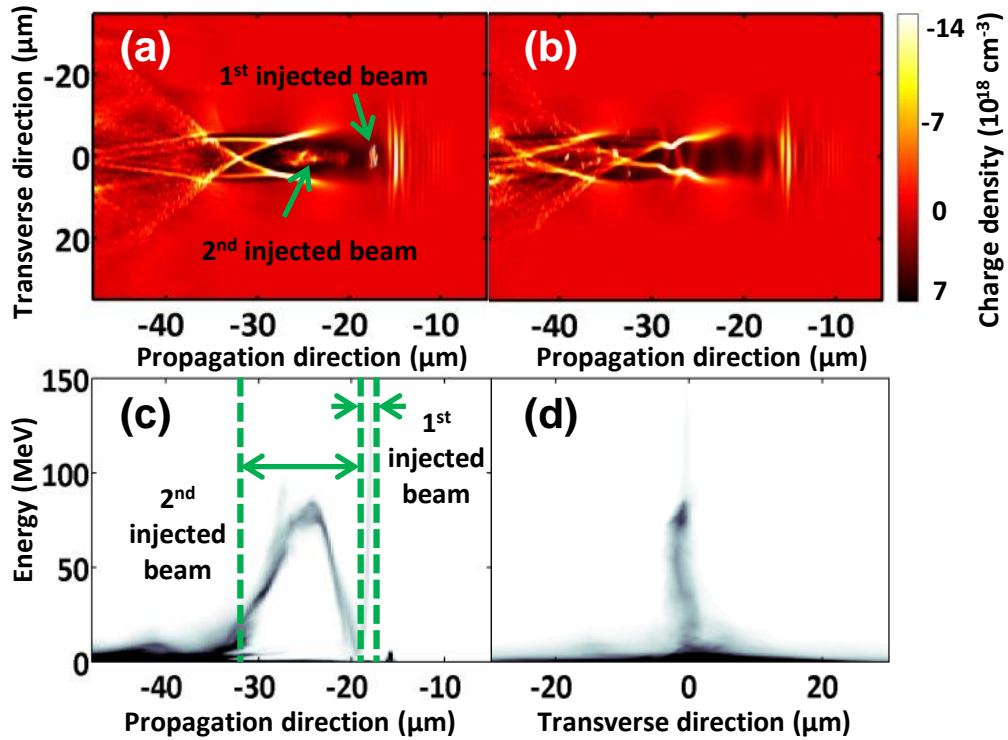


**Figure 3.12.** Charge density plots from Turbowave 2D PIC simulations after 1.4 mm propagation in a He-like nitrogen plasma waveguide (a) and a hydrogen plasma waveguide (b) with the same electron density profile. No beam injection is observed in the hydrogen channel case. The longitudinal (c) and transverse (d) phase space of the electrons ionized from  $N^{5+}$  to  $N^{6+}$  in the waveguide after 1.4 mm propagation show similar beam profile and energy as observed in experiments.

Electron beams similar to those observed experimentally, though with substantially higher charge, were produced from the simulated helium-like nitrogen plasma channel. A mono-energetic peak appears at 80MeV with a long low energy tail, as can be seen in the phase space plots Fig. 3.12(c) and 3.12(d). We can see the trapped electrons inside the bucket in Fig. 3.12(a), which shows a charge density plot near the end of the  $N^{5+}$  channel. In contrast, Fig. 3.12(b) shows that no significant trapping occurs in the hydrogen plasma channel.

Figures 3.12(a) and 3.12(c) also show that two spatially separated beams are trapped. The first beam has a lower charge (14pC) and a broad spectrum extending up



to 150MeV, whereas the second beam contains much more charge (55pC) and the energy distribution has a quasi-monoenergetic peak at 80MeV. From the simulations, we observe that the second beam is trapped at the density down ramp, whereas the first beam is trapped starting from the entrance of the channel. Due to the significant difference in accelerated charge observed between the experiment and simulations, only the down ramp injected electrons are seen in the experimental electron spectra. The density down ramp traps significant charge in a short time by expanding the plasma bucket, giving rise to the quasi-monoenergetic peak. Even with the density down ramp, the plasma wave driven by the laser pulse was not strong enough to self-trap background plasma electrons without the help of ionization injection, and simulations showed that both beams are composed of K-shell electrons ionized near the peak of the drive laser pulse.

## Chapter 4: Guiding of quasi-radially polarized modes in a plasma channel

### ***4.1 Direct acceleration in a plasma slow wave structure***

The vast majority of publications relating to laser driven plasma electron accelerators have focused on the laser wakefield (LWFA) technique described in the introduction to this dissertation. However, as outlined in that chapter, a major impediment to widespread application of these advanced accelerator concepts is the size, cost, and repetition rate of the drive lasers needed to create such an accelerator. Whereas the LWFA concept uses the large electrostatic fields associated with a laser driven nonlinear plasma wave, there have been a number of attempts to use the laser field itself, by far the largest electric field available in the lab, as an accelerating field [15,16,81,165,166]. There are three major impediments to using a laser electric field to accelerate charged particles. First, the laser field is oscillatory, so either the acceleration must be subcycle or the symmetry between the acceleration and deceleration phases must be broken. Second, the laser field is normally transverse to the laser propagation direction. This impediment can be overcome by using the strong longitudinal fields at the focus of a radially polarized pulse [15,167–169]. Acceleration of electron beams by tightly focused radially polarized beams in a background gas has been demonstrated, though at relatively small net energy transfer [15,165]. Finally, for high energy acceleration the high field intensity must be maintained over sufficient distances. This constraint is frequently limited by the

Rayleigh range of the focused beam but can be overcome through the use of guiding structures such as those presented in Chapter 3.

Recently a quasi-phase-matching DLA scheme has been proposed and studied both analytically and through particle-in-cell (PIC) simulations [12,84,85,170]. In this scheme the longitudinal field of a radially polarized femtosecond laser pulse is used as the accelerating field. The radially polarized pulse is injected along with a co-propagating relativistic electron beam into a plasma slow wave guiding structure. The slow wave structure is formed by applying axial density modulations to a plasma waveguide such as those described in Chapter 3.

In the limit that the laser frequency,  $\omega_0$ , is much larger than the plasma frequency,  $\omega_p = \sqrt{4\pi N_e e^2 / m_e}$ , the phase velocity of an electromagnetic wave propagating in an unmodulated plasma channel is given by

$$\frac{v_p}{c} = 1 + \frac{N_{e,0}}{2N_{cr}} + \frac{4}{k_0^2 w_{ch}^2}$$

where  $N_{e,0}$  is the on axis electron density,  $N_{cr}$  is the laser critical density,  $w_{ch}$  is the matched spot size of the waveguide, and  $k_0$  is the laser wavenumber [61]. It is evident that the phase velocity is strictly superluminal and, therefore, cannot be matched to the velocity of a co-propagating relativistic electron. However, in the presence of axial density modulations the phase velocity becomes

$$\frac{v_p}{c} = 1 + \frac{\bar{N}_{e,0}}{2N_{cr}} + \frac{4}{k_0^2 w_{ch}^2} - \frac{mk_{mod}}{k_0}$$

where now  $\bar{N}_{e,0}$  is the longitudinally averaged on axis electron density,  $k_{mod} = 2\pi/d_{mod}$  is the wavenumber associated with the density modulation period  $d_{mod}$ , and  $m$  is an integer [12,84]. The axial density modulations launch axial harmonics of the

pulse which propagate at slower (for  $m>0$ ) or faster (for  $m<0$ ) phase velocity than the fundamental axial mode ( $m=0$ ) through the waveguide. The  $m>0$  waves are called “slow waves” in the RF and microwave literature and, through proper tuning of  $k_{mod}$ , can be made to propagate at or below the speed of light. The slow wave structure breaks the symmetry between accelerating and decelerating phases of the pulse as it interacts with the co-propagating electron beam, allowing a net energy transfer to the electrons over the length of the plasma waveguide. Similar to quasi-phase-matching in nonlinear optics [171,172], the electron periodically gains and loses energy as it propagates, with a net gain in each cycle resulting in a net energy gain over the full propagation path.

A simple scaling law for the energy gain in the quasi-phase-matched DLA process was developed by York *et al.* [12] by considering the maximum energy gain  $\Delta E_{DLA}$  of a highly relativistic test electron accelerated in a modulated channel,

$$\frac{\Delta E_{DLA}}{m_e c^2} \sim 4\delta a_0 \left(\frac{\sigma_z}{w_{ch}}\right) \left(\frac{\lambda_p}{\lambda_0}\right)^2 \left(1 + \frac{2\lambda_p^2}{\pi^2 w_{ch}^2}\right)^{-2} \quad (4.1)$$

where  $\delta$  is the modulation depth of the corrugated plasma waveguide,  $a_0$  is the laser normalized vector potential,  $\sigma_z$  is the longitudinal extent of the laser pulse,  $\lambda_p$  is the plasma wavelength, and  $\lambda_0$  is the laser wavelength [12]. Dephasing in the DLA process occurs when the accelerated electron outruns the laser pulse envelope. The DLA energy gain of equation (4.1) can be compared to that for LWFA,

$$\frac{\Delta E_{LWFA}}{m_e c^2} \sim \frac{a_0^2}{\sqrt{1 + a_0^2/2}} \left(\frac{\lambda_p}{\lambda_0}\right)^2 \left(1 + \frac{2\lambda_p^2}{\pi^2 w_{ch}^2}\right)^{-1} \quad (4.2)$$

as derived by Hubbard et al. in the mildly relativistic regime [77]. For typical experimental parameters  $\lambda_0 = 800 \text{ nm}$ ,  $w_{ch} = 15 \text{ }\mu\text{m}$ ,  $a_0 = 0.25$ ,  $\frac{\sigma_z}{c} = 300 \text{ fs}$  corresponding to a 1.9 TW laser power,  $\bar{N}_{e,0} = 7 \times 10^{18} \text{ cm}^{-3}$ ,  $\delta = 0.9$ , and a modulation period  $d_{mod} = 349 \text{ }\mu\text{m}$ , York *et al.* [12] calculate a peak energy gain of  $\frac{\Delta E_{DLA}}{m_e c^2} \sim 1000$ . This is comparable to the energy gain  $\frac{\Delta E_{LWFA}}{m_e c^2} \sim 750$  calculated in [77] for a wakefield accelerator driven by a 7.16 TW laser in a suitable plasma channel. However, the linear dependence of the DLA energy gain with the laser field provides the strongest advantage of such a scheme. Even with peak powers  $\sim 10 \text{ GW}$  typical of kHz regenerative amplifiers the DLA scheme can yield energy gains  $\frac{\Delta E_{DLA}}{m_e c^2} \sim 50$  whereas highly nonlinear wakefield accelerators are generally unable to operate. This scaling argument shows that DLA is an intriguing technique for applications requiring moderate electron energies and high repetition rates in a compact and affordable package.

## **4.2 Generation of modulated waveguides for DLA**

The first major hurdle for a proof of concept demonstration of DLA was the generation of a suitably micro-structured plasma waveguide to serve as the slow wave structure. This was first accomplished by Layer *et al.* using the hydrodynamic expansion method to form the plasma waveguide using a clustered gas target and an auxiliary  $\sim 100 \text{ ps}$  pulse as outlined in Chapter 3 [173]. The axial modulations were achieved by imaging a diffractive “ring grating” to the axicon as shown in Fig. 4.1(a). Multiple diffraction orders from the ring grating interfering on axis created axial intensity modulations of the channel forming pulse. The axial intensity modulations

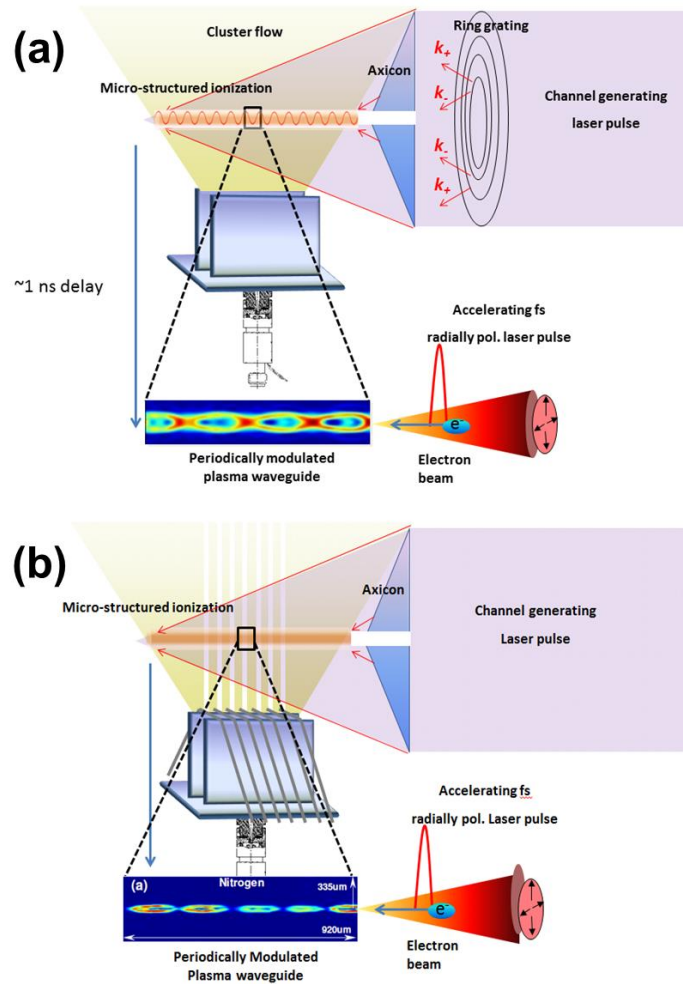


**Figure 4.1.** Experimental setup for creating modulated plasma waveguides using (a) a ring grating to modulate the focused intensity of the channel generating pulse and (b) wire obstructions for creating density modulations by periodically interrupting cluster flow. The general DLA scheme is also presented.

lead to a modulation of the ionization depth along the channel creating the necessary density modulations.

A simpler method, shown in Fig. 4.1(b), has been demonstrated for creating modulated channels in which the elongated cluster target is periodically obstructed using an array of thin wires [152,155,174]. The obstruction method has the advantage of providing large modulation depths, which may enhance the total energy gain in the accelerator [174]. Figure 4.2 shows the time evolution of a modulated

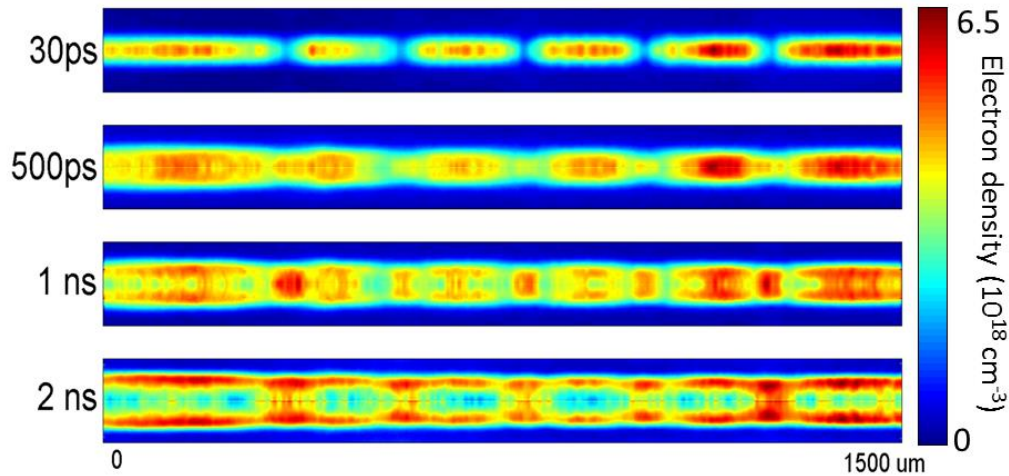


**Figure 4.2.** Abel inverted density profile of wire modulated plasmas as a function of probe delay. After  $\sim 1$  ns delays a density minimum develops on axis providing a suitable density profile for optical guiding. Axial density modulations with a  $220 \mu\text{m}$  period are generated by obstructing the cluster flow with  $25 \mu\text{m}$  diameter tungsten wires.

channel created in a nitrogen cluster jet with a  $200 \mu\text{m}$  period wire array. Using  $25 \mu\text{m}$  diameter tungsten wires, modulation periods as small as  $\sim 70 \mu\text{m}$  were possible without significant loss of density in the unobstructed regions between the wires. These small modulation periods can be important for ramping the quasi-phase-matching period to successfully accelerate lower energy electrons [170]. However, it was found that with such small wire spacings the cluster flow properties become important for maintaining a quality plasma channel [152]. If there is a significant monomer fraction to the supersonic flow past the wire obstructions, then shock waves form which can disassemble the clusters [174]. The effect of shocks is eliminated with increased cluster size accompanied by a reduced monomer component of the flow. When the cluster flow is ballistic (the mean free path for cluster collisions is much larger than the wire diameter) the shockwaves disappear and a clear shadow appears behind the wires. Figure 4.3 demonstrates the effect of

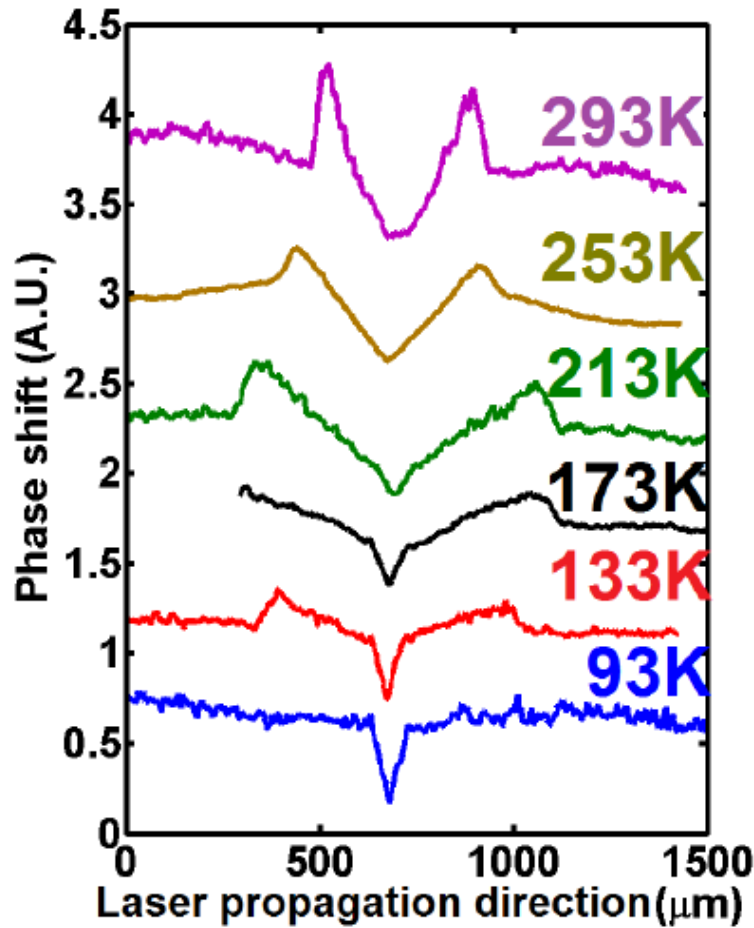


**Figure 4.3.** Lineouts of phase profiles in a plasma generated over a cluster jet obstructed by a single wire as a function of cluster jet reservoir temperature. At high temperatures and low mean cluster sizes shock waves are clearly evident while only a ballistic shadow of the wire appears at low temperatures and large mean cluster sizes.

jet reservoir temperature, and consequently cluster size, on shock formation behind a single wire in a nitrogen cluster jet.

Both the ring grating and wire modulation methods provide static modulation periods, and a new ring grating or wire array must be fabricated for each modulation period. For experimental optimization of the phase matching process a dynamic modulation period which can be controlled on the fly is preferred. This is particularly true in the case of period or density ramping, where the seed electron beam is of too



low an initial velocity to be phase matched at a single period over the entire interaction length [85]. The use of a spatial light modulator to dynamically shape the intensity profile of the channel-forming pulse shows promise in providing dynamic modulation control [175]. This is the subject of ongoing work and could also provide fine control of channel profiles for improved coupling to plasma channels or controllable density dips which have been used as a diagnostic for laser wakefield accelerators [176,177].

### ***4.3 Generation and focusing of quasi-radially polarized beams***

Radially polarized laser beams (RPLBs), proposed as the drive field for the DLA scheme and other direct particle acceleration schemes, have found applications in a variety of fields including optical trapping [178,179], laser machining [180,181], and microscopy [182]. A RPLB is particularly interesting in all of these fields because, when focused with a high numerical aperture lens the (non-paraxial) RPLB can produce a dominant longitudinal field at its focal plane with a transverse extent smaller than the conventional diffraction limit for linearly polarized beams [182]. Due to this field structure, the RPLB has been described as a free space analog to TM modes found in RF and microwave waveguides [183,184]. In the paraxial limit, the fields of the RPLB can be derived by considering an axially polarized vector potential in the Lorentz gauge satisfying the Helmholtz equation [183]. The vector potential has standard Gaussian mode solutions the lowest of which is of the form

$$A_z = \frac{A_0}{k\tilde{q}(z)} \exp \left[ ik \frac{x^2 + y^2}{2\tilde{q}(z)} + ikz \right]$$

where  $\tilde{q}(z) = z - iz_R$  is the complex Gaussian beam parameter and  $k = \omega/c$  is the wavenumber. The electric and magnetic fields can then be calculated from simple relations  $\vec{B} = \nabla \times \vec{A}$  and  $\vec{E} = -\frac{ic}{k} \nabla \times B$  to be

$$B_\theta = \frac{-ikr}{\tilde{q}} A_z$$

$$E_r = cB_\theta$$

$$E_z = -\frac{2c}{\tilde{q}} \left( 1 + \frac{ikr^2}{2\tilde{q}} \right) A_z.$$

Much effort has gone into the calculation of the longitudinal fields of RPLBs in nonparaxial and pulsed (non-monochromatic) limits in which case a significant fraction of the electromagnetic energy can be contained in the longitudinal field [13,182,184,185].

Methods have been demonstrated for generating RPLBs both inside and outside the laser cavity. Due to the complexity of maintaining radial symmetry inside of a laser cavity, which will normally be broken by polarizing or Brewster angle

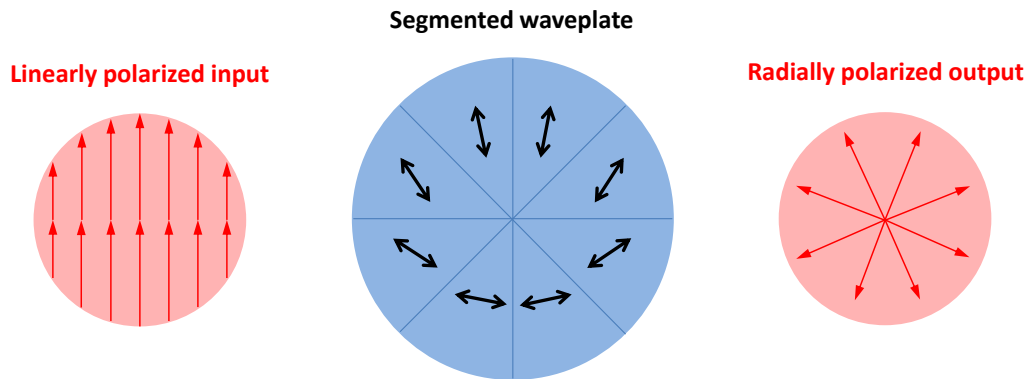


**Figure 4.4.** Concept of a segmented waveplate used for generating approximately radially polarized light. Slices of a  $\lambda/2$  waveplate are arranged with slowly varying orientation of the birefringent crystal's slow axis. This causes a varying rotation of the laser polarization with the azimuthal angle

optics, extra-cavity radial polarizing schemes are of interest for generating a DLA drive pulse. The most commonly used method of generating radial polarization is the segmented waveplate [186,187]. This consists of a standard half wave plate which has been cut into various segments and rearranged such that the slow axis rotates around the optic as shown in Fig. 4.4. A linearly polarized beam passing through the segmented waveplate will experience a difference in polarization rotation around the azimuthal angle following the slow axis of the waveplate giving an approximately radially polarized beam. The degree of radial polarization (and cost of the waveplate) increases with an increasing number of segments. Recently, commercial radial polarizers based on liquid crystal spatial light modulators have become available which can give an excellent approximation to a purely radially polarized beam, but suffer from a relatively low damage threshold [188].

It has been shown that a RPLB can be constructed as a linear combination of linearly polarized Hermite-Gaussian  $TEM_{01}$  and  $TEM_{10}$  modes [90,189]. Therefore, we can consider the lowest order approximation to radial polarization to be a linearly polarized Hermite-Gaussian  $TEM_{01}$  mode. These modes can be produced by passing a linearly polarized beam through an appropriate (reflective or transmissive) step phase plate which applies a  $\pi$  phase shift across two halves of the beam. This was accomplished on our system by placing a 2  $\mu\text{m}$  thick “half-pellicle” in the beam path. The half-pellicle is a standard optical pellicle in which half the film has been cut away with a razor blade. The angle of the pellicle was tuned to create a half wave difference in the optical path length across the beam as shown in Fig. 4.5(a). The measured intensity profile of the resulting beam at the focal plane is shown in Fig.

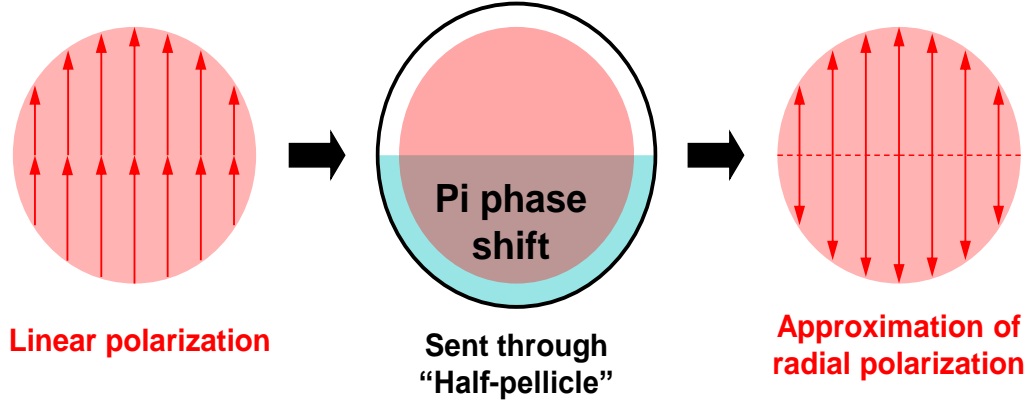


**Figure 4.5.** A pellicle beamsplitter cut in half with a razor blade was used to transform a linearly polarized Gaussian beam into an approximation of a Hermite-Gaussian  $TEM_{01}$  mode. The angle of the pellicle was tuned to apply a  $\pi$  phase shift on one half of the beam with respect to the other.

4.6(a). The focal plane of a pure  $TEM_{01}$  mode is shown in Fig. 4.6(b), and lineouts parallel to the polarization direction are plotted in Fig. 4.6(c). The overlap integral of the half-pellicle mode with a pure Hermite-Gaussian  $TEM_{01}$  mode is

$$\frac{P_{01}}{P_{HP}} = \frac{\int E_{HP} u_{01}^* dA}{\int |E_{HP}|^2 dA} = 0.85$$

where a flat phase profile is assumed so that  $E_{HP} = \sqrt{I_{HP}}$ .

The longitudinal field of a Hermite-Gaussian mode can be approximated in the paraxial limit by considering Gauss's law near the focal plane [81,182]. In the paraxial limit the electric field satisfies the Helmholtz equation

$$\frac{\partial}{\partial z} E = \frac{i}{2k} \nabla_{\perp}^2 E.$$

The Gaussian lowest order mode is given by

$$\mathbf{E}_{00}(x, y, z) = \mathbf{E}_0 \frac{w_0}{w(z)} \exp\left(-\frac{x^2 + y^2}{w(z)^2} + i\left[kz - \eta(z) + \frac{k(x^2 + y^2)}{2R(z)}\right]\right)$$

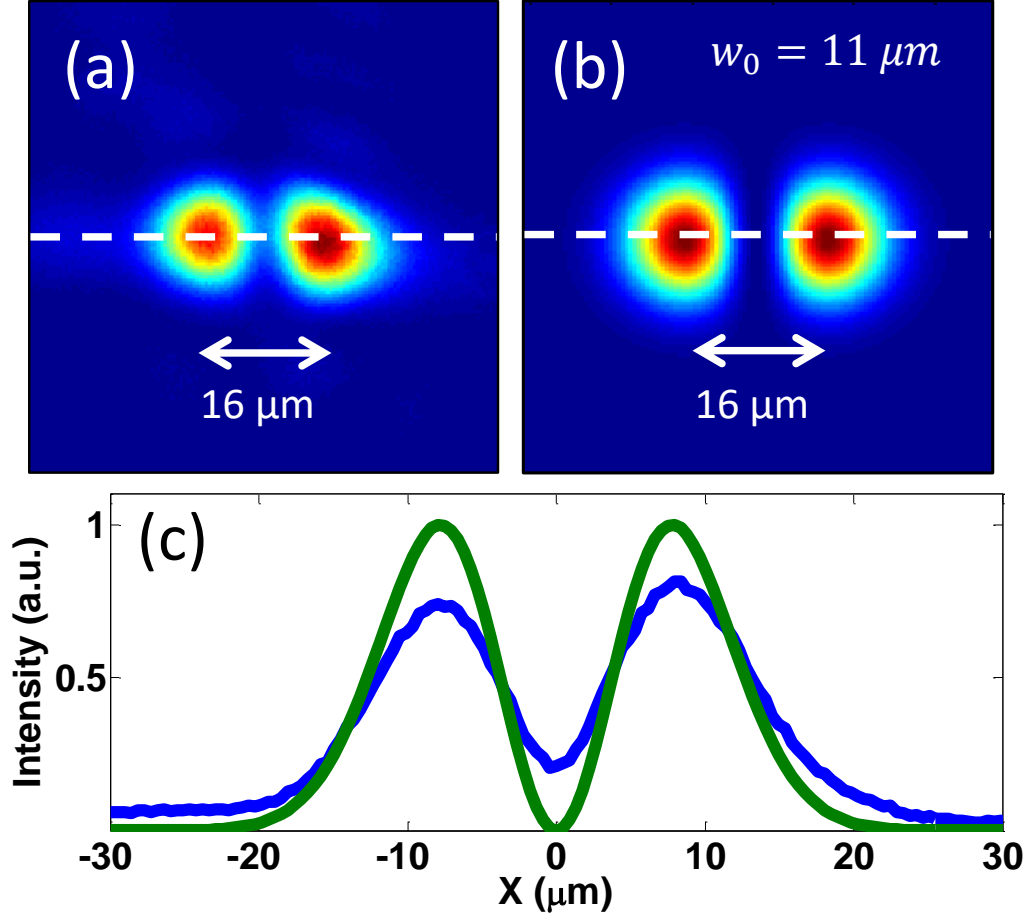


**Figure 4.6.** The focus of the half-pellicle beam (a) resembles a pure  $\text{TEM}_{01}$  Hermite-Gaussian mode (b). Lineouts along the maxima are compared in (c).

where  $w(z) = w_0 \sqrt{1 + z^2/z_R^2}$  is the beam spot size,  $R(z) = z(1 + z^2/z_R^2)$  is the beam phase front curvature,  $\eta(z) = \arctan(z/z_R)$  is the Guoy phase shift, and  $z_R = kw_0^2/2$  is the Rayleigh length [91]. Higher order modes can be derived from the fundamental mode by the recursion relation

$$\mathbf{E}_{nm}^{HG}(x, y, z) = w_0^{n+m} \frac{\partial^n}{\partial x^n} \frac{\partial^m}{\partial y^m} \mathbf{E}_{00}(x, y, z)$$

which yields

$$\mathbf{E}_{01}^{HG}(x, y, z) = -\frac{2xw_0}{w(z)^2} \left( 1 - \frac{ikw(z)^2}{2R(z)} \right) \mathbf{E}_{00}(x, y, z)$$

for the first higher order mode [190]. The paraxial approximation, by solving only the scalar wave equation, explicitly assumes  $E_z = 0$  and all modes are TEM. However, using Gauss's law we can at least approximate the longitudinal field near the beam waist as

$$E_z(x, y, z = 0) = - \int \frac{\partial}{\partial x} E_x(x, y, z) dz,$$

where the beam is assumed linearly polarized in the x direction and we take  $z = 0$  after the integration. For the  $E_{01}^{HG}$  mode this gives

$$E_z = - \frac{2i}{kw_0} E_0 \left[ 1 - \frac{2x^2}{w_0^2} \right] e^{-\frac{x^2+y^2}{w_0^2}}.$$

The longitudinal field is seen to be 90 degrees out of phase with the radial field and has a maximum on axis whereas the transverse field vanishes on axis with a maximum at  $x = w_0/\sqrt{2}$ . The ratio of longitudinal to transverse field maxima is found to be

$$\left| \frac{E_{max,z}}{E_{max,x}} \right| = \frac{\sqrt{2}e}{kw_0}.$$

For typical focusing parameters in our experiments,  $kw_0 \sim 80$  so  $\left| \frac{E_{max,z}}{E_{max,x}} \right| \sim 3\%$ . As might be expected, this is exactly half the peak accelerating field calculated in the paraxial limit for a purely radially polarized beam with the same peak electric field [81]. If we instead compare the peak longitudinal field,  $E_{z,max}^{01}$ , of a  $TEM_{01}$  mode to that of a purely radially polarized mode,  $E_{z,max}^r$ , with the same total energy, we find that  $E_{z,max}^{01} = \frac{E_{z,max}^r}{\sqrt{2}} = 0.707 * E_{z,max}^r$ .

#### 4.4 Guiding of a $TEM_{01}$ mode in a plasma channel

The approximately parabolic plasma channel described in Chapter 3 will support higher order modes, allowing matched guiding of the half-pellicle mode (near- $TEM_{01}$  mode) with its associated axial field component [61]. The controlled guiding of higher order modes in a plasma channel has never before been demonstrated experimentally to the best of our knowledge. Plasma waveguides were generated by focusing a 250mJ, 140ps Nd:YAG laser pulse over an 11 mm nitrogen cluster jet. The clusters ionize and collisionally absorb the Nd:YAG pulse. The plasma expands at the ion acoustic speed and after approximately 700 ps forms a density minimum on axis with an index profile supporting guided modes. Figure 4.7 shows the Abel-inverted density profile of the first 1.4 mm of the 11 mm plasma as well as a transverse lineout showing the density minimum on axis and the approximately parabolic density profile between the shock walls. Figure 4.7(c) and

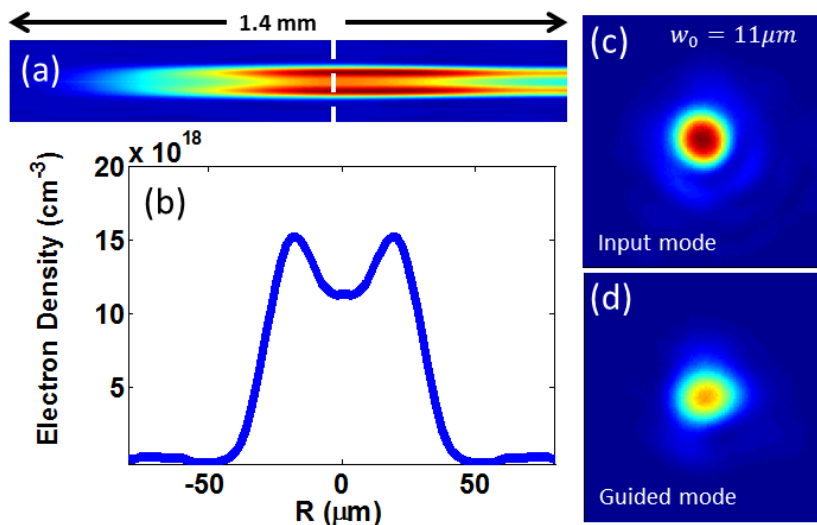


**Figure 4.7.** The Abel inverted density profile of the first 1.4 mm of an 11 mm nitrogen plasma waveguide (a) with a lineout shown in (b). A Gaussian input mode with an 11 μm spot size (c) is guided with approximately 60% energy throughput and the same spot size as the input mode (d).

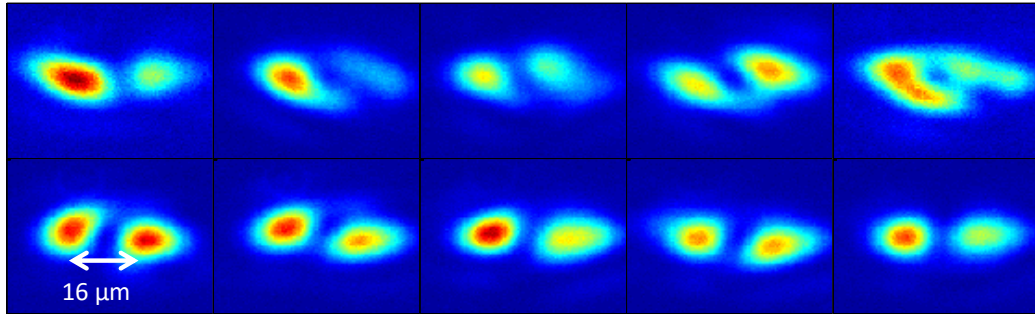


**Figure 4.8.** Series of guided modes at the exit of an 11 mm nitrogen plasma waveguide. The modes retain the two-lobe structure of the injected near- $TEM_{01}$  mode with an energy throughput of  $\sim 30\%$ .

4.7(d) show sample injected and guided Gaussian modes using the same spatial and color scales. The Gaussian input  $TEM_{00}$  mode (10 mJ, 40 fs) has a spot size of  $w_0 = 11 \mu m$ . Guided throughput is approximately 60% over a distance of 20 Rayleigh lengths with an 11  $\mu m$  spot size.

The half pellicle was inserted before the vacuum pulse compressor, and the beam was focused onto the entrance of the plasma waveguide with an injected focal spot profile shown in Fig. 4.6(a). The calculated  $w_0$  of the approximate  $TEM_{01}$  mode was 11  $\mu m$ , identical to the guided Gaussian mode in Fig. 4.7(d). Figure 4.8 shows a series of guided half-pellicle-injected modes from ten consecutive laser shots. The exit modes retain the  $TEM_{01}$  mode structure over the 11 mm propagation length with an average energy throughput of  $\sim 30\%$ . While the energy throughput is somewhat low, the expected peak longitudinal field at the exit of the plasma waveguide is still an impressive  $\sim 100$  MV/cm. Using the DLA relations for energy gain this gives a  $\sim 24$  MV/cm accelerating gradient. This is well within detection limits for a proof of principle DLA demonstration with an input mode energy of 10 mJ and 30% energy throughput.



## Chapter 5: Characterization of a micrometer-scale cryogenically cooled gas jet for near critical density laser-plasma experiments

### **5.1 Introduction**

Gas jets have been employed as targets in high intensity laser-matter interaction studies for decades. Experiments utilizing gas jets span a wide variety of applications including electron and ion acceleration [27,29,191,192], high harmonic generation [193,194], x-ray lasers [133], and even generation of fusion neutrons [195]. The main draw of gas jets, as compared to solid targets or static gas fills, is the ability to create a well-controlled, automatically replenishing target that can be used at relatively high repetition rate without requiring target rasterization schemes. Fine control of the gas density and profile has been demonstrated by multiple groups through engineering of the valve design [196–198], nozzle geometry [199–202], and through external shaping of the resulting gas flow [152,155,203,204].

In experiments with these gas jets, the electron density has generally been limited to less than  $\sim 10^{20} \text{ cm}^{-3}$ , with interaction lengths on the millimeter scale. This density precludes the study of the near critical plasma density regime with ultrashort Ti:Sapphire laser pulses ( $N_{crit} \approx 1.7 \times 10^{21} \text{ cm}^{-3}$ ). Two notable exceptions to this limitation are the schemes presented by Sylla et al. [197] and Kaganovich et al. [203] for achieving thin, high density plasmas suitable for the study of near critical phenomena. Sylla et al. achieved a critical density plasma by implementing a novel valve design which boosts the pressure above 4000 psi behind

a  $\sim 400$   $\mu\text{m}$  nozzle. Kaganovich et al. generate a shockwave in a standard gas jet by ablating a metal plate with a nanosecond laser a controlled time before the main interacting pulse. The density of the gas in the thin shock can be many times higher than the ambient gas density, boosting the target density into the near critical regime.

Here, a simple method for generating thin, near critical density plasmas which avoids complicated pressure boosting schemes or secondary lasers is presented. The technique hinges on the use of a cryogenically cooled high pressure solenoid valve coupled to a variety of thin nozzles with diameters as small as  $50$   $\mu\text{m}$ . Sonic nozzles are employed to maximize the peak molecule number density at the nozzle output for a given nozzle minimum diameter. The cryogenic cooling increases the molecule number density inside the reservoir for a fixed valve backing pressure which, in the isentropic limit, proportionally increases the number density at the orifice exit plane.

## ***5.2 High density valve design***

The valve used in the high density jet design is a solenoid valve held in a custom cooling jacket, shown in Fig. 5.1(c), which uses a combination of liquid nitrogen and electrically driven heating elements to control the valve reservoir temperature. The reservoir temperature can be controlled to within 1 degree Celsius between room temperature and  $\sim -160^\circ$  C. A series of custom nozzles was fabricated which attach to the solenoid valve with two main designs. The first design, shown in Fig. 5.1(a), uses a straight  $\sim 1$  cm long section of a thin needle which restricts the flow directly at the valve orifice. The second design, shown in Fig. 5.1(b), uses a precision tapered nozzle with 12 degree taper starting from  $\sim 2.5$  mm diameter at the base. The minimum inner diameters, referred to as the nozzle throat, ranged from  $50$   $\mu\text{m}$  to  $150$

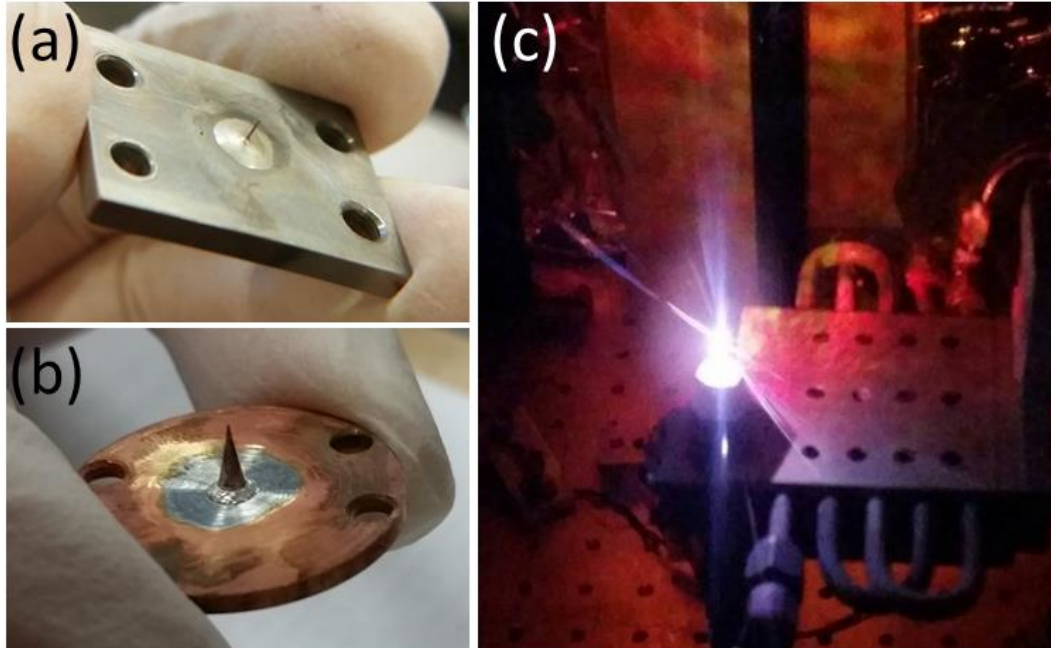


**Figure 5.1.** Custom fabricated straight (a) and tapered (b) nozzles with  $\sim 100 \mu\text{m}$  throats. The gas jet is held in a custom cooling block (c) which can cool the jet to cryogenic temperatures.

$\mu\text{m}$  for both nozzle designs. In all nozzles, a “sonic” design was employed where the nozzle diameter at the exit plane was equal to the throat diameter. This is in contrast to supersonic nozzles employing a converging-diverging (de Laval) design to reach high Mach numbers [205].

Controlling the reservoir temperature and pressure along with the nozzle exit diameter allowed us to access peak molecular densities in the range  $10^{19}$ - $10^{21} \text{ cm}^{-3}$ . The radial density profile of the gas flow was nearly Gaussian with full width at half maximum (FWHM) of 100-200  $\mu\text{m}$  depending on the diameter of the nozzle exit orifice. Depending on the gas species used, when ionized this covers underdense through overdense plasma regimes for an 800 nm Ti:Sapphire laser ( $N_{crit} \approx 1.7 \times 10^{21} \text{ cm}^{-3}$ ).

### 5.3 Isentropic flow model

The flow of gas from the jet can be modelled as the steady, one-dimensional isentropic flow of an ideal gas into a low pressure reservoir [206]. The gas in the valve reservoir is held at a given stagnation (zero velocity) temperature,  $T_0$ , and pressure,  $P_0$ . Flow from the reservoir is forced through a narrow orifice by the pressure gradient between the reservoir and vacuum chamber which is held at a pressure,  $P_b$ . We seek to calculate the molecule density,  $n$ , at the exit of the nozzle as a function of the reservoir and nozzle parameters.

The steady flow assumption is validated by measurements of the gas density as a function of time presented in section 5.5 which show a fast rise in the gas density output followed by a plateau. The isentropic flow assumption requires that the flow be adiabatic and inviscid. We can validate the adiabatic nature of the flow by calculating the heat transfer from the nozzle to the gas as it transits the nozzle. The total heat transfer is given by  $\Delta Q = -\kappa A \frac{dT}{dr} \Delta t$  where  $\kappa$  is the thermal conductivity of the gas ( $\kappa \approx 0.069 \text{ W/m/K}$  for hydrogen at 100 K [207]),  $A$  is the gas contact area which is taken to be the inner wall of the nozzle  $\sim 3 \text{ mm}^2$ , the temperature gradient  $dT/dr$ , taken across the diameter of the nozzle throat, is calculated using isentropic fluid equations presented below to be  $\sim 200 \text{ K/mm}$ , and the transit time  $\Delta t \sim 10 \mu\text{s}$  is estimated by assuming the gas flows at the sound speed ( $c_s = \sqrt{\gamma k_B T_0 / m} \approx 800 \text{ m/s}$ ) through the 1 cm long nozzle. With these parameters 0.5  $\mu\text{J}$  is transferred to the gas as it transits the nozzle. The change in temperature of the hydrogen gas through heat conduction is given by  $\Delta T = Q/C_v$  where  $C_v \approx 13 \text{ J/g/K}$  is the specific heat capacity of hydrogen at constant volume. For the nozzle volume of 0.2

mm<sup>3</sup> and a hydrogen molecule density  $\sim 10^{21}$  cm<sup>-3</sup> approximately 0.3  $\mu$ mol of hydrogen is contained in the nozzle at a given time. Therefore the 0.5  $\mu$ J transferred to the gas as it transits the nozzle yields a temperature change  $\sim 0.1$  K. This is much less than the temperature change in the gas due to expansion from the reservoir through the nozzle, which is  $\sim 10$  K calculated from the isentropic flow relations given below with  $M = 1$ , so we may use the adiabatic approximation.

The effect of viscosity on the flow can be expressed through the dimensionless Reynold's number,  $Re = \rho VD/\mu$ , where  $\rho$  is the fluid mass density,  $V$  is the flow velocity,  $D$  is the nozzle diameter, and  $\mu$  is the fluid dynamic viscosity. The Reynold's number represents the ratio of the inertial to viscous forces acting on the fluid, with high Reynold's numbers representing inertially dominated flow. We can estimate  $Re$  by considering a flow at the stagnation temperature and pressure within the jet reservoir moving through the needle nozzle at the sound speed. This will be shown below to give the correct order of magnitude for the Reynold's number under isentropic flow conditions. We consider the stagnation conditions  $T_0 = -160C = 113$  K,  $P_0 = 1000$  psi = 7 MPa,  $n_0 = 4.4 \times 10^{21}$  cm<sup>-3</sup> and  $c_s = \sqrt{\gamma k_B T/m} = 840$  m/s. The dynamic viscosity of hydrogen can be approximated by Sutherland's formula for the viscosity of an ideal gas,  $\mu = CT^{3/2}/(T + S)$  where  $C$  and  $S$  are empirically measured gas dependent constants [208]. For hydrogen,  $C = 0.64$  and  $S = 72$  [209] so at  $T_0 = 113$  K the dynamic viscosity is  $\mu = 4.2$   $\mu$ Pa  $\cdot$  s. Plugging these values in to the formula for  $Re$  with a tube diameter of 100  $\mu$ m gives  $Re \approx 3 \times 10^5$ . The boundary layer thickness,  $\delta_L$ , a distance  $L$  along the nozzle can be estimated as  $\delta_L/L \sim 1/\sqrt{Re} = .002$ . The needle aspect ratio is  $\sim 1/100$ , so the

boundary layer thickness at the exit of the needle is estimated to be about 20% of the nozzle diameter. The boundary layers may reduce the overall flow rate somewhat, but the flow near the center of the nozzle may be approximated as isentropic.

In an ideal isentropic flow one can express the gas temperature,  $T$ , and pressure,  $P$ , in terms of the gas specific heat ratio,  $\gamma = \frac{c_P}{c_V} > 1$  and the Mach number,  $M = V/c_s$  where  $V$  is the fluid velocity and  $c_s$  the sounds speed via [210]

$$\frac{T_0}{T} = 1 + \frac{\gamma - 1}{2} M^2 \quad (5.1)$$

$$\frac{P_0}{P} = \left( 1 + \frac{\gamma - 1}{2} M^2 \right)^{\frac{\gamma}{\gamma - 1}} \quad (5.2)$$

where  $P_0$  and  $T_0$  are the stagnation temperature and pressure (i.e. conditions where  $M = 0$ ). Equations (5.1) and (5.2) follow from the assumption that energy in the fluid is conserved so that the stagnation properties of the flow remain constant throughout the expansion. Further, since the flow is isentropic,  $Pn^{-\gamma} = \text{constant}$ , the gas density is given by

$$\frac{n_0}{n} = \left( 1 + \frac{\gamma - 1}{2} M^2 \right)^{\frac{1}{\gamma - 1}}. \quad (5.3)$$

Equation (5.3) indicates the fluid density drops rapidly as the Mach number increases. Therefore, to reach the highest density possible at the nozzle exit, the Mach number should be minimized.

Equations (5.1)-(5.3) also lead to the definition of the fluid critical properties, defined as the fluid state corresponding to exactly sonic flow ( $M = 1$ ) [210]. The critical properties, denoted with a \*, can be written in terms of the stagnation properties as

$$\frac{T^*}{T_0} = \frac{2}{\gamma + 1},$$

$$\frac{P^*}{P_0} = \left( \frac{2}{\gamma + 1} \right)^{\frac{\gamma}{\gamma - 1}},$$

$$\frac{n^*}{n_0} = \left( \frac{2}{\gamma + 1} \right)^{\frac{1}{\gamma - 1}}.$$

Consider the steady gas flow from a region held at high pressure,  $P_0$ , to a region held at low pressure,  $P_b < P_0$ , as is the case for the high pressure jet flowing into the vacuum chamber. If  $P_b < P^*$  then at some point between the (fixed) high and low pressure regions the flow will reach sonic velocity. For diatomic gases such as hydrogen,  $\gamma = 1.4$  and  $\frac{P^*}{P_0} = 0.528$ . The ratio between the jet backing pressure and the vacuum chamber background pressure is  $\sim 10^{-5}$ , so the flow from the jet will reach at least the sound speed. Since the jet output density given by equation (5.3) is strictly decreasing as a function of  $M$  and we know the flow must reach at least the sound speed as it exits the nozzle, the achievable output density is maximized by a nozzle which has  $M = 1$  at the exit plane, which is called a sonic nozzle. Sonic nozzles are achieved by using a converging or fixed nozzle cross section in contrast to supersonic nozzles which have a converging-diverging (de Laval) geometry [206].

The molecule density at the exit of the sonic nozzle is given by

$$n^* = n_0 \left( \frac{2}{\gamma + 1} \right)^{\frac{1}{\gamma - 1}} \cong 0.63 \times n_0 = 0.64 \times \frac{P_0}{k_b T_0} \quad (5.4)$$

where  $\gamma = 1.4$  for a diatomic gas and the ideal gas equation of state are assumed. Equation (5.4) shows that increasing the gas density at the nozzle exit can be achieved by increasing the gas density in the nozzle reservoir. From the equation of

state, increasing the reservoir density is achieved by increasing the nozzle backing pressure,  $P_0$ , or by decreasing the reservoir temperature,  $T_0$ . Cryogenic cooling of the reservoir temperature thus serves to increase the total jet output density proportional to  $T_0^{-1}$  where  $T_0$  is given in Kelvin.

## 5.4 Experimental setup

The output density of the gas jet as a function of temperature, pressure, and nozzle geometry was characterized by transverse interferometry with a  $< 100$  fs, 400 nm probe pulse derived from our 25 TW Ti:Sapphire laser system [141,211]. Figure 5.2 shows a diagram of the experimental setup. The phase shift due to the gas is extracted by shearing the 400 nm probe inside a folded wave front interferometer and extracting the phase shift through Fourier techniques [212]. The extracted 2D phase profile represents the phase shift,  $\Delta\phi(x)$ , accumulated by different chords through the gas profile and can be related to the radial gas density profile through the Abel transform

$$\eta(r) - 1 = -\frac{1}{k\pi} \int_r^{r_0} \left( \frac{d\Delta\phi(x)}{dx} \right) \frac{dx}{\sqrt{x^2 - r^2}} \quad (5.5)$$

and the relation

$$n(r) = \frac{\eta(r) - 1}{2\pi\alpha}.$$

Here  $\eta(r)$  is the gas refractive index,  $k = 2\pi/\lambda$  is the probe wavenumber,  $r$  is the radial coordinate,  $r_0$  is a radius at which the gas density goes to zero,  $n(r)$  is the gas number density, and  $\alpha$  is the gas molecular polarizability. The integral transform of equation (5.5) can be solved numerically or, with a suitable phase shift profile



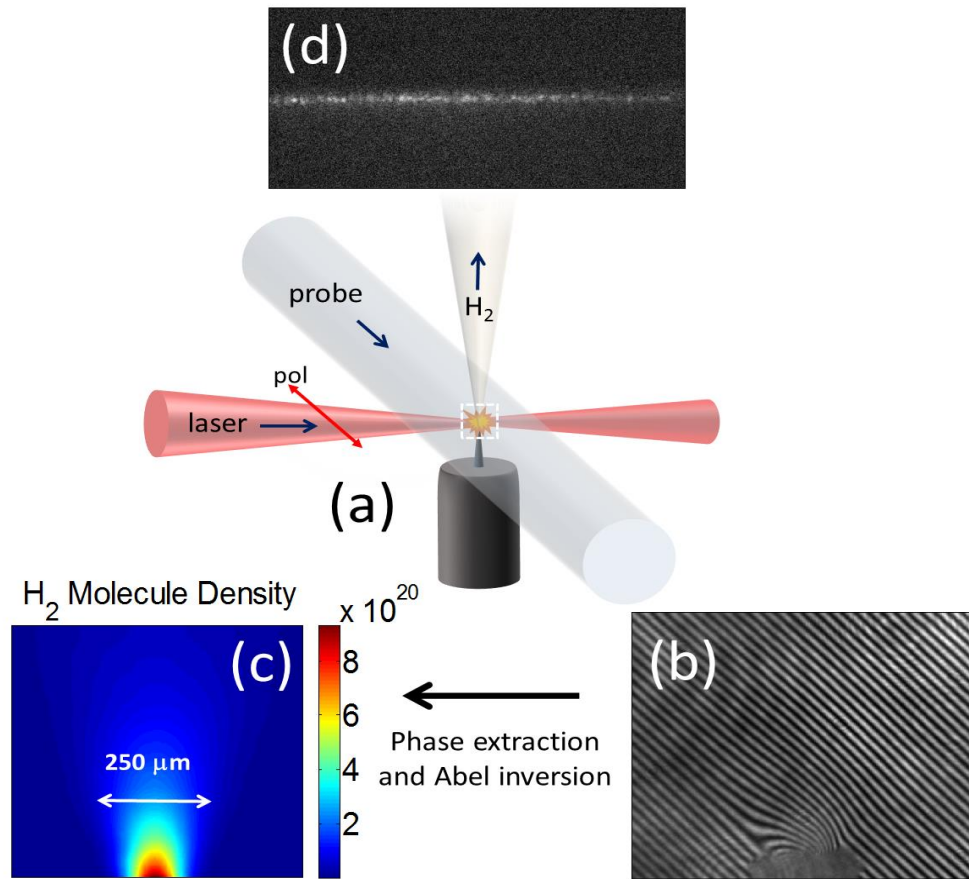


**Figure 5.2.** Experimental setup for characterizing the high density gas jet (a). Density measurements were made using transverse interferometry. A raw interferogram (b) and Abel inverted density profile (c) are shown along with a raw image of Rayleigh scattering used to measure the cluster size and density in the jet.

for  $\Delta\phi(x)$ , analytically. In all of our measurements  $\Delta\phi(x)$  was fit very well by a Gaussian function at heights  $50 \mu\text{m}$  or more above the nozzle orifice. Taking  $\Delta\phi(x) = \Delta\phi_0 \exp\left(-\frac{x^2}{\sigma^2}\right)$  over the full axis, then the Abel inverted radial index profile is calculated from equation (5.5) to be

$$\eta(r) - 1 = \frac{1}{k} \frac{\Delta\phi_0}{\sqrt{\pi}\sigma} \exp\left(-\frac{r^2}{\sigma^2}\right).$$

A numerical Abel inversion routine based on the fast Fourier transform was also implemented [213]. Numerical Abel inversion generally agreed with the analytical

Abel inversion using the Gaussian fit to within ~10%. The insets in Fig. 5.2 show a sample raw interferogram (b), Abel inverted density profile (c), and a sample image of Rayleigh scattering (d) used to measure cluster size in the high density jet.

## **5.5 Hydrogen jet density measurements**

Hydrogen gas is commonly used in laser plasma interaction experiments because of the ease with which it is fully ionized by the leading temporal edge of a suitably intense femtosecond laser pulse. Complete ionization mitigates ionization induced refraction of the main interacting pulse. However, since each hydrogen molecule can only contribute two electrons, high plasma densities have been very difficult to reach without the use of some higher Z dopant such as nitrogen or argon. Figure 5.3(a) shows a sample Abel inverted density profile of the hydrogen gas jet using a 100  $\mu\text{m}$  needle nozzle, 1000 psi backing pressure, and  $-160^\circ\text{C}$  reservoir temperature. The lineouts in Fig. 5.3(b) taken 70, 100, and 200  $\mu\text{m}$  above the nozzle show a near-Gaussian radial density profile. The peak molecule density 70  $\mu\text{m}$  above the nozzle is  $9 \times 10^{20}\text{cm}^{-3}$  which, when fully ionized, gives a peak plasma density of  $1.8 \times 10^{21}\text{cm}^{-3}$  or  $1.03 * N_{crit}$  for  $\lambda = 800\text{nm}$ . Figure 5.3(c) shows the exponential decay of the peak gas density as a function of height above the 100  $\mu\text{m}$  needle nozzle for a series of backing pressures. The decay length is approximately 67  $\mu\text{m}$  independent of the valve backing pressure. The exponential decay of the peak density is driven by the gas expansion, and the profile FWHM increases linearly as a function of height above the nozzle, as shown in Fig. 5.3(d).

To minimize gas loading of the experimental chamber, the solenoid valve should have a fast rise time, reaching a stable output with minimal background gas

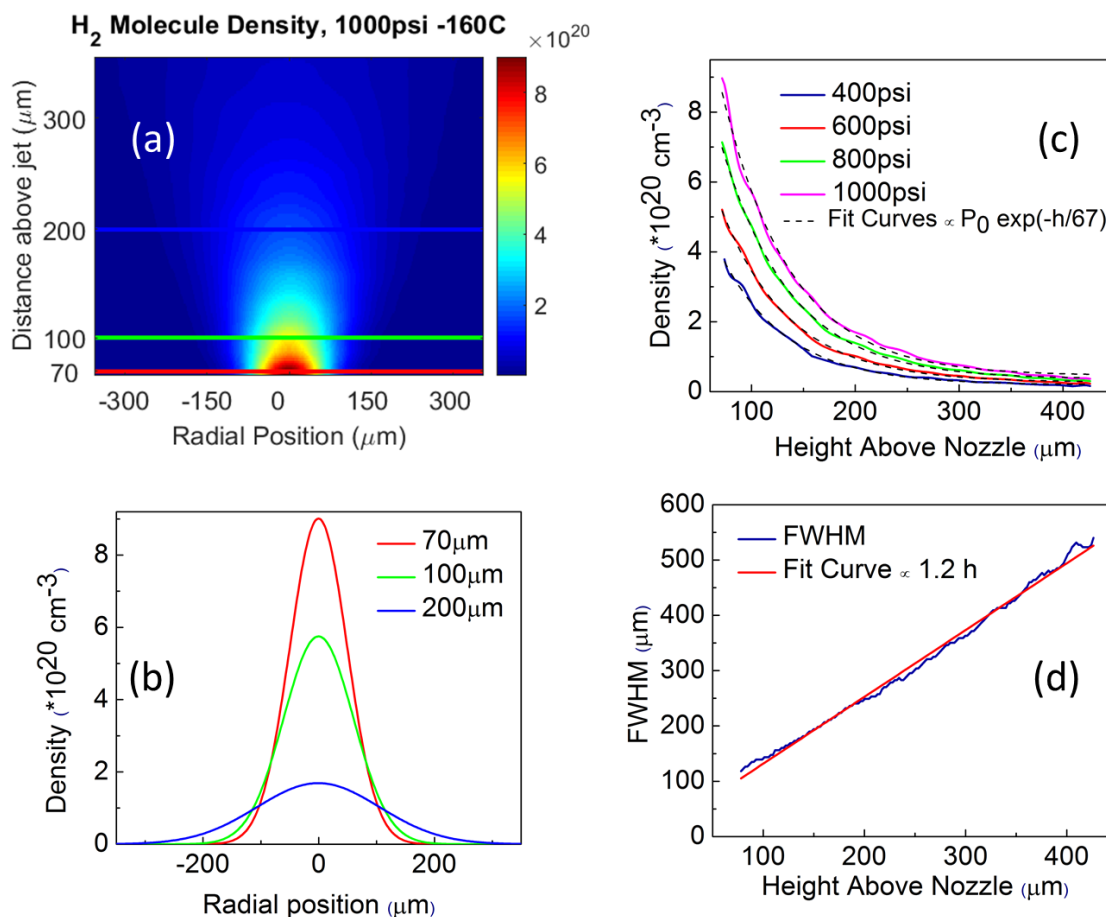


**Figure 5.3.** Sample 2D hydrogen molecule density profile (a) with 1000 psi backing pressure and  $-160^\circ \text{C}$  reservoir temperature and lineouts 70, 100, and 200  $\mu\text{m}$  above the nozzle (b). The peak density as a function of height decays exponentially (c) and the FWHM increases linearly with height above the jet (d).

filling the experimental chamber. Figure 5.4 shows the measured temporal evolution of the nitrogen gas output from a 100  $\mu\text{m}$  needle nozzle with the jet reservoir held at 800 psi and  $-110^\circ \text{C}$  for three different values of the valve opening time. Each point in Fig. 5.4 represents the maximum measured gas density at 200  $\mu\text{m}$  above the needle nozzle. The 10%-90% rise time of the gas density is approximately 400  $\mu\text{s}$  after which the measured output stabilizes for all three open times. The rise and fall times, measured as the time required for the gas density to go from 10%-90% of the peak value and vice versa, were found to be relatively independent of pressure,

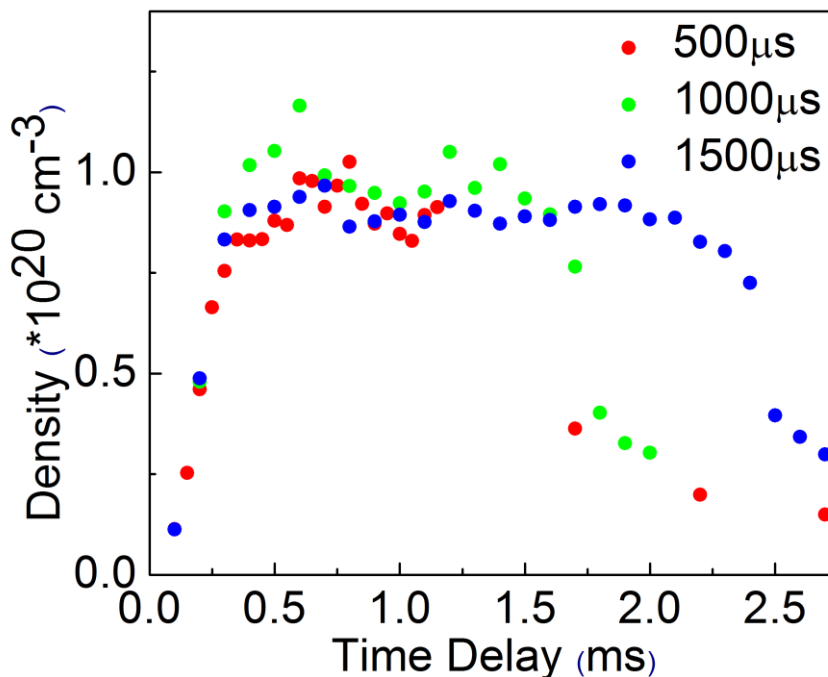


**Figure 5.4.** Nitrogen molecule density versus time delay at 200  $\mu\text{m}$  above the 100  $\mu\text{m}$  needle nozzle with the jet reservoir held at 800 psi and  $-110^\circ\text{C}$  for 500  $\mu\text{s}$ , 1000  $\mu\text{s}$ , and 1500  $\mu\text{s}$  open times.

temperature, and gas species, and a valve time of 700  $\mu\text{s}$  was used for all of the results in this chapter unless otherwise specified.

The isentropic flow model discussed in section 5.3 predicts a linear dependence of the gas output density on backing pressure and an inverse dependence on the reservoir temperature. Figure 5.5(a) shows the peak density 200  $\mu\text{m}$  above the 100  $\mu\text{m}$  diameter needle nozzle as a function of backing pressure with a fixed temperature of  $-160^\circ\text{C}$ . In agreement with the isentropic flow model, the measured density varies linearly with pressure. Figure 5.5(b) shows the dependence of the peak gas density at the same location for a fixed pressure of 1000 psi as a function of temperature. The peak density at  $-160^\circ\text{C}$  is enhanced by a factor of  $\sim 2.4$  compared to the peak density at room temperature, highlighting the effectiveness of cryogenic

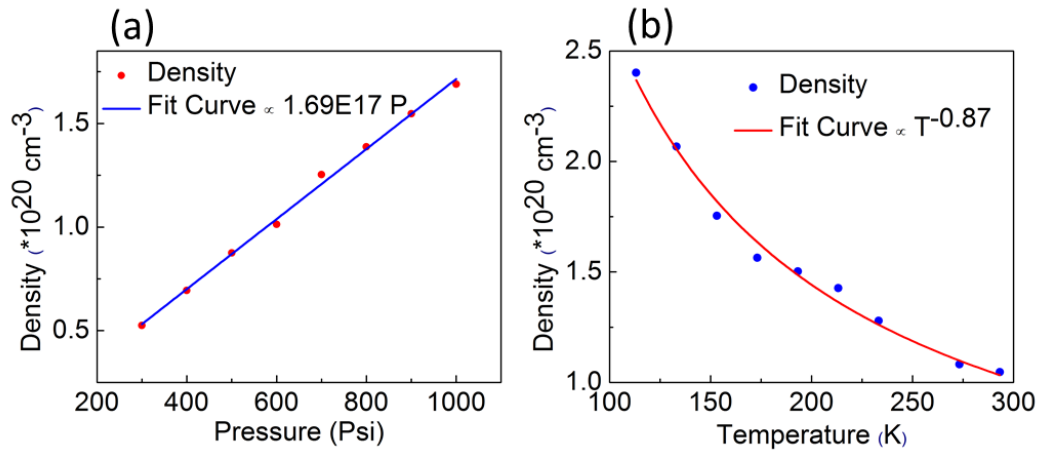


**Figure 5.5.** Peak jet density 200  $\mu\text{m}$  above the 100  $\mu\text{m}$  needle nozzle as a function of valve backing pressure at a fixed reservoir temperature  $-160^\circ \text{C}$  (113 K) (a) and as a function of reservoir temperature at a fixed backing pressure 1000psi (b).

cooling for increasing gas jet density output. The measured density as a function of temperature is roughly proportional to  $T_0^{-0.87}$ . Departure from the  $1/T_0$  dependence is possibly caused by viscous effects in the flow as the dynamic fluid viscosity,  $\mu$ , is a function of the fluid temperature [208].

Finally, the density was measured for a series of nozzles with throat diameters of 50, 100, and 150  $\mu\text{m}$  in both straight and tapered geometries. Viscous forces in the flow reduce the flow rate and thus the peak density at the nozzle exit for smaller diameter nozzles, consistent with the increased fraction of boundary layer flow discussed in section 5.3. Figure 5.6 shows the output density as a function of height for a fixed reservoir temperature and pressure of  $-160^\circ \text{C}$  and 1000 psi for five nozzle designs. The density is almost equal for the same throat diameter in the tapered and straight nozzle geometry. However, the total output in both cases increases rapidly with increasing nozzle diameter.

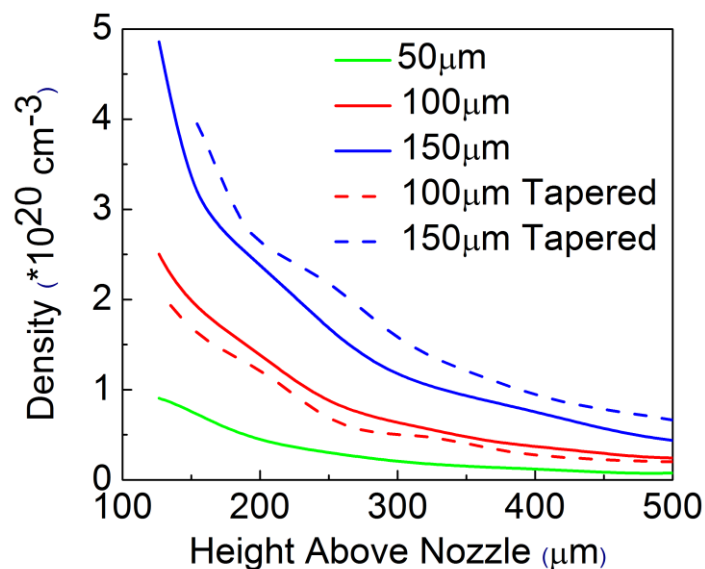


**Figure 5.6.** Density as a function of height above the needle (solid) and tapered (dashed) nozzles with 50 (green), 100 (red), and 150 (blue)  $\mu\text{m}$  throat all at  $-160^\circ\text{C}$  and 1000 psi .

## 5.6 Cluster size and density characterization

### 5.6.1 Cluster formation in high pressure gas jets

In many experiments involving high pressure gas jets clustering of molecules can play an important role. Collisional ionization within the solid density clusters can greatly enhance ionization and increase laser-plasma coupling [149,214]. The laser cluster interaction has been demonstrated as a source of fast ions [191,215], electrons [216,217], x-rays [214,218], and even neutrons [195,219]. Ballistic cluster flows can also be used to make shaped plasma density profiles using obstructions smaller than the cluster mean free path [152].

The size and density of clusters formed in expanding gas jets has been empirically characterized by Hagena [153,220,221], who introduced the scaling parameter

$$\Gamma^* = \frac{k d^{0.85} P_0}{T_0^{2.29}}. \quad (5.6)$$

Here  $k$  is a gas dependent constant,  $d$  is the jet orifice diameter in  $\mu\text{m}$ ,  $P_0$  is the backing pressure in mbar, and  $T_0$  is the jet stagnation temperature in Kelvin [220]. The value of  $k$  varies widely for different gases generally with larger values for more polarizable species. For example,  $k = 1650$  for argon and  $k = 180$  for hydrogen, while for helium  $k = 3.85$  and there is negligible clustering [153,220].

Clustering starts to be observed for  $\Gamma^*$  in the range of 200 – 1000 [221]. The average number of molecules in a cluster as a function of  $\Gamma^*$  was empirically characterized in the range  $10^2 < \Gamma^* < 10^6$  and scales as  $\langle n_c \rangle = 33 \left( \frac{\Gamma^*}{1000} \right)^{2.35}$  [221–223]. The dependence of  $\langle n_c \rangle$  on  $\Gamma^{*2.35}$  shows that larger clusters nucleate at higher pressures and lower reservoir temperatures and from nozzles with larger diameters ( $\langle n_c \rangle \propto \Gamma^{*2.35} \propto P_0^{2.35} T_0^{-5.38} d^{2.00}$ ).

### 5.6.2 Rayleigh scattering-based cluster measurement

The mean size and density of clusters in the high density gas jet can be estimated through an all optical technique combining transverse interferometry and collection of Rayleigh scattered light from the clusters. The technique, first demonstrated by Kim et al. [224], assumes complete clustering within the jet. The Rayleigh scattered energy into a collection lens by a laser propagating from point  $x$  to  $x + \Delta x$  through a cluster jet is given by  $\Delta E_{lens}(x) \approx E_{in} \bar{\sigma}_{lens}(x) N_c(x) \Delta x$  where  $E_{in}$  is the incident laser energy on the scattering volume,  $\bar{\sigma}_{lens}$  is the cross section for scattering into the lens averaged over the cluster size distribution, and  $N_c$  is the

average cluster density. For  $90^\circ$  scattering and cluster sizes much less than the laser wavelength  $\sigma_{lens} = \pi k^4 |\gamma| (\alpha^2 - \alpha^4/4)$  where  $k = 2\pi/\lambda$  is the laser wavenumber,  $\gamma = a^3(\varepsilon - 1)(\varepsilon + 2)^{-1}$  is the cluster polarizability assuming a spherical cluster of radius  $a$  and dielectric constant  $\varepsilon$ , and  $\alpha$  is the collection half angle of the imaging lens. Using this cross section in the equation for the scattered energy gives

$$\overline{a^6} N_c = \frac{1}{\pi k^4} \left| \frac{\varepsilon + 2}{\varepsilon - 1} \right|^2 \frac{\Delta E_{lens}}{E_{in} \Delta x} \left( \frac{1}{\alpha^2 - \alpha^4/4} \right) \quad (5.3)$$

where  $\overline{a^6}$  is the average, over the cluster size distribution, of  $a^6$ . Transverse interferometry allows measurements of the real part of the refractive index  $n_r(x) = 1 + 2\pi N_c \gamma_r$  where  $\gamma_r = Re(\gamma)$ . Rearranging gives

$$\overline{a^3} N_c = \frac{n_r(x) - 1}{2\pi} \left( \frac{\varepsilon + 2}{\varepsilon - 1} \right) \quad (5.4)$$

Combine equations (5.7) and (5.8) yields an effective cluster radius  $a_{eff} \equiv (\overline{a^6}/\overline{a^3})^{1/3}$  and number density  $N_{c,eff} \equiv \overline{a^3} N_c / a_{eff}^3$  [211].

The above model, which assumes complete clustering, requires consideration of the effect of a non-zero monomer concentration on extracted measurements of  $a_{eff}$  and  $N_{c,eff}$ . If the jet contains a monomer fraction  $\delta_m = N_m / (N_m + N_c \overline{n_c})$  where  $N_m$  is the monomer density and  $\overline{n_c}$  is the number of atoms within the cluster averaged over the cluster size distribution within the jet, then the assumption of complete clustering causes an underestimation of  $a_{eff}$  by a factor  $(1 - \delta_m)^{-1/3}$ . The underestimation arises from the additional contribution of the monomers to the measured phase shift while contributing negligibly to the Rayleigh scattered signal. The cube root dependence greatly damps the effect of the uncertainty in  $\delta_m$  since



even an assumption of 95% monomers only increases the calculated  $a_{eff}$  by a factor of 2.7. Further, the effect of the cluster size distribution on  $a_{eff}$  can be calculated by comparing  $a_{eff} \equiv (\overline{a^6}/\overline{a^3})^{1/3}$  to  $\bar{a}$  for various cluster size distributions,  $f(a)$ , where  $\overline{a^n} = \int_0^\infty a^n f(n_c) dn_c$  and  $a = r_{WS} n_c^{1/3}$  with  $r_{WS}$  the intra-cluster Wigner-Seitz radius. Using a log normal distribution for the number of molecules per cluster, we find that this method will tend to overestimate the cluster size. However, if the distribution is sufficiently narrow that the variance is within 40% of the mean, then the retrieved cluster size,  $a_{eff}$ , will be correct to within a factor of 2.

Rayleigh scattering is collected from the cluster jet by focusing a 25 mJ, ~10 ns cavity dumped beam from our Ti:Sapphire system into the thin jet at f/9.5. A calibrated imaging system collects the scattered signal in a plane perpendicular to the pump polarization and images the signal onto a CCD camera. The experimental setup and a raw image of the Rayleigh scattered light are shown in Fig. 5.2. The same transverse interferometry diagnostic described in section 5.2 was used to measure the clustered gas refractive index.

The hydrogen cluster size and density is found to vary as a function of the beam height above the nozzle orifice. Near the orifice, where the hydrogen molecule density is highest, no Rayleigh scattering was detected. A stronger Rayleigh scatter signal was observed farther from the nozzle, consistent with cooling-induced clustering as the gas expands into vacuum. Figure 5.7 shows the cluster size and density as a function of radial position at various heights above the 150  $\mu\text{m}$  diameter tapered nozzle with a jet backing pressure of 1000 psi and reservoir temperature - 160° C. The minimum average cluster radius measured for any conditions was

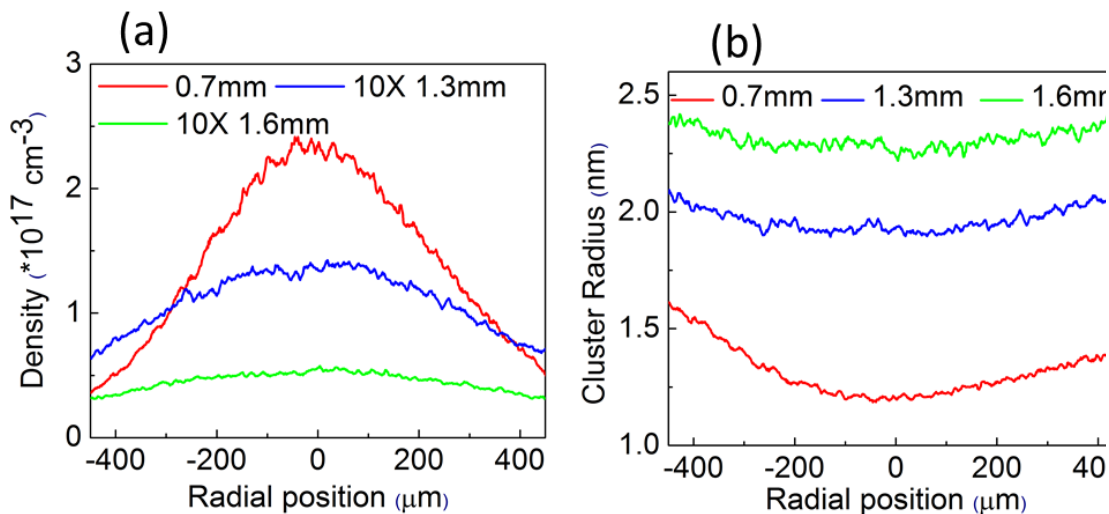


**Figure 5.7.** Average cluster density (a) and average cluster size (b) as a function of radial position at various heights above the 150  $\mu\text{m}$  diameter nozzle orifice at jet backing pressure and temperature 1000 psi and  $-160^\circ \text{C}$ .

approximately 0.5 nm limited by the photon collection efficiency of the Rayleigh scatter imaging system.

At positions greater than approximately 500  $\mu\text{m}$  above the jet the cluster size is measurable and the dependence of clustering on jet backing pressure and reservoir temperature can be determined. The left panel of Fig.5.8 shows the nonlinear dependence of the spatially integrated Rayleigh scatter signal on jet backing pressure at a height  $\sim 1$  mm above the 150  $\mu\text{m}$  nozzle when the jet reservoir temperature is held at  $-160^\circ \text{C}$ . The right panel of Fig. 5.8 shows the cluster size (dotted line) and density (solid line) at the same position as a function of backing pressure. The effective cluster radius dropped rapidly as the valve temperature was increased. The average cluster radius measured 1 mm above the 150  $\mu\text{m}$  needle nozzle with 1050 psi backing pressure and  $-160^\circ \text{C}$  was 1.8 nm. When the temperature was raised to  $-140^\circ \text{C}$  the cluster radius dropped to 0.5 nm for the same backing pressure. Above  $-140^\circ \text{C}$  the cluster size was too small to be measured by the Rayleigh scatter diagnostic.

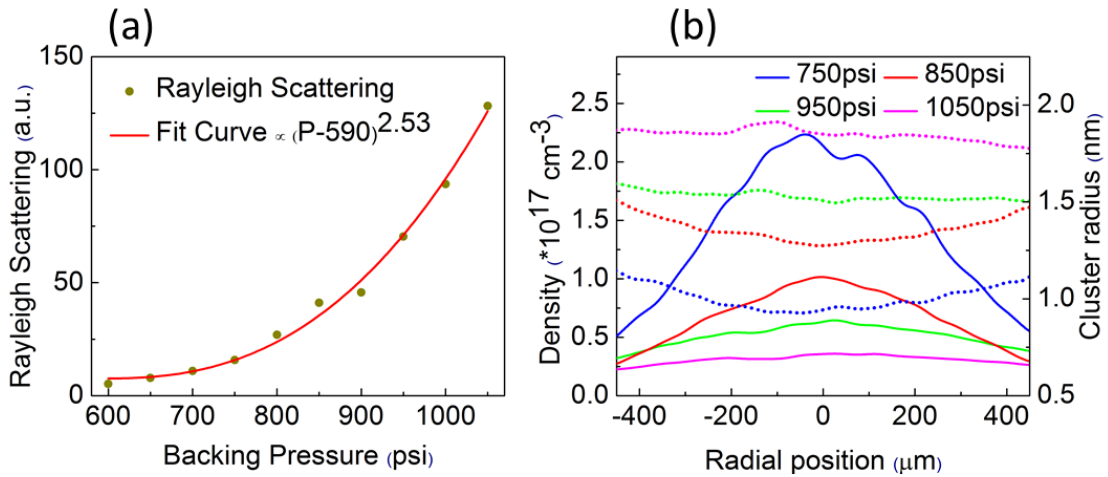


**Figure 5.8.** Rayleigh scatter signal versus backing pressure (a) and cluster density (solid line) and size (dotted line) at a height  $\sim 1$  mm above the  $150 \mu\text{m}$  nozzle (b) with the jet reservoir held at  $-160^\circ \text{C}$ .

## 5.7 Conclusion

The development of thin, high density gas jet targets for near critical laser-plasma interaction experiments with Ti:Sapphire laser systems has thus far been limited to a few, rather complicated, efforts. In this chapter a jet design based on a cryogenically cooled pulsed solenoid valve with needle and tapered nozzles was described. The jet was shown to be capable of reaching hydrogen molecule densities as high as  $9 \times 10^{20} \text{ cm}^{-3}$  in a  $\sim 200 \mu\text{m}$  FWHM Gaussian density profile when the jet was backed with 1000 psi and cooled to  $-160^\circ \text{C}$ . When fully ionized, this brings the peak plasma density above the (non-relativistic) critical density for Ti:Sapphire lasers, making this jet an interesting target for electron and ion acceleration experiments, as exemplified by the electron acceleration experiments performed using this jet presented in the next chapter.

Estimates of the output density scaling with the valve backing pressure and reservoir temperature were made by modelling the gas flow through the nozzle as

steady and isentropic. Reaching the highest density output possible was found to require a sonic nozzle design with the output molecule density directly proportional to the molecule density within the valve reservoir. Through the equation of state this means the gas density at the nozzle exit scales as  $T_0^{-1}$  so that cryogenic cooling of the jet reservoir serves to increase the valve output density. Rayleigh scatter measurements showed that clustering of the high density gas occurs only  $\sim 500 \mu\text{m}$  and farther above the nozzle. Effective cluster radii  $\sim 1 \text{ nm}$  were measured approximately 1 mm above the nozzle for the highest backing pressures and coldest reservoir temperatures. The cluster size measurements show that clustering is negligible in experiments operating near the nozzle exit plane where the gas density is highest.

## Chapter 6: Multi-MeV electron acceleration by sub-terawatt laser pulses in high density plasma

### **6.1 Introduction**

Laser-driven electron acceleration in plasmas has achieved many successes in recent years, including record acceleration up to 4 GeV in a low emittance quasi-monoenergetic bunch [31] and generation of high energy photons [38,41,225–227]. In these experiments, the driver laser pulse typically propagates in the ‘bubble’ or ‘blow-out’ regime [80,228] for a normalized peak vector potential  $a_0 = eA_0/mc^2 \gg 1$ . Plasma densities are deliberately kept low for resonant plasma wave excitation and to avoid dephasing [80]. Essentially all of these experiments use 10 TW –1 PW laser drivers, with repetition rates ranging from 10 Hz to one shot per hour [229]. Even the electron acceleration experiments described in Chapter 3, where ionization injection and plasma channel guiding were leveraged to reduce the laser energy threshold for electron beam production, required multi-terawatt drive laser pulses to generate relativistic electron beams.

For many modest lab scale and portable applications, however, a compact, relatively inexpensive, high average current source of laser-accelerated relativistic electrons is sufficient and desirable. This chapter describes an experiment using the very dense and thin hydrogen gas jet characterized in Chapter 5, where the relativistic self-focusing threshold is exceeded even with ~10 mJ laser pulses and MeV-scale energy electron bunches are generated. This enables applications, such as ultrafast low dose medical radiography, which would benefit from a truly portable source of

relativistic charged particle beams. The electron beams generated from interaction with the high density are also an interesting seed source for injection into secondary acceleration stages, such as the QPM-DLA scheme described in Chapter 4. Prior work has shown electron bunch generation of modest charge and acceleration ( $\sim 10$  fC/pulse,  $< 150$  keV) from a 1 kHz,  $\sim 10$  mJ laser driving a thin ( $\sim 100$   $\mu\text{m}$ ), low density continuous flow argon or helium jet [230].

## **6.2 Experimental setup**

Central to our experiment is the thin, high density pulsed hydrogen sonic gas jet described in Chapter 5, which reaches a maximum peak molecular density of  $9 \times 10^{20}$   $\text{cm}^{-3}$ , and when fully ionized can exceed the plasma critical density,  $N_{cr} = 1.7 \times 10^{21}$   $\text{cm}^{-3}$  at our laser wavelength of  $\lambda_0 = 800 \text{nm}$ . The density profile is near-Gaussian, with a full width at half maximum (FWHM) in the range 150-250  $\mu\text{m}$ , depending on the height of the optical axis above the jet orifice. Earlier versions of this jet were run in both pulsed [75] and continuous flow [231] for nitrogen and argon. High densities are achieved using a combination of high valve backing pressure and cryogenic cooling of the valve feed gas, which is forced through a 100  $\mu\text{m}$  diameter needle orifice. Cooling to  $-160^\circ \text{C}$  enables a significant density increase for a given valve backing pressure.

Figure 6.1 shows the experimental setup. Pulses from a Ti:Sapphire laser (50 fs, 10-50 mJ) are focused into the gas jet (Fig 1a) at  $f/9.5$  by a  $15^\circ$  off-axis parabolic mirror. Figure 6.1(b) shows neutral hydrogen profiles measured by interferometry. The wave front sensor and deformable mirror described in Chapter 2 are used to

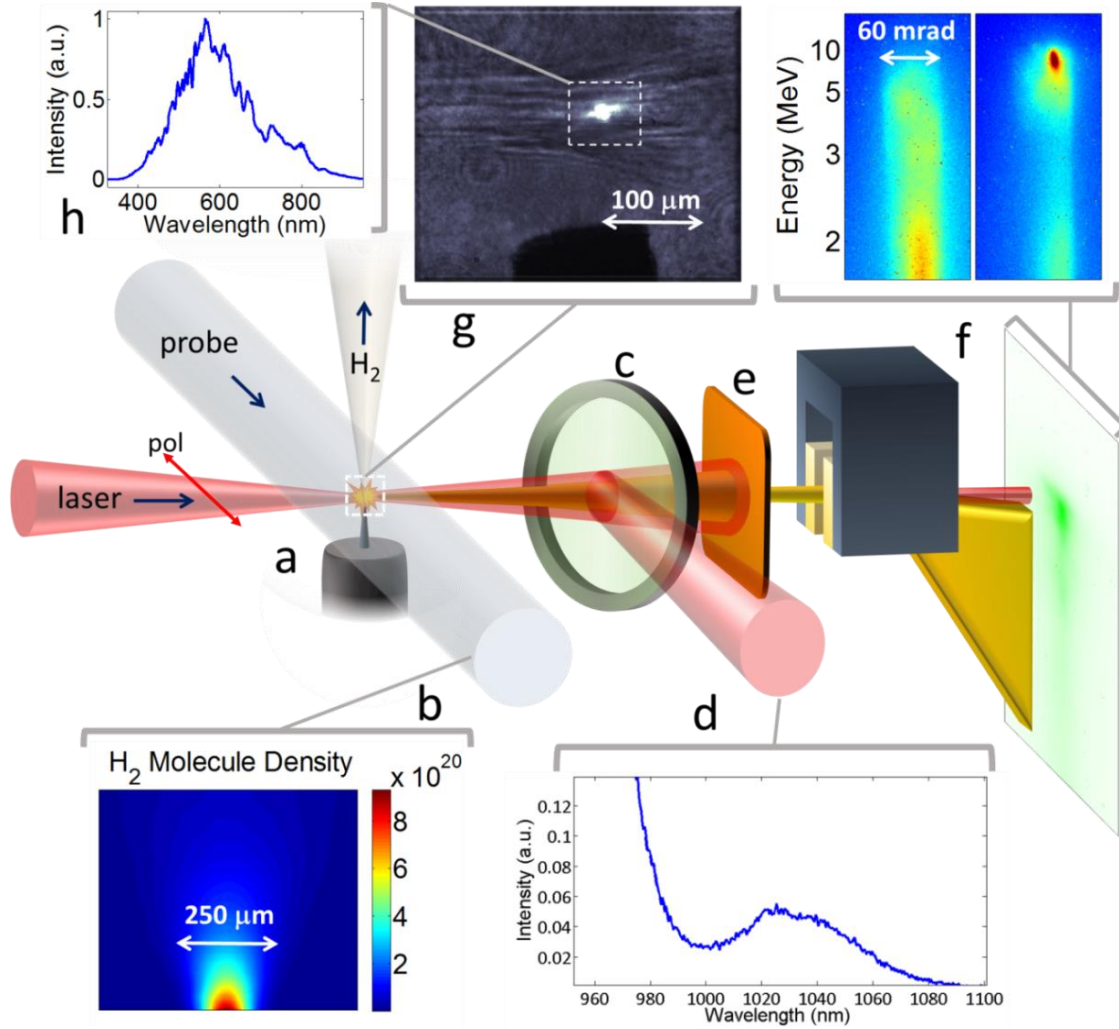


**Figure 6.1.** Experimental setup. A horizontally polarized Ti:Sapphire laser pulse (10-50 mJ, 50 fs,  $\lambda=800$  nm) interacts with a cryogenically-cooled, dense thin  $H_2$  gas jet (a), whose neutral and plasma density profiles are measured by 400 nm probe interferometry (b). A portion of the transmitted laser pulse is reflected by a pellicle (c) and measured by a spectrometer (d). The electron beam from the jet is apertured by a 1.7mm horizontal slit (e), enters a 0.13 T permanent magnet spectrometer, and is dispersed on an aluminum foil-shielded LANEX screen (f), which is imaged by a low noise CCD camera (not shown). (f) shows example quasi-monoenergetic and exponential spectra for a 40 mJ pulse at  $N_e=2\times 10^{20}$   $cm^{-3}$ . Shadowgraphic imaging of the laser interaction region above the needle orifice (g) (needle seen as a shadow at bottom) and imaging (g) and spectroscopy (h) of the wave breaking flash. The pump polarization could also be rotated to the vertical by a half wave plate.

optimize the vacuum focal spot to  $W_{FWHM} = 8.4$   $\mu m$  ( $1.2\times$  the diffraction limit)

containing 80% of the pulse energy, with a confocal parameter of 550  $\mu m$ . For

maximizing electron beam charge and energy, it was found that placing the focused

beam waist at the center of the gas jet was optimal, without strong sensitivity to positioning. This is consistent with the laser confocal parameter being more than twice the jet width. We note that recent laser interaction experiments at near critical density [232,233] have used a complex pressure-boosted millimetre-scale gas jet [197].

The neutral jet density and plasma profiles were measured using a 400nm, 70fs probe pulse (Fig. 6.1(b), derived from the main pulse), which was directed perpendicularly through the gas jet to a folded wave front interferometer. Forward- and side-directed optical spectra were collected by fibre-coupled spectrometers, with the forward spectra directed out of the path of the pump laser and electron beam by a pellicle (Fig. 6.1(c)). Shadowgraphic images using the 400 nm probe and images of bright broadband wave breaking radiation flashes were collected using achromatic optics.

Relativistic electron spectra in the energy range 2–15 MeV were measured using a 0.13 T permanent magnet spectrometer 25 cm downstream of the gas jet (Fig. 6.1(f)). A copper plate with a 1.7 mm  $\times$  12 mm slit aperture in front of the magnet entrance (Fig. 6.1(e)) provided energy resolution while allowing measurement of beam divergence in 1D. Electron spectra were dispersed along a LANEX scintillating screen, shielded against exposure to the laser by 100  $\mu$ m thick aluminum foil, and imaged using a low noise CCD camera. Full electron beam profiles were collected by the LANEX screen by translating the dispersing magnets and slit aperture out of the way. Estimates of the accelerated charge were made by calibrating the imaging system and using published LANEX conversion efficiencies [161,162].



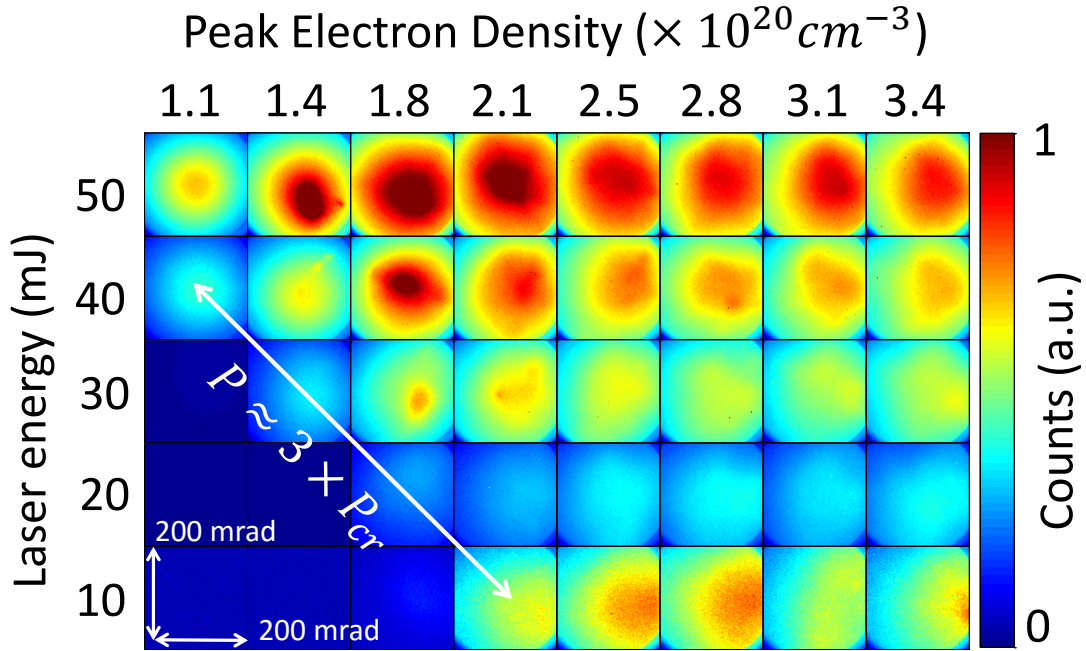


**Figure 6.2.** Single shot electron beam images for energies  $> 1$  MeV for a range of laser energies and peak profile electron densities. The colour palette was scaled up by  $10\times$  for the 10 mJ column. The onset laser power for detectable electron beam generation was  $\sim 3P_{cr}$  across our range of conditions.

### 6.3 Electron acceleration

The high density of our target has the immediate effect of enabling relativistic self-focusing of low energy laser pulses and generation of a nonlinear plasma wake. Furthermore, the reduced laser group velocity (and therefore plasma wave phase velocity) at high density drops the threshold for electron injection. Figure 6.2 shows  $> 1$  MeV electron beam generation for pulse energies in the range 10-50 mJ, or 0.2–1.0 TW, as a function of peak plasma density. Beam divergence is  $\lesssim 200$  mrad. The results are consistent with the inverse density scaling of the relativistic self-focusing critical power,  $P_{cr} = 17.4(N_{cr}/N_e)$  GW [234,235], and the laser power threshold for appearance of a relativistic electron beam is  $\sim 3P_{cr}$  across our range of conditions.

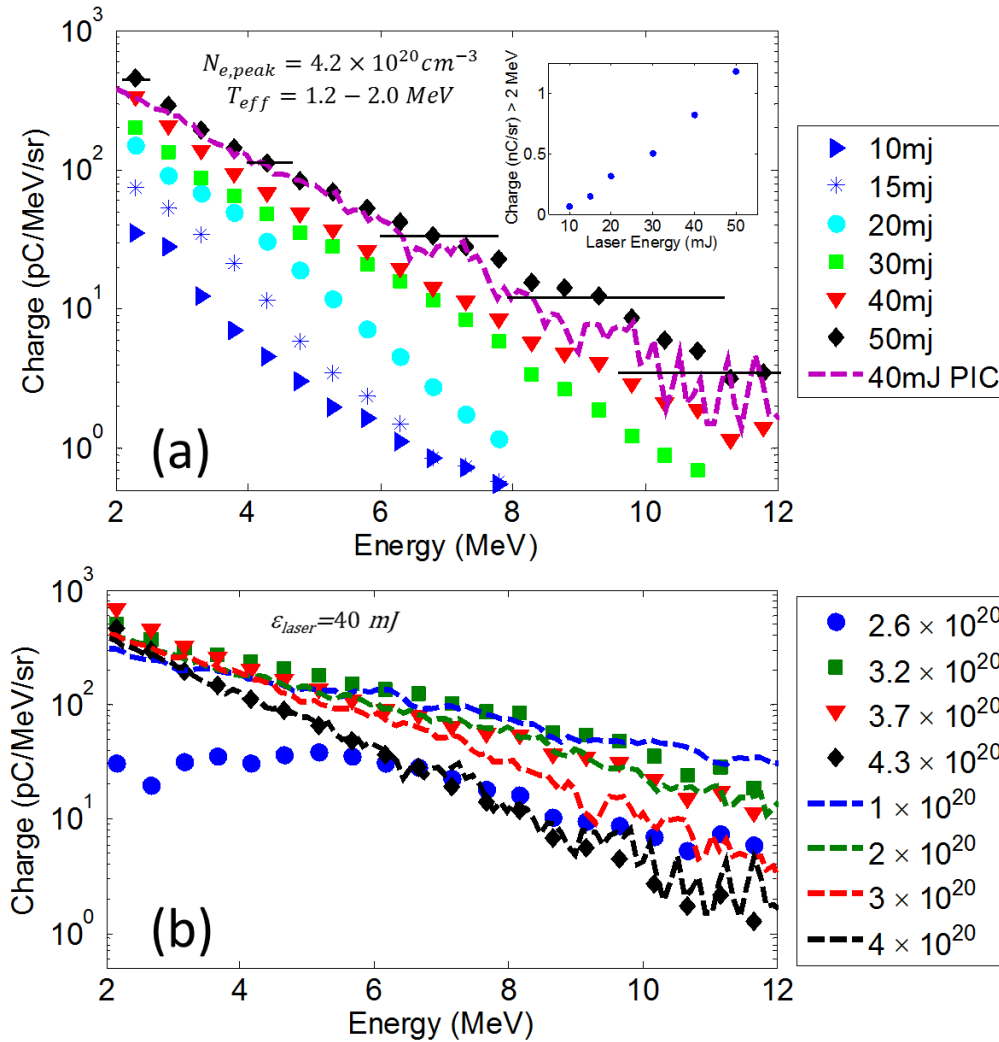


**Figure 6.3.** (a) Accelerated electron spectra for peak jet electron density  $4.2 \times 10^{20} \text{ cm}^{-3}$  for varying laser energy. The inset shows total charge  $> 2 \text{ MeV}$  as a function of laser energy. The range of effective temperatures of these exponential-like distributions is indicated. The horizontal black lines indicate the experimental uncertainty in the energy, determined by geometry-limited spectrometer resolution. The dashed curve is a 3D PIC simulation for 40 mJ pump which has been scaled by a factor 0.14 to line up with the experimental curve for 40 mJ. (b) Accelerated electron spectra at laser energy 40 mJ for varying peak electron density. The dashed curves are from 3D PIC simulations and were scaled by the factor 0.14.

Electron energy spectra in the range 2–12 MeV are shown in Fig 6.3(a) for laser pulse energy 10-50 mJ and peak electron density  $N_e = 4.2 \times 10^{20} \text{ cm}^{-3}$ , with the inset showing total accelerated charge  $> 2 \text{ MeV}$  up to  $\sim 1.2 \text{ nC/sr}$  for 50 mJ laser pulses. An electron spectrum simulated from a TurboWAVE 3D particle in cell (PIC)

simulation [163] for the 40 mJ case is overlaid on the plot. Electron spectra as a function of peak density for fixed pulse energy of 40 mJ are shown in Fig. 6.3(b) along with results from the 3D PIC simulations. We note that for approximately 20% of shots near the self-focusing onset at each pressure, we observed quasi-monoenergetic peaks ranging from 3 MeV ( $\sim 25$  fC for 10 mJ) to 10 MeV ( $\sim 1.4$  pC for 50 mJ, see Fig. 6.1(f) with  $\sim 10$  mrad beam divergence. Both the spectra and the beam spot positions are highly variable and are the subject of ongoing work.

Another consequence of the high density gas target interaction is that the pump pulse envelope is multiple plasma periods long. Over our experimental density range of  $N_e = 1 - 4 \times 10^{20} \text{ cm}^{-3}$ , the plasma period is  $2\pi/\omega_0 \sim 11 \text{ fs} - 5.7 \text{ fs}$ , placing our 50 fs pump pulse in the self-modulated laser wakefield acceleration (SM-LWFA) regime. Evidence of SM-LWFA is seen in the moderately collimated electron beams of Fig. 6.2 and the exponential electron spectra of Fig. 6.3, reflecting acceleration from strongly curved plasma wave buckets and electron injection into a range of accelerating phases. This is consistent with prior SM-LWFA experiments [24,56,236], except that here our dense hydrogen jet enables production of MeV spectra with laser pulses well below 1 TW. Further confirmation of self-modulation is seen in the spectrum of Raman forward scattered Stokes radiation shown in Fig. 6.1(d), for the case of laser energy 50 mJ (vacuum  $a_0 \sim 0.8$ ) and peak density  $N_e = 1.8 \times 10^{20} \text{ cm}^{-3}$ . The strong broadband red-shifted Raman peak located at  $\lambda_s = 2\pi c/\omega_s \sim 1030 \text{ nm}$  enables the estimate of self-focused  $a_{sf} \sim 2.7$ , using the measured electron density profile and  $\omega_s = \omega - \omega_p/\sqrt{\gamma}$ , where  $\omega$  is the laser

frequency and  $\gamma = (1 + a_{sf}^2/2)^{1/2}$  is the relativistic factor. This estimate is in good agreement with the peak  $a_{sf}$  in our 3D PIC simulations.

## **6.4 Wave breaking radiation**

In order for electrons to be accelerated, they must first be injected into the wakefield. Our 3D simulations show transverse wave breaking [65] of the strongly curved plasma wave fronts [237] behind the laser pulse, which injects electrons from a wide spread of initial trajectories into a range of phases of the plasma wave. Wave breaking is accompanied by a broadband radiation flash emitted by electrons accelerated from rest to near the speed of light in a small fraction of a plasma wavelength. Figure 6.1(g) shows a magnified single shot image of the sideways-collected flash superimposed on a shadowgram image of the relativistically self-focused filament. Figure 6.4 shows 10-shot average images of the flash for varying plasma peak density and laser energy collected along the pump polarization direction. Such radiation has been observed in prior work, although at a much lower energy and yield ( $\sim 0.1$  nJ for a 500 mJ pump pulse) [238]. Here, neutral density filters were employed to prevent the side-imaged flash intensity from saturating our CCD. We measure flash energies of  $\sim 15$   $\mu$ J into  $f/2.6$  collection optics for the 40 mJ,  $N_e = 3.4 \times 10^{20}$   $\text{cm}^{-3}$  panel in Fig. 6.4, giving  $\sim 1.5$  mJ or  $>3\%$  of the laser energy if the emission is into  $4\pi$  sr.

The axial location, total energy, and spectrum of the horizontally polarized component of the flash are independent of pump polarization, so the flashes do not originate from pump scattering. When the flash is collected perpendicular to the

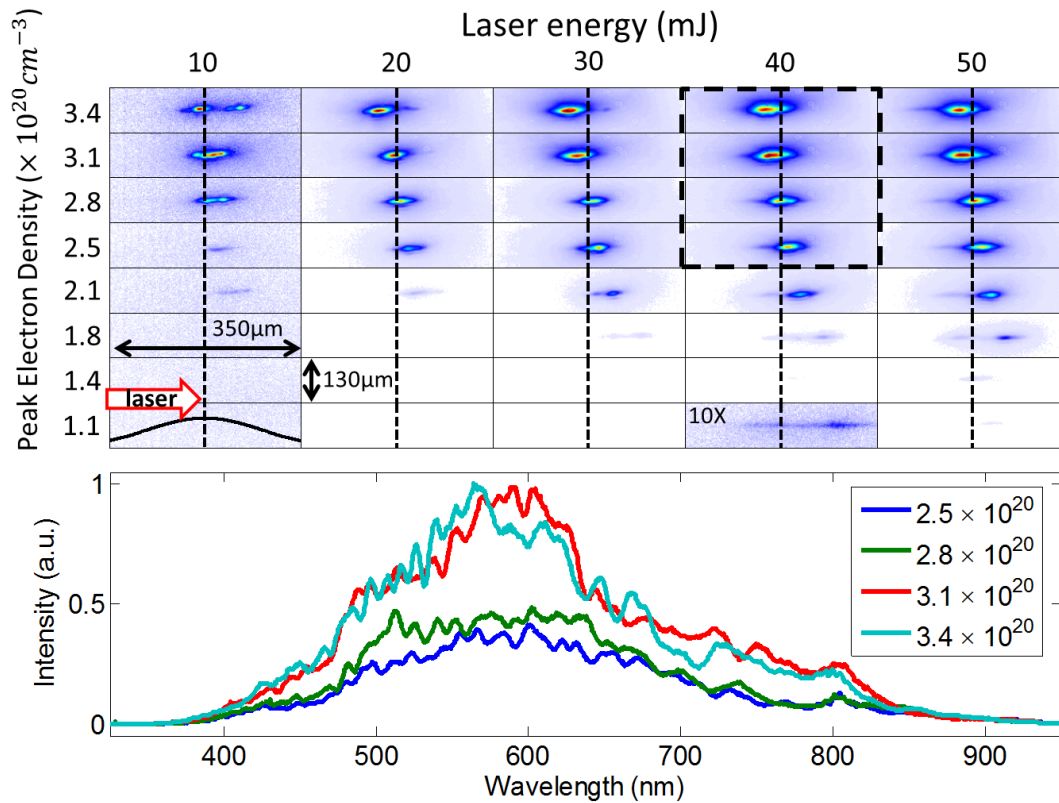


**Figure 6.4.** Top panel: Side images of intense radiation flashes from wave breaking (10 shot averages). The horizontally polarized pump laser pulse propagates left to right. Image intensities are normalized to the maximum intensity within each column. The vertical dashed line is the centre of the gas jet, whose profile is shown in the lower left. The 40 mJ,  $1.1 \times 10^{20} \text{ cm}^{-3}$  image for vertical pump polarization (enhanced 10 $\times$ ), is dominated by 800 nm Thomson scattering on the left and the flash on the right. Bottom panel: Spectra (10 shot averages) of the flash for conditions enclosed by the dashed black box in the top panel.

pump polarization, the vertically polarized component has a small contribution at 800nm, attributed to Thomson scattering, on top of the broadband flash spectrum. Broadband flash spectra (10 shot averages, with no filtering of the pump), peaking at  $\lambda_{rad} \sim 550\text{-}600\text{nm}$  with bandwidth  $\sim 400\text{nm}$ , are shown at the bottom of Fig. 6.4 for pump energy 40 mJ and a range of densities. The figure panels show that the flash occurs on the hydrogen density profile up-ramp for higher densities and laser energies and on the down-ramp for lower densities and laser energies, as also borne out by our

3D simulations. This is explained by the earlier onset of relativistic self-focusing for higher density or laser energy, which is followed closely by self-modulation and wave breaking.

The huge increase in radiation flash energy compared to earlier experiments [238] stems from its coherent emission by electron bunches wave breaking over a spatial scale much smaller than the radiation wavelength and the consequent damping of these bunches by this radiation. As a rough estimate of this effect using 1D approximations, the near-wave breaking crest width  $\Delta x_{crest}$  of the nonlinear plasma wave is given by  $\Delta x_{crest}/\lambda_p \sim \frac{1}{\pi}(\omega/\omega_p)^{3/4}(\Delta p_0/2mc)^{3/4}$  [239], where  $\Delta p_0$  is the electron initial momentum spread. For  $N_e=3 \times 10^{20} \text{ cm}^{-3}$  and  $\Delta p_0/mc \sim 0.06$  (from an initial spread  $\sim (\Delta p_0)^2/2m < 1 \text{ keV}$  from residual electron heating after ionization [240]) we get  $\Delta x_{crest}/\lambda_p \sim 0.04$ , or  $\Delta x_{crest} \sim 0.12\lambda_{rad}$ , significantly shorter than the peak radiated wavelength, ensuring coherent emission. The wave breaking electrons radiate as they execute curved orbits into the wake bucket just ahead of the crest, with emission power  $P \sim n^2 \left( \frac{2e^2}{3m^2c^3} \gamma^2 \left| \frac{d\mathbf{p}}{dt} \right|^2 \right)$  [241] and total radiated energy  $\epsilon_{rad} \sim P\Delta t \sim P\Delta x_{crest} \gamma^{-1}/c$ , where  $n$  is the number of accelerating electrons from the crest,  $d\mathbf{p}/dt$  is the force on an electron, and  $\Delta t$  is the sub-femtosecond time for acceleration off the crest (accounting for Lorentz contraction), or equivalently, the crest lifetime. Taking  $n \sim N_e \lambda_p^3$ ,  $\gamma = \gamma_p = \omega/\omega_p$ , and  $|d\mathbf{p}/dt| \sim eE_{wb}$ , where  $E_{wb} = \sqrt{2}(m\omega_p c/e)(\gamma_p - 1)^{1/2}$  is the 1D wave breaking field [65], gives a total radiated energy of  $\epsilon_{rad} \sim 2 \text{ mJ}$ , which is of the correct order of magnitude.

The strong curving of injected electron orbits by the ion column allows an estimate of the flash spectrum range using the synchrotron radiation critical frequency  $\omega_{rad} \sim \omega_c \sim 3c\gamma^3/2\rho$  [241], where  $\rho$  is the orbit radius of curvature, which we take as  $\rho \sim \lambda_p$ , assuming trapping within a single plasma wave bucket. This gives  $\lambda_c \sim 4\pi/3 (N_e/N_{cr})\lambda_0 \sim 400 - 700 \text{ nm}$  for the density range shown in Fig. 6.4, reasonably overlapping the measured spectra. The synchrotron spectrum bandwidth is estimated as  $(\Delta\lambda/\lambda)_{rad} \sim (\omega_{rad}\Delta t)^{-1} \sim 1$ , in accord with the  $\sim 1$  fs bandwidth in Fig. 6.4 characteristic of half-cycle optical emission, which is consistent with the violent unidirectional electron acceleration upon wave breaking. We note that half-cycle wave breaking radiation at high  $\gamma$  has been proposed as an attosecond x-ray source [242].

To probe its temporal duration and coherence, the flash was interfered in the frequency domain with a supercontinuum pulse, well-characterized in amplitude and phase generated in a Xe gas cell [243,244]. The supercontinuum pulse was compressed in a grism compressor [245], sent through a variable delay line, and directed across the gas jet perpendicular to the pump pulse. The flash and supercontinuum were both collected by an f/4 imaging system and imaged to the entrance slit of an imaging spectrometer at 5X magnification. The entrance slit, oriented perpendicular to the pump laser propagation direction, was used to spatially isolate single flashes. A sample spectral interferogram of the flash and compressed supercontinuum pulse is shown in Fig. 6.5. Fringes across the full supercontinuum bandwidth ( $\sim 250 \text{ nm}$ ) were observed with high visibility, suggesting that the flash is coherent across its full bandwidth.

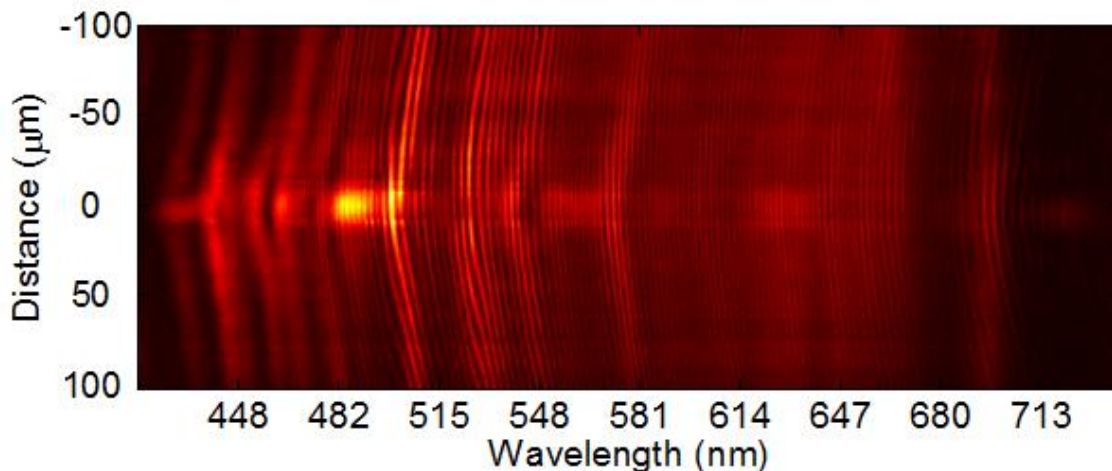


**Figure 6.5.** A sample spectral interferogram between the broadband wave breaking flash and a compressed supercontinuum pulse generated in a Xe gas cell. Fringes are visible across the full 250 nm supercontinuum bandwidth, showing that the broadband flash is spectrally coherent.

Measurement of the flash spectral phase was performed by chirping the supercontinuum pulse and using the stationary phase point method to determine the relative spectral phase between the flash and supercontinuum pulse [246,247]. In the stationary phase point method, a long, chirped pulse is interfered with a much shorter pulse in an imaging spectrometer, and a null in the total spectral phase occurs at the frequency where the arrival time of the two pulses is equal. The total spectral phase can be constructed by changing the delay of the chirped pulse with respect to the short pulse and recording the position of the null. If the spectral phase of the chirped pulse is already well known, then the spectral phase of the short pulse, in this case the flash, can be reconstructed. The extracted flash spectral phase from this technique was consistent with the flash being a nearly transform-limited pulse of  $\sim 1$  fs duration. However, the uncertainty in the measurement of the supercontinuum spectral phase precludes a definitive measurement of the flash temporal pulse shape at this time. Definitive measurement of the flash pulse duration is the subject of ongoing research.



## 6.5 Acceleration mechanism

A question that has arisen in prior experiments and simulations of acceleration at higher plasma densities [27,248,249] is the relative contributions of laser wakefield acceleration (LWFA) and direct laser acceleration (DLA). The contribution of the plasma wave to electron energy gain (in units of  $mc^2$ ) is  $W_z = -\frac{e}{mc^2} \int E_z v_z dt$ , where the integral is over the full electron trajectory and  $E_z$  and  $v_z$  are the longitudinal plasma wakefield and electron velocity. The DLA contribution,  $W_\perp = -\frac{e}{mc^2} \int \mathbf{E}_\perp \cdot \mathbf{v}_\perp dt$ , arises as near light-speed electrons, axially co-propagating with the laser field  $\mathbf{E}_\perp$ , oscillate with a  $\mathbf{v}_\perp$  component about the ion column axis at the betatron frequency  $\omega_\beta = \omega_p / \sqrt{2\gamma}$  or its harmonics, in resonance with the field [248]. In our experiment, the jet location-dependence of electron injection determines the relative contributions of DLA and LWFA to the net energy gain. Early wave breaking injection on the density profile up-ramp occurs when the plasma wavelength is decreasing and more wake buckets lie under the laser pulse envelope, exposing injected electrons to DLA. On the down-ramp, the plasma wavelength is increasing and fewer buckets lie under the laser field envelope, so that injected electrons are less exposed to the laser field. The flash images of Fig. 6.4 are a map of injection locations through the jet, and therefore they spatially map the relative balance of DLA and LWFA, predicting that DLA dominates at high density /high laser energy and LWFA dominates at low density /low laser energy. This transition from LWFA to DLA is corroborated by 2D PIC simulations. Figure 6.6 shows the contributions for a subset of tracked particles accelerated to energies above 1 MeV. For a fixed peak density  $N_e = 0.07N_{cr}$ , the

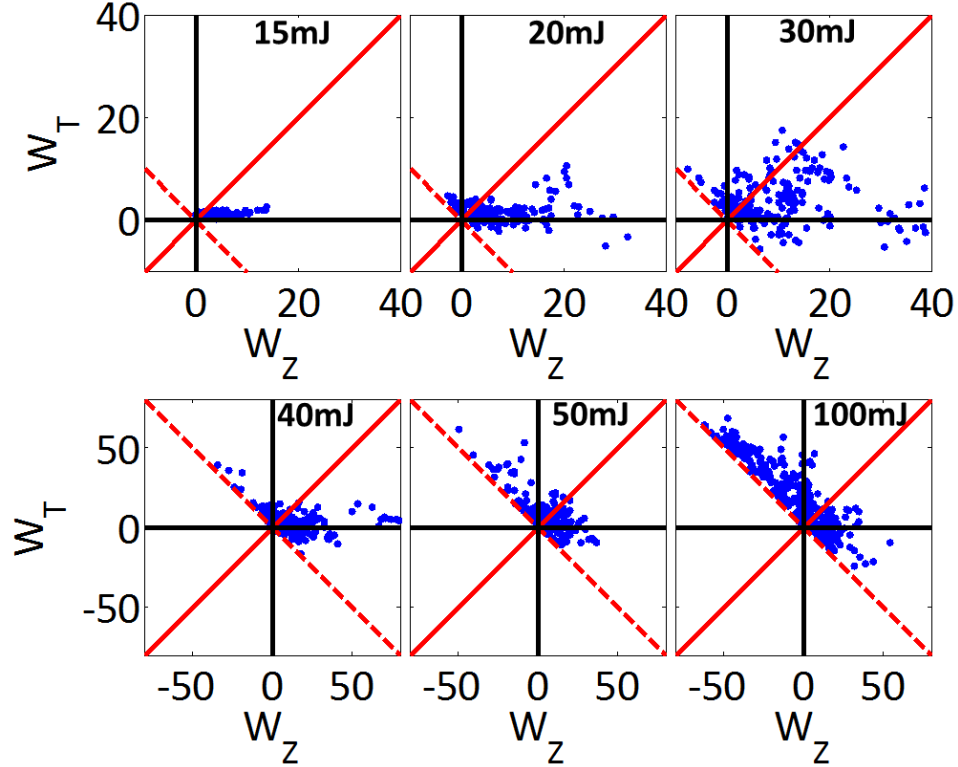


**Figure 6.6.** 2D PIC simulations showing contributions of LWFA and DLA to electron energy gain for a fixed peak plasma density  $N_e = 0.07N_{cr}$  for drive laser energies 15-100mJ. Each blue dot is a tracked electron. Regions above and to the left of the solid red line indicate DLA as the dominant form of acceleration, whereas regions below and to the right are dominated by LWFA. The dashed red diagonal marks zero net energy gain. LWFA dominates acceleration at low drive laser energies, transitioning to DLA at high drive laser energies.

figure panels show clearly that acceleration with low laser energies is dominated by LWFA, transitioning to DLA at energies above  $\sim 50$  mJ.

## 6.6 Summary

In summary, we have demonstrated electron acceleration to the 10 MeV scale with laser pulses well below 1 terawatt, using a thin, high density hydrogen gas jet, with efficiency of laser energy to MeV electrons of a few percent. The high plasma density reduces the thresholds for relativistic self-focusing, nonlinear plasma wave generation, and electron injection. The reduced spatial scales associated with high

density yields intense coherent wave breaking radiation, whose  $\sim 1$  fs bandwidth is consistent with half-cycle optical emission upon violent unidirectional electron acceleration from rest to nearly the speed of light over a subwavelength distance. The flash is of sufficient intensity to self-damp the injected bunch, with the result that wave breaking radiation and acceleration are comparable energy channels. These results open the way to applications of relativistic electron beams with truly compact and portable high repetition rate laser systems.

## Chapter 7: Summary and Future Work

### 7.1 Summary

The purpose of experiments in this dissertation was to advance the state of the art in laser driven electron accelerators, particularly with the goal of reducing the demand on the drive laser energy necessary for acceleration. Plasmas with transverse and longitudinal structure on the sub-millimeter scale were used to accomplish this goal. In Chapter 3, experiments were presented that studied guiding and electron acceleration in plasma waveguides produced by hydrodynamic motion of a hot plasma formed in a clustered gas jet. Guiding of low intensity pulses at efficiencies up to 80% with  $\sim 14 \mu\text{m}$  spot sizes was demonstrated over  $\sim 1 \text{ cm}$  long channels. At higher intensities ( $P > P_{cr}$ ) the energy throughput and mode quality deteriorated due to relativistic effects within the channel, and plasma wave generation was inferred from spectral measurements of the guided beam. The guiding structure was then shown to stabilize the pointing of wakefield accelerated electron beams produced in  $\sim 1.5 \text{ mm}$  long  $\text{N}^{5+}$  channels. Particle-in-cell simulations were performed confirming that injection into wakes driven in He-like nitrogen plasma channels was due to tunnel-ionization of inner-shell electrons near the peak of the drive laser pulse.

Quasi-phase-matched direct acceleration (QPM-DLA) of electrons in a corrugated plasma channel was described in Chapter 4. A simple method for making a femtosecond laser pulse with a longitudinal field component capable of driving the QPM-DLA scheme was presented. Further, guiding of the higher order Hermite-

Gaussian mode in a plasma channel, vital for a proof of principle QPM-DLA scheme, was demonstrated over lengths up to 11 mm.

The QPM-DLA technique can accelerate electrons with a high gradient using a low energy, high repetition rate drive laser. However, the scheme requires a source of relativistic seed electrons. The seed source has been the limiting constraint to a proof of concept QPM-DLA experiment. Chapter 6 presented an experiment in which a high energy ( $>5$  MeV) and high charge ( $\sim 100$  pC) electron beam was generated from the interaction of a sub-terawatt laser pulse with a high density ( $>10^{20}$   $\text{cm}^{-3}$ ) plasma. The electron beams observed in this experiment, interesting in their own right for electron radiography or bremsstrahlung x-ray generation experiments, could be an excellent seed source for a QPM-DLA proof of concept. The high density jet, characterized in Chapter 5, was capable of reaching the critical density for our Ti:Sapphire laser ( $N_{cr} \approx 1.7 \times 10^{21} \text{cm}^{-3}$ ) while still maintaining a thin ( $\sim 200$   $\mu\text{m}$ ) density profile. The electron acceleration results made use of relativistic self-focusing and self-modulation of the  $< 50$  mJ, 50 fs laser pulse to drive a plasma wave in the thin jet to the point of wave breaking. Coherent radiation of the electrons as they were accelerated from rest to nearly the speed of light was detected as a bright, extremely broadband “flash” radiating  $\sim 1\%$  of the drive laser energy.

## **7.2 Future Work**

### **7.2.1 Plasma channel guiding experiments**

The wakefield accelerator presented in Chapter 3 was demonstrated at relatively high density ( $\sim 1.4 \times 10^{19} \text{cm}^{-3}$ ) over a relatively short interaction length

(~1.5 mm). Scaling laws presented in Chapter 1 of the maximum electron energy available from wakefield accelerators suggest that higher energy electron beams can be produced in longer, lower density plasmas because of the increased dephasing length at lower density. While guiding was demonstrated at relativistic intensity in ~1 cm channels, no experiments as yet have been performed looking for high energy electron beams in these experiments. However, 2D TurboWave PIC simulations suggest that ionization injection and subsequent acceleration in a channel with a density profile similar to that presented in Fig. 3.6 can accelerate electrons up to ~0.5 GeV using a drive pulse of only ~6 TW peak power.

## **7.2.2 Quasi-phase-matched direct laser acceleration**

Many of the experiments presented in this dissertation were performed in advance of a proof of concept demonstration of the QPM-DLA technique [12]. The three components necessary for this demonstration, a modulated waveguide, radially polarized drive pulse, and electron seed source, have all been demonstrated in this dissertation. Modulated plasma waveguide generation and guiding of quasi-radially polarized laser pulses were shown in Chapter 4. Modulation techniques outlined in Chapter 4 involving ring gratings [173] or wire modulated cluster jets [152,155], however, produce static modulation profiles. Real time optimization of the QPM-DLA process would benefit from a dynamic modulation technique. The use of a spatial light modulator to shape the intensity profile of the channel-forming pulse can produce computer controlled axial modulations, allowing dynamic control of the modulation depth and period during an experiment.

A proof of concept QPM-DLA experiment will require the radially polarized pulse, modulated waveguide, and seed source to be produced and diagnosed concurrently. While this presents no major technical hurdles, the geometry and diagnostics necessary to adequately diagnose each component of the experiment should be carefully considered. Use of the electron beams presented in Chapter 6 as a seed source must be carefully considered so that estimates can be made of the expected accelerated charge which is necessary for proper detector design. For instance, the relatively large divergence of the beams presented in Chapter 6 could be a problem given the small acceptance angle of a  $\sim 1$  cm long,  $\sim 100$   $\mu\text{m}$  diameter plasma waveguide. If the electron beam divergence requires a small separation between the electron beam seed source and the modulated plasma waveguide, injection of the radially polarized pulse into the modulated channel could be geometrically difficult.

### **7.2.3 High density laser-plasma interaction experiments**

The gas jet characterized in Chapter 5 and the experiments performed in Chapter 6 open up a number of interesting avenues for further research. First, the low drive pulse energy ( $\sim 10$  mJ) used to generate the multi-MeV electron beams suggests extension of the technique to kHz repetition rate laser systems. A higher repetition rate pulsed jet or, more likely, a continuous flow high density target will be necessary for experiments using a kHz drive laser. If kHz operation can be achieved, ultrafast high-repetition rate radiography or MeV electron diffraction experiments could be performed driven by a relatively compact laser system. Further reduction of the required pulse energy for electron injection, possibly to the few mJ range, may also

be achieved through ionization injection. Electron beams were only observed at power levels  $\sim 3P_{cr}$  because the plasma wave amplitude needed to reach the wave breaking threshold for electron injection into the wakefield. As demonstrated by experiments in Chapter 3, ionization injection can reduce the required drive laser power for electron acceleration.

In addition to the prospects of a high repetition rate MeV electron source, the experiments in Chapter 6 open the way to further experimentation with the physics of laser-plasma interaction at near critical densities. The bright wave breaking radiation flashes observed from the high density laser-plasma interaction were shown to be coherent through spectral interferometry experiments. However, error bars on the extracted flash spectral phase precluded the precise determination of the flash pulse duration. The mechanism suggested for the coherent flash emission, namely the violent unipolar acceleration of electrons at wave breaking, suggests that the flash is actually generated as a half-cycle optical pulse. Further experiments are currently being performed in an attempt to more precisely measure the flash pulse duration. Simulations of the interaction of a tightly focused, multi-TW pulse with our high density jet also suggest that ions within the plasma can be accelerated to high energy under certain conditions. Proton acceleration to multi-MeV energies at relatively high repetition rates ( $\geq 10$  Hz) from a gas jet target could open the way to applications such as on-demand production of short half-life radioisotopes used in nuclear medicine.



## Bibliography

- [1] T. P. Wangler, *RF Linear Accelerators*, 2nd ed (Wiley-VHC, 2008).
- [2] A. Grudiev, S. Calatroni, and W. Wuensch, *Phys. Rev. Spec. Top. - Accel. Beams* **12**, 102001 (2009).
- [3] R. W. Hamme and M. E. Hamme, *Industrial Accelerators an Their Applications* (World Scientrific, 2012).
- [4] V. Malka, J. Faure, Y. A. Gauduel, E. Lefebvre, A. Rousse, and K. T. Phuoc, *Nat. Phys.* **4**, 447 (2008).
- [5] E. Esarey, C. B. Schroeder, and W. P. Leemans, *Rev. Mod. Phys.* **81**, 1229 (2009).
- [6] H. Daido, M. Nishiuchi, and A. S. Pirozhkov, *Rep. Prog. Phys.* **75**, 056401 (2012).
- [7] P. Maine, D. Strickland, P. Bado, M. Pessot, and G. Mourou, *IEEE J. Quantum Electron.* **24**, 398 (1988).
- [8] D. Strickland and G. Mourou, *Opt. Commun.* **55**, 447 (1985).
- [9] W. R. Rapoport and C. P. Khattak, *Appl. Opt.* **27**, 2677 (1988).
- [10] K. Wall and A. Sanchez, *Lincoln Lab. J.* **3**, 447 (1990).
- [11] S. W. Bahk, P. Rousseau, T. A. Planchon, V. Chvykov, G. Kalintchenko, A. Maksimchuk, G. A. Mourou, and V. Yanovsky, *Opt. Lett.* **29**, 2837 (2004).
- [12] A. York, H. Milchberg, J. Palastro, and T. Antonsen, *Phys. Rev. Lett.* **100**, 195001 (2008).
- [13] C. Varin, S. Payeur, V. Marceau, S. Fourmaux, A. April, B. Schmidt, P.-L. Fortin, N. Thiré, T. Brabec, F. Légaré, J.-C. Kieffer, and M. Piché, *Appl. Sci.* **3**, 70 (2013).

- [14] R. J. England, R. J. Noble, K. Bane, D. Dowell, C. Ng, J. E. Spencer, S. Tantawi, Z. Wu, R. L. Byer, E. Peralta, K. Soong, C.-M. Chang, B. Montazeri, S. J. Wolf, B. Cowan, J. Dawson, W. Gai, P. Hommelhoff, Y.-C. Huang, C. Jing, C. McGuinness, R. B. Palmer, B. Naranjo, J. Rosenzweig, G. Travish, A. Mizrahi, L. Schachter, C. Sears, G. R. Werner, and R. B. Yoder, *Rev. Mod. Phys.* **86**, 1337 (2014).
- [15] W. D. Kimura, G. H. Kim, R. D. Romea, L. C. Steinhauer, I. V. Pogorelsky, K. P. Kusche, R. C. Fernow, X. Wang, and Y. Liu, *Phys. Rev. Lett.* **74**, 546 (1995).
- [16] B. Hafizi, E. Esarey, and P. Sprangle, *Phys. Rev. E* **55**, 3539 (1997).
- [17] T. Tajima and J. Dawson, *Phys. Rev. Lett.* **43**, 267 (1979).
- [18] P. Sprangle, E. Esarey, A. Ting, and G. Joyce, *Appl. Phys. Lett.* **53**, 2146 (1988).
- [19] S. Corde, K. Ta Phuoc, G. Lambert, R. Fitour, V. Malka, A. Rousse, A. Beck, and E. Lefebvre, *Rev. Mod. Phys.* **85**, 1 (2013).
- [20] J. Faure, C. Rechatin, A. Norlin, A. Lifschitz, Y. Glinec, and V. Malka, *Nature* **444**, 737 (2006).
- [21] A. J. Gonsalves, K. Nakamura, C. Lin, D. Panasencko, S. Shiraishi, T. Sokollik, C. Benedetti, C. B. Schroeder, C. G. R. Geddes, J. van Tilborg, J. Osterhoff, E. Esarey, C. Toth, and W. P. Leemans, *Nat. Phys.* **7**, 862 (2011).
- [22] B. S. Rao, A. Moorti, R. Rathore, J. A. Chakera, P. A. Naik, and P. D. Gupta, *Phys. Rev. Spec. Top. - Accel. Beams* **17**, 011301 (2014).
- [23] J. Osterhoff, A. Popp, Z. Major, B. Marx, T. P. Rowlands-Rees, M. Fuchs, M. Geissler, R. Hörlein, B. Hidding, S. Becker, E. A. Peralta, U. Schramm, F. Grüner, D. Habs, F. Krausz, S. M. Hooker, and S. Karsch, *Phys. Rev. Lett.* **101**, 085002 (2008).
- [24] A. Modena, Z. Najmudin, A. E. Dangor, C. E. Clayton, K. A. Marsh, C. Joshi, V. Malka, C. B. Darrow, C. Danson, D. Neely, and F. N. Walsh, *Nature* **377**,

606 (1995).

- [25] K. Nakajima, D. Fisher, T. Kawakubo, H. Nakanishi, A. Ogata, Y. Kato, Y. Kitagawa, R. Kodama, K. Mima, H. Shiraga, K. Suzuki, K. Yamakawa, T. Zhang, Y. Sakawa, T. Shoji, Y. Nishida, N. Yugami, M. Downer, and T. Tajima, *Phys. Rev. Lett.* **74**, 4428 (1995).
- [26] A. Ting, C. I. Moore, K. Krushelnick, C. Manka, E. Esarey, P. Sprangle, R. Hubbard, H. R. Burris, R. Fischer, and M. Baine, *Phys. Plasmas* **4**, 1889 (1997).
- [27] C. Gahn, G. Tsakiris, A. Pukhov, J. Meyer-ter-Vehn, G. Pretzler, P. Thirolf, D. Habs, and K. Witte, *Phys. Rev. Lett.* **83**, 4772 (1999).
- [28] J. Faure, Y. Glinec, A. Pukhov, S. Kiselev, S. Gordienko, E. Lefebvre, J.-P. Rousseau, F. Burgy, and V. Malka, *Nature* **431**, 541 (2004).
- [29] C. G. R. Geddes, C. Toth, J. van Tilborg, E. Esarey, C. B. Schroeder, D. Bruhwiler, C. Nieter, J. Cary, and W. P. Leemans, *Nature* **431**, 538 (2004).
- [30] S. P. D. Mangles, C. D. Murphy, Z. Najmudin, A. G. R. Thomas, J. L. Collier, A. E. Dangor, E. J. Divall, P. S. Foster, J. G. Gallacher, C. J. Hooker, D. A. Jaroszynski, A. J. Langley, W. B. Mori, P. A. Norreys, F. S. Tsung, R. Viskup, B. R. Walton, and K. Krushelnick, *Nature* **431**, 535 (2004).
- [31] W. P. Leemans, A. J. Gonsalves, H.-S. Mao, K. Nakamura, C. Benedetti, C. B. Schroeder, C. Tóth, J. Daniels, D. E. Mittelberger, S. S. Bulanov, J.-L. Vay, C. G. R. Geddes, and E. Esarey, *Phys. Rev. Lett.* **113**, 245002 (2014).
- [32] X. L. Xu, Y. P. Wu, C. J. Zhang, F. Li, Y. Wan, J. F. Hua, C.-H. Pai, W. Lu, P. Yu, C. Joshi, and W. B. Mori, *Phys. Rev. Spec. Top. - Accel. Beams* **17**, 061301 (2014).
- [33] C. B. Schroeder, E. Esarey, C. Benedetti, and W. P. Leemans, *Phys. Plasmas* **20**, 080701 (2013).
- [34] C. G. R. Geddes, K. Nakamura, G. R. Plateau, C. Toth, E. Cormier-Michel, E. Esarey, C. B. Schroeder, J. R. Cary, and W. P. Leemans, *Phys. Rev. Lett.* **100**, 215004 (2008).

- [35] A. Rousse, K. Ta Phuoc, R. Shah, A. Pukhov, E. Lefebvre, V. Malka, S. Kiselev, F. Burgy, J. P. Rousseau, D. Umstadter, and D. Hulin, *Phys. Rev. Lett.* **93**, 135005 (2004).
- [36] K. T. Phuoc, S. Corde, R. Shah, F. Albert, R. Fitour, J.-P. Rousseau, F. Burgy, B. Mercier, and A. Rousse, *Phys. Rev. Lett.* **97**, 225002 (2006).
- [37] S. Kneip, S. R. Nagel, C. Bellei, N. Bourgeois, A. E. Dangor, A. Gopal, R. Heathcote, S. P. D. Mangles, J. R. Marquès, A. Maksimchuk, P. M. Nilson, K. T. Phuoc, S. Reed, M. Tzoufras, F. S. Tsung, L. Willingale, W. B. Mori, A. Rousse, K. Krushelnick, and Z. Najmudin, *Phys. Rev. Lett.* **100**, 105006 (2008).
- [38] H.-P. Schlenvoigt, K. Haupt, A. Debus, F. Budde, O. Jäckel, S. Pfotenhauer, H. Schworer, E. Rohwer, J. G. Gallacher, E. Brunetti, R. P. Shanks, S. M. Wiggins, and D. A. Jaroszynski, *Nat. Phys.* **4**, 130 (2008).
- [39] G. Sarri, D. J. Corvan, W. Schumaker, J. M. Cole, A. Di Piazza, H. Ahmed, C. Harvey, C. H. Keitel, K. Krushelnick, S. P. D. Mangles, Z. Najmudin, D. Symes, A. G. R. Thomas, M. Yeung, Z. Zhao, and M. Zepf, *Phys. Rev. Lett.* **113**, 224801 (2014).
- [40] K. Khrennikov, J. Wenz, A. Buck, J. Xu, M. Heigoldt, L. Veisz, and S. Karsch, *Phys. Rev. Lett.* **114**, 1 (2015).
- [41] S. Kneip, C. McGuffey, J. L. Martins, S. F. Martins, C. Bellei, V. Chvykov, F. Dollar, R. Fonseca, C. Huntington, G. Kalintchenko, A. Maksimchuk, S. P. D. Mangles, T. Matsuoka, S. R. Nagel, C. A. J. Palmer, J. Schreiber, K. Ta Phuoc, A. G. R. Thomas, V. Yanovsky, L. O. Silva, K. Krushelnick, and Z. Najmudin, *Nat. Phys.* **6**, 980 (2010).
- [42] G. J. Williams, B. B. Pollock, F. Albert, J. Park, and H. Chen, *Phys. Plasmas* **22**, 093115 (2015).
- [43] G. Sarri, W. Schumaker, A. Di Piazza, M. Vargas, B. Dromey, M. E. Dieckmann, V. Chvykov, A. Maksimchuk, V. Yanovsky, Z. H. He, B. X. Hou, J. A. Nees, A. G. R. Thomas, C. H. Keitel, M. Zepf, and K. Krushelnick, *Phys. Rev. Lett.* **110**, 255002 (2013).

- [44] A. Di Piazza, C. Müller, K. Z. Hatsagortsyan, and C. H. Keitel, *Rev. Mod. Phys.* **84**, 1177 (2012).
- [45] E. Esarey, P. Sprangle, J. Krall, and A. Ting, *IEEE Trans. Plasma Sci.* **24**, (1996).
- [46] P. Sprangle, E. Esarey, and A. Ting, *Phys. Rev. Lett.* **64**, 2011 (1990).
- [47] A. Ting, E. Esarey, and P. Sprangle, *Phys. Fluids B Plasma Phys.* **2**, 1390 (1990).
- [48] P. Sprangle, E. Esarey, and A. Ting, *Phys. Rev. A* **41**, 4463 (1990).
- [49] E. Esarey, P. Sprangle, J. Krall, A. Ting, and G. Joyce, *Phys. Fluids B Plasma Phys.* **5**, 2690 (1993).
- [50] D. Teychenné, G. Bonnaud, and J. Bobin, *Phys. Rev. E* **48**, 3248 (1993).
- [51] C. E. Max, J. Aronst, and A. B. Langdon, *Phys. Rev. Lett.* **33**, 209 (1974).
- [52] P. Sprangle, C.-M. Tang, and E. Esarey, *IEEE Trans. Plasma Sci.* **15**, 145 (1987).
- [53] P. Sprangle, E. Esarey, J. Krall, and G. Joyce, *Phys. Rev. Lett.* **69**, 2200 (1992).
- [54] C. K. Birdsall and A. B. Langdon, *Plasma Physics via Computer Simulation* (Taylor & Francis Group, 2005).
- [55] J. P. Verboncoeur, *Plasma Phys. Control. Fusion* **47**, A231 (2005).
- [56] C. Moore, A. Ting, K. Krushelnick, E. Esarey, R. Hubbard, B. Hafizi, H. Burris, C. Manka, and P. Sprangle, *Phys. Rev. Lett.* **79**, 3909 (1997).
- [57] S. Le Blanc, M. Downer, R. Wagner, S.-Y. Chen, A. Maksimchuk, G. Mourou, and D. Umstadter, *Phys. Rev. Lett.* **77**, 5381 (1996).

- [58] R. Wagner, S.-Y. Chen, A. Maksimchuk, and D. Umstadter, *Phys. Rev. Lett.* **78**, 3125 (1997).
- [59] A. Ting, K. Krushelnick, C. Moore, H. Burris, E. Esarey, J. Krall, and P. Sprangle, *Phys. Rev. Lett.* **77**, 5377 (1996).
- [60] C. G. Durfee and H. M. Milchberg, *Phys. Rev. Lett.* **71**, 2409 (1993).
- [61] T. Clark and H. Milchberg, *Phys. Rev. E* **61**, 1954 (2000).
- [62] C. B. Schroeder, E. Esarey, B. A. Shadwick, and W. P. Leemans, *Phys. Plasmas* **13**, 033103 (2006).
- [63] D. Gordon, K. C. Tzeng, C. E. Clayton, A. E. Dangor, V. Malka, K. A. Marsh, A. Modena, W. B. Mori, P. Muggli, Z. Najmudin, D. Neely, C. Danson, and C. Joshi, *Phys. Rev. Lett.* **80**, 2133 (1998).
- [64] S. Bulanov, N. Naumova, F. Pegoraro, and J. Sakai, *Phys. Rev. E* **58**, R5257 (1998).
- [65] S. V. Bulanov, F. Pegoraro, A. M. Pukhov, and A. S. Sakharov, *Phys. Rev. Lett.* **78**, 4205 (1997).
- [66] E. Esarey, R. F. Hubbard, W. P. Leemans, A. Ting, and P. Sprangle, *Phys. Rev. Lett.* **79**, 2682 (1997).
- [67] D. Umstadter, J. Kim, and E. Dodd, *Phys. Rev. Lett.* **76**, 2073 (1996).
- [68] G. Golovin, S. Chen, N. D. Powers, C. Liu, S. Banerjee, J. Zhang, M. Zeng, Z. Sheng, and D. Umstadter, *Phys. Rev. Spec. Top. - Accel. Beams* **18**, 011301 (2015).
- [69] M. Chen, E. Esarey, C. G. R. Geddes, E. Cormier-Michel, C. B. Schroeder, S. S. Bulanov, C. Benedetti, L. L. Yu, S. Rykovanov, D. L. Bruhwiler, and W. P. Leemans, *Phys. Rev. Spec. Top. - Accel. Beams* **17**, 051303 (2014).
- [70] A. Pak, K. A. Marsh, S. F. Martins, W. Lu, W. B. Mori, and C. Joshi, *Phys. Rev. Lett.* **104**, 025003 (2010).

- [71] E. Oz, S. Deng, T. Katsouleas, P. Muggli, C. D. Barnes, I. Blumenfeld, F. J. Decker, P. Emma, M. J. Hogan, R. Ischebeck, R. H. Iversen, N. Kirby, P. Krejcik, C. O'Connell, R. H. Siemann, D. Walz, D. Auerbach, C. E. Clayton, C. Huang, D. K. Johnson, C. Joshi, W. Lu, K. A. Marsh, W. B. Mori, and M. Zhou, *Phys. Rev. Lett.* **98**, 084801 (2007).
- [72] T. P. Rowlands-Rees, C. Kamperidis, S. Kneip, A. J. Gonsalves, S. P. D. Mangles, J. G. Gallacher, E. Brunetti, T. Ibbotson, C. D. Murphy, P. S. Foster, M. J. V. Streeter, F. Budde, P. A. Norreys, D. A. Jaroszynski, K. Krushelnick, Z. Najmudin, and S. M. Hooker, *Phys. Rev. Lett.* **100**, 105005 (2008).
- [73] C. McGuffey, A. G. R. Thomas, W. Schumaker, T. Matsuoka, V. Chvykov, F. J. Dollar, G. Kalintchenko, V. Yanovsky, A. Maksimchuk, K. Krushelnick, V. Y. Bychenkov, I. V. Glazyrin, and A. V. Karpeev, *Phys. Rev. Lett.* **104**, 025004 (2010).
- [74] Y.-C. Ho, T.-S. Hung, C.-P. Yen, S.-Y. Chen, H.-H. Chu, J.-Y. Lin, J. Wang, and M.-C. Chou, *Phys. Plasmas* **18**, 063102 (2011).
- [75] A. J. Goers, S. J. Yoon, J. A. Elle, G. A. Hine, and H. M. Milchberg, *Appl. Phys. Lett.* **104**, 214105 (2014).
- [76] N. Bourgeois, J. Cowley, and S. M. Hooker, *Phys. Rev. Lett.* **111**, 155004 (2013).
- [77] R. R. Hubbard, P. Sprangle, and B. Hafizi, *IEEE Trans. Plasma Sci.* **28**, 1159 (2000).
- [78] P. Sprangle, B. Hafizi, J. Penano, R. F. Hubbard, A. Ting, A. Zigler, and T. M. Antonsen, *Phys. Rev. Lett.* **85**, 5110 (2000).
- [79] S. J. Yoon, J. P. Palastro, and H. M. Milchberg, *Phys. Rev. Lett.* **112**, 134803 (2014).
- [80] W. Lu, M. Tzoufras, C. Joshi, F. S. Tsung, W. B. Mori, J. Vieira, R. A. Fonseca, and L. O. Silva, *Phys. Rev. Spec. Top. - Accel. Beams* **10**, 061301 (2007).

- [81] P. Serafim, P. Sprangle, and B. Hafizi, *IEEE Trans. Plasma Sci.* **28**, 1155 (2000).
- [82] T. Plettner, R. L. Byer, E. Colby, B. Cowan, C. M. S. Sears, J. E. Spencer, and R. H. Siemann, *Phys. Rev. Lett.* **95**, 134801 (2005).
- [83] E. Esarey, P. Sprangle, and J. Krall, *Phys. Rev. E* **52**, 5443 (1995).
- [84] J. P. Palastro, T. M. Antonsen, S. Morshed, A. G. York, and H. M. Milchberg, *Phys. Rev. E* **77**, 036405 (2008).
- [85] S. Yoon, J. Palastro, D. Gordon, T. Antonsen, and H. Milchberg, *Phys. Rev. Spec. Top. - Accel. Beams* **15**, 081305 (2012).
- [86] G. Mourou, T. Tajima, and S. Bulanov, *Rev. Mod. Phys.* **78**, 309 (2006).
- [87] S. Backus, C. G. Durfee, M. M. Murnane, and H. C. Kapteyn, *Rev. Sci. Instrum.* **69**, 1207 (1998).
- [88] U. Morgner, F. X. Kärtner, S. H. Cho, Y. Chen, H. A. Haus, J. G. Fujimoto, E. P. Ippen, V. Scheuer, G. Angelow, and T. Tschudi, *Opt. Lett.* **24**, 411 (1999).
- [89] D. H. Sutter, G. Steinmeyer, L. Gallmann, N. Matuschek, F. Morier-Genoud, U. Keller, V. Scheuer, G. Angelow, and T. Tschudi, *Opt. Lett.* **24**, 631 (1999).
- [90] W. Koechner, *Solid State Laser Engineering*, 6th ed. (Springer-Verlag New York, 2006).
- [91] A. Siegman, *Lasers* (University Science Books, 1986).
- [92] J. Zhou, C.-P. Huang, M. M. Murnane, and H. C. Kapteyn, *Opt. Lett.* **20**, 64 (1995).
- [93] C. Le Blanc, P. Curley, and F. Salin, *Opt. Commun.* **131**, 391 (1996).
- [94] C. P. Barty, C. L. Gordon, and B. E. Lemoff, *Opt. Lett.* **19**, 1442 (1994).



- [95] P. Poole, S. Trendafilov, G. Shvets, D. Smith, and E. Chowdhury, *Opt. Express* **21**, 26341 (2013).
- [96] E. Treacy, *IEEE J. Quantum Electron.* **5**, 454 (1969).
- [97] B. E. Lemoff and C. P. Barty, *Opt. Lett.* **18**, 1651 (1993).
- [98] S. Kane and J. Squier, *J. Opt. Soc. Am. B* **14**, 1237 (1997).
- [99] R. Trebino and D. J. Kane, *J. Opt. Soc. Am. A* **10**, 1101 (1993).
- [100] C. Iaconis and I. A. Walmsley, *Opt. Lett.* **23**, 792 (1998).
- [101] C. Rulliere, *Femtosecond Laser Pulses: Principles and Experiments*, 2nd ed. (Springer, 2005).
- [102] R. Trebino, *Frequency-Resolved Optical Gating* (Kluwer Academic Publishers, 2000).
- [103] Femtosoft QuickFROG, [www.femtosoft.com](http://www.femtosoft.com)
- [104] A. M. Weiner, *Opt. Commun.* **284**, 3669 (2011).
- [105] A. M. Weiner, *Rev. Sci. Instrum.* **71**, 1929 (2000).
- [106] F. Verluise, V. Laude, Z. Cheng, C. Spielmann, and P. Tournois, *Opt. Lett.* **25**, 575 (2000).
- [107] [www.fastlite.com](http://www.fastlite.com)
- [108] P. Tournois, *Opt. Commun.* **140**, 245 (1997).
- [109] D. Kaplan and P. Tournois, *J. Phys. IV* **12**, 69 (2002).
- [110] J. Seres, A. Müller, E. Seres, K. O’Keeffe, M. Lenner, R. F. Herzog, D. Kaplan, C. Spielmann, and F. Krausz, *Opt. Lett.* **28**, 1832 (2003).

- [111] [www.ultrafast-innovations.com](http://www.ultrafast-innovations.com)
- [112] D. Kaganovich, J. R. Peñano, M. H. Helle, D. F. Gordon, B. Hafizi, and A. Ting, *Opt. Lett.* **38**, 3635 (2013).
- [113] M. Hart, *Appl. Opt.* **49**, D17 (2010).
- [114] R. Zhi-Jun, L. Xiao-Yan, M.-B. Lie, C.-Q. Xia, X.-M. Lu, R.-X. Li, and Z.-Z. Xu, *Chinese Phys. Lett.* **26**, 124203 (2009).
- [115] F. Canova, A. Flacco, L. Canova, R. Clady, J.-P. Chambaret, F. Ple, M. Pittman, T. A. Planchon, M. Silva, R. Benocci, G. Lucchini, D. Batani, E. Lavergne, G. Dovillaire, and X. Levecq, *Laser Part. Beams* **25**, 649 (2007).
- [116] S.-W. Bahk, P. Rousseau, T. A. Planchon, V. Chvykov, G. Kalintchenko, A. Maksimchuk, G. A. Mourou, and V. Yanovsky, *Appl. Phys. B* **80**, 823 (2005).
- [117] Z.-H. He, B. Hou, V. Lebailly, J. A. Nees, K. Krushelnick, and A. G. R. Thomas, *Nat. Commun.* **6**, 7156 (2015).
- [118] T. Bifano, *Nat. Photonics* **5**, 21 (2011).
- [119] S. Serati and J. Stockley, *Proc. SPIE* **5894**, 58940K (2005).
- [120] E. Steinhaus and S. G. Lipson, *J. Opt. Soc. Am.* **69**, 478 (1979).
- [121] J.-C. Chanteloup, *Appl. Opt.* **44**, 1559 (2005).
- [122] J. Primot and L. Sogno, *J. Opt. Soc. Am. A* **12**, 2679 (1995).
- [123] K. Osvay, A. P. Kovács, G. Kurdi, Z. Heiner, M. Divall, J. Klebniczki, and I. E. Ferincz, *Opt. Commun.* **248**, 201 (2005).
- [124] G. Pretzler, A. Kasper, and K. J. Witte, *Appl. Phys. B Lasers Opt.* **70**, 1 (2000).

- [125] M. Trentelman, I. N. Ross, and C. N. Danson, *Appl. Opt.* **36**, 8567 (1997).
- [126] C. Fiorini, C. Sauteret, C. Rouyer, N. Blanchot, S. Seznec, and A. Migus, *IEEE J. Quantum Electron.* **30**, 1662 (1994).
- [127] R. Kammel, R. Ackermann, J. Thomas, J. Götte, S. Skupin, A. Tünnermann, and S. Nolte, *Light Sci. Appl.* **3**, e169 (2014).
- [128] D. N. Vitek, D. E. Adams, A. Johnson, P. S. Tsai, S. Backus, C. G. Durfee, D. Kleinfeld, and J. A. Squier, *Opt. Express* **18**, 18086 (2010).
- [129] E. Block, M. Greco, D. Vitek, O. Masihzadeh, D. A. Ammar, M. Y. Kahook, N. Mandava, C. Durfee, and J. Squier, *Biomed. Opt. Express* **4**, 831 (2013).
- [130] P. G. Gobbi and G. C. Reali, *Opt. Commun.* **52**, 195 (1984).
- [131] Thomas Clark, *Hydrodynamical and Optical Properties of the Plasma Waveguide*. PhD thesis, University of Maryland, College Park, 1998.
- [132] H. Milchberg and T. Clark, *Phys. Plasmas* **3**, 2149 (1996).
- [133] A. Depresseux, E. Oliva, J. Gautier, F. Tissandier, G. Lambert, B. Vodungbo, J.-P. Goddet, A. Tafzi, J. Nejdil, M. Kozlova, G. Maynard, H. T. Kim, K. T. Phuoc, A. Rousse, P. Zeitoun, and S. Sebban, *Phys. Rev. Lett.* **115**, 083901 (2015).
- [134] H. Milchberg, C. Durfee, and J. Lynch, *JOSA B* **12**, 731 (1995).
- [135] T. M. Antonsen, J. Palastro, and H. M. Milchberg, *Phys. Plasmas* **14**, 033107 (2007).
- [136] Lord Rayleigh, *Philos. Mag.* **43**, 125 (1897).
- [137] A. G. Litvak, *Sov. Phys. JETP* **30**, 344 (1970).
- [138] K. Krushelnick, A. Ting, C. Moore, H. Burris, E. Esarey, P. Sprangle, and M. Baine, *Phys. Rev. Lett.* **78**, 4047 (1997).

- [139] P. Monot, T. Auguste, P. Gibbon, F. Jakober, G. Mainfray, A. Dulieu, M. Louis-Jacquet, G. Malka, and J. Miquel, *Phys. Rev. Lett.* **74**, 2953 (1995).
- [140] W. P. Leemans, B. Nagler, A. J. Gonsalves, C. Tóth, K. Nakamura, C. G. R. Geddes, E. Esarey, C. B. Schroeder, and S. M. Hooker, *Nat. Phys.* **2**, 696 (2006).
- [141] S. P. Nikitin, T. M. Antonsen, T. R. Clark, Y. Li, and H. M. Milchberg, *Opt. Lett.* **22**, 1787 (1997).
- [142] S. Nikitin, I. Alexeev, J. Fan, and H. Milchberg, *Phys. Rev. E* **59**, R3839 (1999).
- [143] P. Volfbeyn, E. Esarey, and W. P. Leemans, *Phys. Plasmas* **6**, 2269 (1999).
- [144] C. Geddes, C. Toth, J. van Tilborg, E. Esarey, C. Schroeder, J. Cary, and W. Leemans, *Phys. Rev. Lett.* **95**, 145002 (2005).
- [145] A. Zigler, Y. Ehrlich, C. Cohen, J. Krall, and P. Sprangle, *J. Opt. Soc. Am. B* **13**, 68 (1996).
- [146] D. Spence and S. Hooker, *Phys. Rev. E* **63**, 015401 (2000).
- [147] T. R. Clark and H. M. Milchberg, *Phys. Rev. Lett.* **78**, 2373 (1997).
- [148] A. J. Gonsalves, T. P. Rowlands-Rees, B. H. P. Broks, J. J. A. M. van der Mullen, and S. M. Hooker, *Phys. Rev. Lett.* **98**, 025002 (2007).
- [149] H. M. Milchberg, K. Y. Kim, V. Kumarappan, B. D. Layer, and H. Sheng, *Philos. Trans. A. Math. Phys. Eng. Sci.* **364**, 647 (2006).
- [150] H. Sheng, K. Y. Kim, V. Kumarappan, B. D. Layer, and H. M. Milchberg, *Phys. Rev. E* **72**, 036411 (2005).
- [151] H. M. Milchberg, K. Y. Kim, V. Kumarappan, B. D. Layer, and H. Sheng, *Philos. Trans. A. Math. Phys. Eng. Sci.* **364**, 647 (2006).

- [152] S. J. Yoon, A. J. Goers, G. A. Hine, J. D. Magill, J. A. Elle, Y.-H. Chen, and H. M. Milchberg, *Opt. Express* **21**, 15878 (2013).
- [153] O. Hagen, *Surf. Sci.* **106**, 101 (1981).
- [154] H. Milchberg, S. McNaught, and E. Parra, *Phys. Rev. E* **64**, 056402 (2001).
- [155] B. D. Layer, A. G. York, S. Varma, Y.-H. Chen, and H. M. Milchberg, *Opt. Express* **17**, 4263 (2009).
- [156] T. Ditmire, T. Donnelly, A. Rubenchik, R. Falcone, and M. Perry, *Phys. Rev. A* **53**, 3379 (1996).
- [157] E. Parra, I. Alexeev, J. Fan, K. Kim, S. McNaught, and H. Milchberg, *Phys. Rev. E* **62**, R5931 (2000).
- [158] S. Shiraishi, C. Benedetti, A. J. Gonsalves, K. Nakamura, B. H. Shaw, T. Sokollik, J. van Tilborg, C. G. R. Geddes, C. B. Schroeder, C. Tóth, E. Esarey, and W. P. Leemans, *Phys. Plasmas* **20**, 063103 (2013).
- [159] M. Z. Mo, A. Ali, S. Fourmaux, P. Lassonde, J. C. Kieffer, and R. Fedosejevs, *Appl. Phys. Lett.* **100**, 074101 (2012).
- [160] M. Z. Mo, A. Ali, S. Fourmaux, P. Lassonde, J. C. Kieffer, and R. Fedosejevs, *Appl. Phys. Lett.* **102**, 134102 (2013).
- [161] Y. Glinec, J. Faure, A. Guemnie-Tafo, V. Malka, H. Monard, J. P. Larbre, V. De Waele, J. L. Marignier, and M. Mostafavi, *Rev. Sci. Instrum.* **77**, 103301 (2006).
- [162] A. Buck, K. Zeil, A. Popp, K. Schmid, A. Jochmann, S. D. Kraft, B. Hidding, T. Kudyakov, C. M. S. Sears, L. Veisz, S. Karsch, J. Pawelke, R. Sauerbrey, T. Cowan, F. Krausz, and U. Schramm, *Rev. Sci. Instrum.* **81**, 033301 (2010).
- [163] D. F. Gordon, *IEEE Trans. Plasma Sci.* **35**, 1486 (2007).

- [164] M. V. Ammosov, N. B. Delone, and V. P. Krainov, *Sov. Phys. JETP* **64**, 1191 (1986).
- [165] S. Payeur, S. Fourmaux, B. E. Schmidt, J. P. MacLean, C. Tchervenkov, F. Légaré, M. Piché, and J. C. Kieffer, *Appl. Phys. Lett.* **101**, 041105 (2012).
- [166] Y. I. Salamin, Z. Harman, and C. H. Keitel, *Phys. Rev. Lett.* **100**, 155004 (2008).
- [167] Y. Liu, D. Cline, and P. He, *Nucl. Instruments Methods Phys. Res. Sect. A Accel. Spectrometers, Detect. Assoc. Equip.* **424**, 296 (1999).
- [168] P.-L. Fortin, M. Piché, and C. Varin, *J. Phys. B At. Mol. Opt. Phys.* **43**, 025401 (2009).
- [169] L. J. Wong and F. X. Kärtner, *Opt. Express* **18**, 25035 (2010).
- [170] Sung Jun Yoon, *Quasi-Phasematched Acceleration of Electrons in a Density Modulated Plasma Waveguide*. PhD thesis, University of Maryland, College Park, 2014.
- [171] M. Yamada, N. Nada, M. Saitoh, and K. Watanabe, *Appl. Phys. Lett.* **62**, 435 (1993).
- [172] G. Khanarian, R. A. Norwood, D. Haas, B. Feuer, and D. Karim, *Appl. Phys. Lett.* **57**, 977 (1990).
- [173] B. Layer, A. York, T. Antonsen, S. Varma, Y.-H. Chen, Y. Leng, and H. Milchberg, *Phys. Rev. Lett.* **99**, 035001 (2007).
- [174] B. D. Layer, J. P. Palastro, A. G. York, T. M. Antonsen, and H. M. Milchberg, *New J. Phys.* **12**, 095011 (2010).
- [175] G. Hine, A. Goers, S. Yoon, J. Elle, and H. Milchberg, *CLEO 2014 JW2A.87* (2014).
- [176] P. Brijesh, C. Thaury, K. T. Phuoc, S. Corde, G. Lambert, V. Malka, S. P. D. Mangles, M. Bloom, and S. Kneip, *Phys. Plasmas* **19**, 063104 (2012).

- [177] M.-W. Lin, Y.-M. Chen, C.-H. Pai, C.-C. Kuo, K.-H. Lee, J. Wang, S.-Y. Chen, and J.-Y. Lin, *Phys. Plasmas* **13**, 110701 (2006).
- [178] T. Kuga, Y. Torii, N. Shiokawa, T. Hirano, Y. Shimizu, and H. Sasada, *Phys. Rev. Lett.* **78**, 4713 (1997).
- [179] S. Sato, Y. Harada, and Y. Waseda, *Opt. Lett.* **19**, 1807 (1994).
- [180] M. Meier, V. Romano, and T. Feurer, *Appl. Phys. A* **86**, 329 (2007).
- [181] A. V Nesterov and V. G. Niziev, *J. Phys. D. Appl. Phys.* **33**, 1817 (2000).
- [182] B. Hecht and L. Novotny, *Principles of Nano-Optics*, 2nd ed. (Cambridge University Press, 2012).
- [183] L. W. Davis and G. Patsakos, *Opt. Lett.* **6**, 22 (1981).
- [184] A. April, *Opt. Lett.* **33**, 1563 (2008).
- [185] Y. I. Salamin, *New J. Phys.* **8**, 133 (2006).
- [186] S. Quabis, R. Dorn, and G. Leuchs, *Appl. Phys. B Lasers Opt.* **81**, 597 (2005).
- [187] G. Machavariani, Y. Lumer, I. Moshe, A. Meir, and S. Jackel, *Opt. Lett.* **32**, 1468 (2007).
- [188] M. Stalder and M. Schadt, *Opt. Lett.* **21**, 1948 (1996).
- [189] S. C. Tidwell, D. H. Ford, and W. D. Kimura, *Appl. Opt.* **29**, 2234 (1990).
- [190] E. Zauderer, *J. Opt. Soc. Am. A* **3**, 465 (1986).
- [191] Y. Fukuda, A. Y. Faenov, M. Tampo, T. A. Pikuz, T. Nakamura, M. Kando, Y. Hayashi, A. Yogo, H. Sakaki, T. Kameshima, A. S. Pirozhkov, K. Ogura, M. Mori, T. Z. Esirkepov, J. Koga, A. S. Boldarev, V. A. Gasilov, A. I.

- Magunov, T. Yamauchi, R. Kodama, P. R. Bolton, Y. Kato, T. Tajima, H. Daido, and S. V. Bulanov, *Phys. Rev. Lett.* **103**, 165002 (2009).
- [192] A. Lifschitz, F. Sylla, S. Kahaly, A. Flacco, M. Veltcheva, G. Sanchez-Arriaga, E. Lefebvre, and V. Malka, *New J. Phys.* **16**, 033031 (2014).
- [193] A. Willner, F. Tavella, M. Yeung, T. Dzelzainis, C. Kamperidis, M. Bakarezos, D. Adams, M. Schulz, R. Riedel, M. Hoffmann, W. Hu, J. Rossbach, M. Drescher, N. Papadogiannis, M. Tatarakis, B. Dromey, and M. Zepf, *Phys. Rev. Lett.* **107**, 175002 (2011).
- [194] C. Altucci, C. Beneduce, R. Bruzzese, C. De Lisio, G. S. Sorrentino, T. Starczewski, and F. Vigilante, *J. Phys. D. Appl. Phys.* **29**, 68 (1999).
- [195] T. Ditmire, J. Zweiback, V. P. Yanovsky, T. E. Cowan, and G. Hays, *Nature* **398**, 489 (1999).
- [196] M. Krishnan, K. W. Elliott, C. G. R. Geddes, R. A. van Mourik, W. P. Leemans, H. Murphy, and M. Clover, *Phys. Rev. Spec. Top. - Accel. Beams* **14**, 033502 (2011).
- [197] F. Sylla, M. Veltcheva, S. Kahaly, A. Flacco, and V. Malka, *Rev. Sci. Instrum.* **83**, 033507 (2012).
- [198] E. Parra, S. J. McNaught, and H. M. Milchberg, *Rev. Sci. Instrum.* **73**, 468 (2002).
- [199] S. Semushin and V. Malka, *Rev. Sci. Instrum.* **72**, 2961 (2001).
- [200] R. Azambuja, M. Eloy, G. Figueira, and D. Neely, *J. Phys. D. Appl. Phys.* **32**, L35 (1999).
- [201] A. Murakami, J. Miyazawa, H. Tsuchiya, T. Murase, N. Ashikawa, T. Morisaki, R. Sakamoto, and H. Yamada, *J. Plasma Fusion Res.* **9**, 79 (2010).
- [202] J. Fan, T. R. Clark, and H. M. Milchberg, *Appl. Phys. Lett.* **73**, 3064 (1998).
- [203] D. Kaganovich, M. H. Helle, D. F. Gordon, and A. Ting, *Phys. Plasmas* **18**,



120701 (2011).

- [204] A. Buck, J. Wenz, J. Xu, K. Khrennikov, K. Schmid, M. Heigoldt, J. M. Mikhailova, M. Geissler, B. Shen, F. Krausz, S. Karsch, and L. Veisz, *Phys. Rev. Lett.* **110**, 185006 (2013).
  
- [205] K. Schmid and L. Veisz, *Rev. Sci. Instrum.* **83**, 053304 (2012).
  
- [206] P. M. Gerhart, R. J. Gross, and J. I. Hochstein, *Fundamentals of Fluid Mechanics* (Addison-Wesley, 1992).
  
- [207] Available online from U.S. Department of Energy Hydrogen Analysis Resource Center. [www.hydrogen.pnl.gov/hydrogen-data/](http://www.hydrogen.pnl.gov/hydrogen-data/)
  
- [208] B. R. Munson, D. F. Young, and T. H. Okiishi, *Fundamentals of Fluid Mechanics*, 2nd ed. (John Wiley & Sons, Inc., 1997).
  
- [209] Crane Company, *Flow of Fluids through Valves, Fittings, and Pipe*, (1988).
  
- [210] P. H. Oosthuizen and W. E. Carscallen, *Compressible Fluid Flow* (McGraw-Hill, 1997).
  
- [211] K. Y. Kim, V. Kumarappan, and H. M. Milchberg, *Appl. Phys. Lett.* **83**, 3210 (2003).
  
- [212] M. Takeda, H. Ina, and S. Kobayashi, *J. Opt. Soc. Am.* **72**, 156 (1982).
  
- [213] M. Kalal and K. A. Nugent, *Appl. Opt.* **27**, 1956 (1988).
  
- [214] T. Ditmire, T. Donnelly, R. Falcone, and M. Perry, *Phys. Rev. Lett.* **75**, 3122 (1995).
  
- [215] Y. Fukuda, H. Sakaki, M. Kanasaki, A. Yogo, S. Jinno, M. Tampo, A. Y. Faenov, T. A. Pikuz, Y. Hayashi, M. Kando, A. S. Pirozhkov, T. Shimomura, H. Kiriya, S. Kurashima, T. Kamiya, K. Oda, T. Yamauchi, K. Kondo, and S. V. Bulanov, *Radiat. Meas.* **50**, 92 (2013).

- [216] L. M. Chen, J. J. Park, K. H. Hong, J. L. Kim, J. Zhang, and C. H. Nam, *Phys. Rev. E - Stat. Nonlinear, Soft Matter Phys.* **66**, 17 (2002).
- [217] Y. Shao, T. Ditmire, J. Tisch, E. Springate, J. Marangos, and M. Hutchinson, *Phys. Rev. Lett.* **77**, 3343 (1996).
- [218] T. Caillaud, F. Blasco, F. Dorchies, Y. Glinec, C. Stenz, and J. Stevefelt, *Nucl. Instruments Methods Phys. Res. Sect. B Beam Interact. with Mater. Atoms* **205**, 329 (2003).
- [219] T. Ditmire, J. Zweiback, V. P. Yanovsky, T. E. Cowan, G. Hays, and K. B. Wharton, *Phys. Plasmas* **7**, 1993 (2000).
- [220] O. F. Hagen, *J. Chem. Phys.* **56**, 1793 (1972).
- [221] O. F. Hagen, *Rev. Sci. Instrum.* **63**, 2374 (1992).
- [222] H. Lu, G. Ni, R. Li, and Z. Xu, *J. Chem. Phys.* **132**, 124303 (2010).
- [223] O. G. Danylchenko, S. I. Kovalenko, and V. N. Samovarov, *Tech. Phys. Lett.* **34**, 1037 (2008).
- [224] K. Y. Kim, V. Kumarappan, and H. M. Milchberg, *Appl. Phys. Lett.* **83**, 3210 (2003).
- [225] S. Cipiccia, M. R. Islam, B. Ersfeld, R. P. Shanks, E. Brunetti, G. Vieux, X. Yang, R. C. Issac, S. M. Wiggins, G. H. Welsh, M.-P. Anania, D. Maneuski, R. Montgomery, G. Smith, M. Hoek, D. J. Hamilton, N. R. C. Lemos, D. Symes, P. P. Rajeev, V. O. Shea, J. M. Dias, and D. A. Jaroszynski, *Nat. Phys.* **7**, 867 (2011).
- [226] H. Schworer, B. Liesfeld, H.-P. Schlenvoigt, K.-U. Amthor, and R. Sauerbrey, *Phys. Rev. Lett.* **96**, 014802 (2006).
- [227] S. Chen, N. D. Powers, I. Ghebregziabher, C. M. Maharjan, C. Liu, G. Golovin, S. Banerjee, J. Zhang, N. Cunningham, A. Moorti, S. Clarke, S. Pozzi, and D. P. Umstadter, *Phys. Rev. Lett.* **110**, 155003 (2013).

- [228] A. Pukhov and J. Meyer-ter-Vehn, *Appl. Phys. B Lasers Opt.* **74**, 355 (2002).
- [229] E. W. Gaul, M. Martinez, J. Blakeney, A. Jochmann, M. Ringuette, D. Hammond, T. Borger, R. Escamilla, S. Douglas, W. Henderson, G. Dyer, A. Erlandson, R. Cross, J. Caird, C. Ebbers, and T. Ditmire, *Appl. Opt.* **49**, 1676 (2010).
- [230] Z. H. He, B. Hou, J. A. Nees, J. H. Easter, J. Faure, K. Krushelnick, and A. G. R. Thomas, *New J. Phys.* **15**, 053016 (2013).
- [231] D. G. Jang, Y. S. You, H. M. Milchberg, H. Suk, and K. Y. Kim, *Appl. Phys. Lett.* **105**, 021906 (2014).
- [232] F. Sylla, A. Flacco, S. Kahaly, M. Veltcheva, A. Lifschitz, G. Sanchez-Arriaga, E. Lefebvre, and V. Malka, *Phys. Rev. Lett.* **108**, 115003 (2012).
- [233] F. Sylla, A. Flacco, S. Kahaly, M. Veltcheva, A. Lifschitz, V. Malka, E. D’Humières, I. Andriyash, and V. Tikhonchuk, *Phys. Rev. Lett.* **110**, 085001 (2013).
- [234] G.-Z. Sun, E. Ott, Y. C. Lee, and P. Guzdar, *Phys. Fluids* **30**, 526 (1987).
- [235] G. Schmidt and W. Horton, *Phys. Fluids* **30**, 526 (1987).
- [236] D. Umstadter, S.-Y. Chen, A. Maksimchuk, G. Mourou, and R. Wagner, *Science* **273**, 472 (1996).
- [237] S. V. Bulanov, F. Pegoraro, and A. Pukhov, *Phys. Rev. Lett.* **74**, 710 (1995).
- [238] A. G. R. Thomas, S. P. D. Mangles, Z. Najmudin, M. C. Kaluza, C. D. Murphy, and K. Krushelnick, *Phys. Rev. Lett.* **98**, 054802 (2007).
- [239] S. V. Bulanov, T. Z. Esirkepov, M. Kando, J. K. Koga, A. S. Pirozhkov, T. Nakamura, S. S. Bulanov, C. B. Schroeder, E. Esarey, F. Califano, and F. Pegoraro, *Phys. Plasmas* **19**, 113102 (2012).
- [240] B. M. Penetrante and J. N. Bardsley, *Phys. Rev. A* **43**, 3100 (1991).

- [241] J. D. Jackson, *Classical Electrodynamics*, 3rd ed. (Wiley, New York, 2001).
- [242] F. Y. Li, Z. M. Sheng, M. Chen, L. L. Yu, J. Meyer-ter-Vehn, W. B. Mori, and J. Zhang, *Phys. Rev. E* **90**, 043104 (2014).
- [243] Y.-H. Chen, S. Varma, I. Alexeev, and H. Milchberg, *Opt. Express* **15**, 7458 (2007).
- [244] K. Y. Kim, I. Alexeev, and H. M. Milchberg, *Appl. Phys. Lett.* **81**, 4124 (2002).
- [245] N. Forget, V. Crozatier, and P. Tournois, *Appl. Phys. B Lasers Opt.* **109**, 121 (2012).
- [246] A. P. Kovács, K. Osvay, G. Kurdi, M. Görbe, J. Klebniczki, and Z. Bor, *Appl. Phys. B Lasers Opt.* **80**, 165 (2005).
- [247] C. Sainz, P. Jourdain, R. Escalona, and J. Calatroni, *Opt. Commun.* **111**, 632 (1994).
- [248] A. Pukhov, Z.-M. Sheng, and J. Meyer-ter-Vehn, *Phys. Plasmas* **6**, 2847 (1999).
- [249] J. L. Shaw, F. S. Tsung, N. Vafaei-Najafabadi, K. A. Marsh, N. Lemos, W. B. Mori, and C. Joshi, *Plasma Phys. Control. Fusion* **56**, 084006 (2014).
- [250] F. Albert, A. G. R. Thomas, S. P. D. Mangles, S. Banerjee, S. Corde, A. Flacco, M. Litos, D. Neely, J. Vieira, Z. Najmudin, R. Bingham, C. Joshi, and T. Katsouleas, *Plasma Phys. Control. Fusion* **56**, 084015 (2014).